WARWICK
THE UNIVERSITY OF WARWICK

A Thesis Submitted for the Degree of PhD at the University of Warwick

Permanent WRAP URL:
http://wrap.warwick.ac.uk/135406

Copyright and reuse:
This thesis is made available online and is protected by original copyright.
Please scroll down to view the document itself.
Please refer to the repository record for this item for information to help you to cite it.
Our policy information is available from the repository home page.

For more information, please contact the WRAP Team at: wrap@warwick.ac.uk

warwick.ac.uk/lib-publications

Electrons and Phonons in Low-Dimensional Semiconductor Structures

by

X Zianni

This thesis is presented to the University of Warwick
in partial fulfillment of the requirements for entry
to the degree of Doctor of Philosophy
Department of Physics

September 28, 1993

Contents

1 Introduction **1**

1.1 Interest in semiconductor heterostructures 1

1.2 Main features of low-dimensional structures 2

1.3 The confining potential and the formation of a Q2DEG 5

1.3.1 Si-MOSFET 5

1.3.2 GaAs/$Al_xGa_{1-x}As$ heterojunction 7

1.4 Electron confinement in inversion layers 8

1.5 Outline of the thesis. 10

2 Longitudinal optical phonons in a AlAs/GaAs/AlAs quantum well. **12**

2.1 Introduction. 12

2.2 Dispersionless Continuum Models. 14

2.3 The Modified Dielectric Continuum Model (MDCM) 18

2.4 Results and Discussion. 22

3 Electron transport: theoretical considerations **31**

3.1 The transport coefficients 31

3.2 Two-dimensional Boltzmann transport theory 32

3.3 Electron screening 35

3.4 Electron scattering by static defects. 41

3.4.1 Ionized impurity scattering. 41

3.4.2 Interface roughness scattering. 43

3.5 Thermopower 44

3.5.1 Diffusion thermopower 45
3.5.2 Phonon drag 46

4 Electron transport: calculations **51**
4.1 Introduction 51
4.2 Electron transport in a Si-MOSFET for $T < 2$ K. 52
4.2.1 Dominant scattering mechanisms. 53
4.2.2 More on electron scattering. 56
4.2.3 Calculated transport coefficients. 61
4.3 Electron transport in a Si-MOSFET for $T > 2$ K. 68
4.4 Electron mobility in a GaAs/AlGaAs heterojunction. 74
4.5 Thermopower in a GaAs/AlGaAs heterojunction 80

5 Semiclassical magnetothermopower of a two-dimensional electron gas **84**
5.1 Introduction 84
5.2 The Boltzmann equation. 85
5.3 Calculation of the thermopower and the Nernst-Ettinghausen coefficient. 86
5.3.1 Diffusion. 86
5.3.2 Phonon drag. 88
5.4 Discussion. 90

6 Conclusions and suggestions for further work **99**

Appendix A: Normalized phonon potential functions **105**

Appendix B: Solution of Boltzmann equation **107**

Appendix C: Derivation of transport coefficients for electron diffusion processes **110**

Bibliography **112**

List of Figures

1.1 Quasi-2D band structure and density of states 4
1.2 Cross section through a Si-MOSFET. 6
1.3 Band profile in a Si-MOSFET. 6
1.4 Band profile in the heterojunction. 7

2.1 Scalar potential as predicted by MDCM in the dispersionless limit 23
2.2 Dispesion curves for LO phonon modes. 25
2.3 Scalar potential for even modes. 26
2.4 Scalar potential for odd modes. 27

3.1 2D polarizability at finite T in Si and GaAs. 39

4.1 Measured mobilities and thermopowers in Si-MOSFETs 54
4.2 Scattering angle distribution for various processes 57
4.3 Wavevector and scattering angle distributions 58
4.4 The effect of image potential and temperature dependence of screening on electron relaxation times 59
4.5 Electron density variation of the relaxation times 62
4.6 Independently fitted electron mobilities 63
4.7 Calculated mobilities and values of p 66
4.8 Calculated and measured thermopowers 67
4.9 Simplified picture for electron-phonon interaction resonance . . . 70
4.10 Temperature dependence of phonon mean free paths 73
4.11 Effect of N_{free} in S_g calculations 75

4.12 Effect of temperature dependence of screening, of image potential and energy broadening of the relaxation time 76
4.13 Electron mobilities in GaAs/AlGaAs heterojunctions 79
4.14 Piezoelectric scattering and deformation potential in heterojunctions 81
4.15 Calculated and measured thermopowers for GaAs/AlGaAs heterojunctions 83

5.1 Thermopower tensor versus $\omega\tau_f$. 91
5.2 Magnetothermopower tensor in a Si-MOSFET at $T = 1.5$ K. . . . 92
5.3 Magnetothermopower tensor in a Si-MOSFET at $T = 7$ K. 93
5.4 Magnetothermopower tensor in a GaAs/AlGaAs heterojunction at $T = 7$ K. 95
5.5 Validity of approximations in magnetothermopower calculations. 98

List of Tables

4.1 Data for Si-MOSFET samples (after Oxley) 52

4.2 Mobilities for Fletcher's GaAs samples 78

4.3 Estimated phonon mean free path values 82

Acknowledgments

I would like to take this opportunity to thank some of the many people who helped me conclude my studies:

My parents and sisters for their love and encouragement

Professor P N Butcher for his excellent supervision

Professor G P Triberis for his support

Dr. M J Kearney for his help

Dimitris Charalambakis for his love and understanding

My good friends Kostas Simserides, Thanassis Yannacopoulos, Electra Petrakou, Giorgos Leftheriotis and Vasilis Karavolas for their friendship and my colleagues Hui Tang and Daping Chu for much fruitful discussion and their help.

SERC, GEC Hirst research centre and the University of Warwick for financial support.

Declaration

This thesis, unless where stated otherwise, contains an account of my own independent research work performed in the Department of Physics at the University of Warwick between October 1991 and September 1993 under the supervision of Professor P N Butcher.

Some of the work has been published previously:

'Macroscopic behaviour of longitudinal optical phonons in an AlAs/GaAs/AlAs quantum well'
X Zianni, P N Butcher and I Dharssi, J. Phys.: Condens. Matter 4 L77 (1992)

or is on the course of publication:

1. 'Semiclassical Magnetothermopower of a two-dimensional electron gas'
X Zianni, P N Butcher and M J Kearney (to appear in Phys. Rev. B)

2. 'The effect of interface roughness on the transport of a two-dimensional electron gas in a Si-MOSFET'
X Zianni and P N Butcher (to be submitted to J. Phys.: Condens. Matter)

The following papers have been presented as posters at conferences:

1. 'Macroscopic behaviour of longitudinal optical phonons in a AlAs/GaAs/AlAs quantum well'
CMMP 91, University of Birmingham (1991) and
Winter Schools on new Concepts in Semiconductor Nanostructures, Mauntendorf, Austria (1992).

2. 'Study of the thermopower of a 2DEG in a Si-MOSFET'

X Zianni, P N Butcher, J P Oxley and B L Gallagher

CMMP 92, University of Sheffield (1992).

Summary

Calculation of longitudinal optical (LO) mode potential functions and dispersion curves are made for a AlAs/GaAs/AlAs quantum well using a macroscopic model. The interface boundary conditions employed are continuity of potential and of the normal components of both electric flux density and relative ionic displacement. In the non-dispersive limit the model yields unique potential functions of two types: confined modes and interface modes. The confined mode potential functions are almost identical to those calculated for a microscopic model by Huang and Zhu. The interface modes are identical to those predicted by both the microscopic model and the dielectric continuum model. The introduction of bulk dispersion in GaAs produces modes which are hybrids of the confined and interface phonons.

The mobility and thermopower of a 2DEG are calculated in order to explain measurements on two Si-MOSFETs. In one of the samples at $T < 2$ K and electron densities $N_s > 10^{16} m^{-2}$, positive thermopowers have been measured. The change of sign in the thermopower is attributed to dominance of interface roughness scattering. Simultaneous consideration of the two transport properties results to discrepancies between theory and experiment, that indicate the inadequacy of an isotropic statistical theory for interface roughness to explaine electron scattering by interface irregularities in one of the samples. This idea is also supported by calculations in GaAs/AlGaAs heterojunctions where very good agreement has been found with experiments of Fletcher.

Experimental data of thermopower at temperatures $T > 2$ K are explained by phonon drag and good agreement between theory and experiment is obtained in both Si-MOSFETs and GaAs/AlGaAs heterojunctions. The calculations are based on the theory formulated by Cantrell and Butcher and are extended to account for the temperature dependence of screening, the temperature dependence of phonon mean free path and the thermal broadening of the Fermi distribution.

Recent studies of the magnetothermopower of a two-dimensional electron gas have concentrated on measurements in either the low-field weak localization regime or the high-field Landau quantization regime. In this thesis we emphasize that for magnetic fields between these two limits there is an interesting intermediate regime in which the total thermopower is dominated by semiclassical effects. Detailed expressions are derived for both the diffusion and phonon-drag contributions to the thermopower and a number of important observations are made that should be directly amenable to experimental verification.

To my parents

Dimitrios and Ageliki

and to my sisters

Georgia and Stavroula

Chapter 1

Introduction

1.1 Interest in semiconductor heterostructures

In recent years semiconductor heterostructures have become model systems for the investigation of electronic conduction on mesoscopic scales. Technological advances such as molecular beam epitaxy (MBE) and metal-organic chemical vapor deposition (MOCVD) have made possible the realization of semiconductor structures whose properties differ from the bulk semiconductors. Structures can be constructed that contain a thin layer of highly mobile electrons. The electrons are confined in the direction perpendicular to the layer and are constrained to move within it. These systems are characterized by low electron densities that can be varied by an applied electric field. The Fermi wavelength is therefore very large (typically 40 nm) and comparable to the dimensions of structures which can be defined lithographically.

Low-dimensional semiconductor heterostructures first attracted interest in the seventies due to the pioneering work of Esaki and Tsu on transport properties and of Dingle on optical properties. The improved growth techniques, the novel physics thereby introduced (for instance, the quantum Hall effect) and the applications (e.g modulation doped FETs, quantum well lasers) resulted in rapid progress. In the mid-eighties, electron mobilities up to $2\times 10^6 cm^2/Vs$, the integer and fractional quantum Hall effect, low-threshold quantum lasers, ultra-high speed microwave and digital integrated circuits, the realization of electro-

optical and nonlinear materials were characteristic achievements [1]. This remarkable progress has continued and now electron mobilities have reached $12 \times 10^6 cm^2/Vs$, where numerous new effects are exhibited by lower dimensionality systems, such as quantized point contact resistance, electron focusing, ballistic motion up to 100 μm etc. An abundance of applications such as the improved performance of the quantum well laser, vertical emitting lasers, etc. have been achieved. Devices based on both horizontal and vertical transport are still progressing in speed and integration level. Quantized semiconductor structures are already an industrial reality as low noise transistors and quantum well lasers [1].

The interest in low-dimensional structures is well justified by both pure scientific interest and technological applications. In this thesis, the discussion is concentrated on the effect of the reduced dimensionality of the system on phonon modes and electron transport properties.

1.2 Main features of low-dimensional structures

The reduced dimensionality character of the electrons can be seen as a gradual transition from the bulk. Let us imagine an electron being in a 3D box. If the box sides are considerably longer than the electron wavelength, they do not influence its motion. If one of the boundary lengths decreases enough to become comparable to the electron wavelength, the electron feels the boundary and its properties are thereby modified. It is no longer free to move in this direction and the corresponding wave vector component is not a good quantum number. Since it is still free to move in two directions, the electron is said to be two-dimensional. A second boundary can be reduced to produce confinement in an additional direction and then the electron motion becomes one-dimensional with the conduction being along a wire. The confinement can be extended to all the three dimensions, leading to quantum dots. In every case the spatial extent of the electron wavefunction is non-zero in the confinement direction and the confinement may be said to be quasi-2D, quasi-1D or quasi-0D.

In what follows, we are going to concentrate on the quasi-2D electron gas

(from now on referred to as the Q2DEG). The essential feature of the Q2DEG is the creation of a narrow potential well in the conduction band for motion in one direction. This can be formed by an applied electric field or by the band gap discontinuity between the materials across a heterointerface. Its shape can be complicated and an exact treatment would provide us with an equally complicated theory, not easily applicable to study the electron gas properties. Fortunately, simplifications can be made which allow progress. The carriers are treated within the effective mass approximation [2]. In the conducting plane the wave functions are 2D plane waves ($e^{i\mathbf{k}\cdot\mathbf{r}}$), with $\mathbf{k}$ and $\mathbf{r}$ being the 2D wave vector and position vector respectively. It is assumed that the spatial variation of the average electrostatic potential is slow and smooth, so that the electronic structure and the key bulk physical parameters such as the band gaps, band widths, effective masses etc. remain unchanged. In short, we set up the theory on the assumption that the electrostatic potential representing the band bending can be superimposed upon the bulk crystal potential. As an electron approaches the interface region, it will experience a potential which is the consequence of the crystal potential and the electron distribution, given by solving the Poisson and Schrödinger equations self-consistently. For a finite well, discrete energy levels ε_a are expected. We consider cases in which these subbands occur in the conduction band and use the index a as the subband index.

If the conduction plane (xy plane) area is A, the single particle electron eigenfunction in the independent electron picture is:

$$\psi_{a,\mathbf{k}}(\mathbf{r},z) = A^{-1/2}e^{i\mathbf{k}\cdot\mathbf{r}}\phi_a(z). \tag{1.1}$$

Each state is labelled by the subband index and 2D wave vector (a,$\mathbf{k}$). The envelope function for the z direction $\phi_a(z)$ satisfies:

$$-\frac{\hbar^2}{2m}\frac{d^2}{dz^2}\phi_a(z) + V(z)\phi_a(z) = \varepsilon_a\phi_a(z) \tag{1.2}$$

where $V(z)$ is the confining potential. The corresponding band structure is illustrated in figure 1.1a, where all states are filled up to the Fermi level ε_f at $T = 0$ K. The density of states k for each subband is constant and equal to

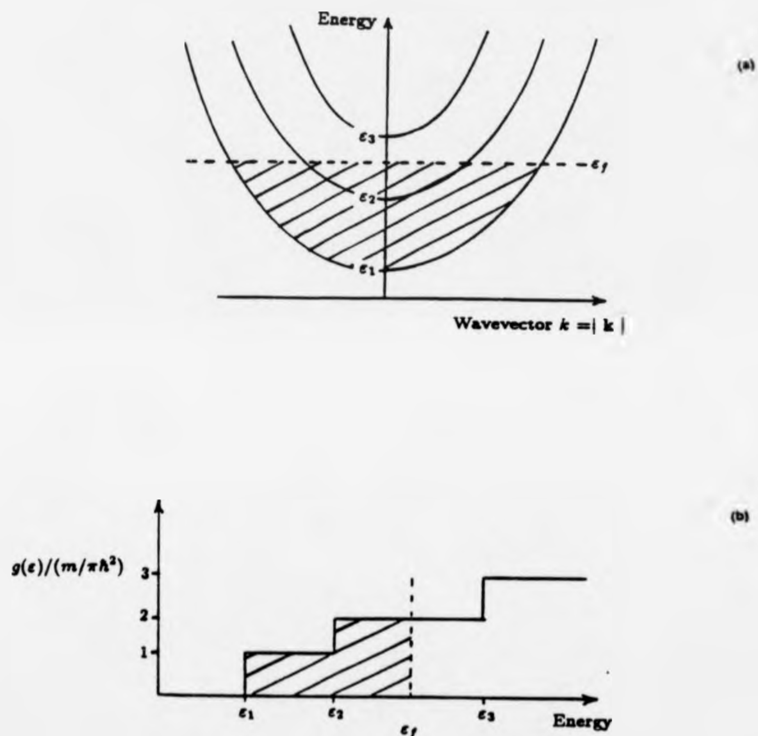

Figure 1.1: Quasi-2D band structure and density of states

(a) Quasi-2D band structure and filling of states $(\alpha, \mathbf{k})$ up to the Fermi level ε_f at $T = 0$ K.

(b) Quasi-2D density of states corresponding to (a).

$m/\pi\hbar^2$ per unit area (see figure 1.1b). The total density of states is:

$$g(\varepsilon) = \sum_{\alpha} \frac{Am}{\pi\hbar^2}\Theta(\varepsilon - \varepsilon_\alpha) \quad (1.3)$$

where $\Theta(\varepsilon)$ is the unit step function. When the electron density is low enough so that the Fermi level lies below the second subband edge, only the ground subband is occupied and higher subbands can be neglected in the calculations. This limit is called 'quantum limit' (QL) and will be assumed throughout this thesis.

1.3 The confining potential and the formation of a Q2DEG

Two common structures are discussed, the Si-MOSFET and the GaAs/AlGaAs heterojunction. The shape of the confining potential in these two structures is the basis of the calculations presented in the following chapters. We confine our discussion to the low temperature regime in which the electrons are degenerate.

1.3.1 Si-MOSFET

The silicon metal-oxide-semiconductor (MOS) field effect transistor has been one of the major components of memory and logic circuits. A cross-section of a Si-MOSFET is shown in figure 1.2. Figure 1.3a shows the electronic structure before charge equilibrium is established. Here the Fermi energies of the metal and p-Si are separated by the potential energy step $e\Phi$. When the two Fermi energies come into equilibrium, a space charge region is established in the semiconductor and there is a gradient of the potential across the oxide, indicated schematically in the equilibrium band diagram shown in figure 1.3b. This gradient represents the built-in electric field due to the difference in the work function of the metal and semiconductor illustrated in figure 1.3a. A positive voltage applied to the metal relative to the semiconductor attracts electrons into the Si side of the SiO_2-Si interface and repeals holes from the interface. This means that the band bending is increased (figure 1.3c). When the con-

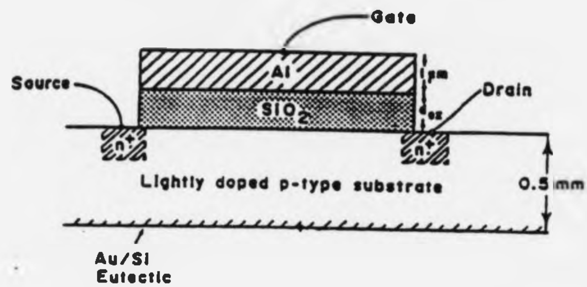

Figure 1.2: Cross section through a Si-MOSFET.

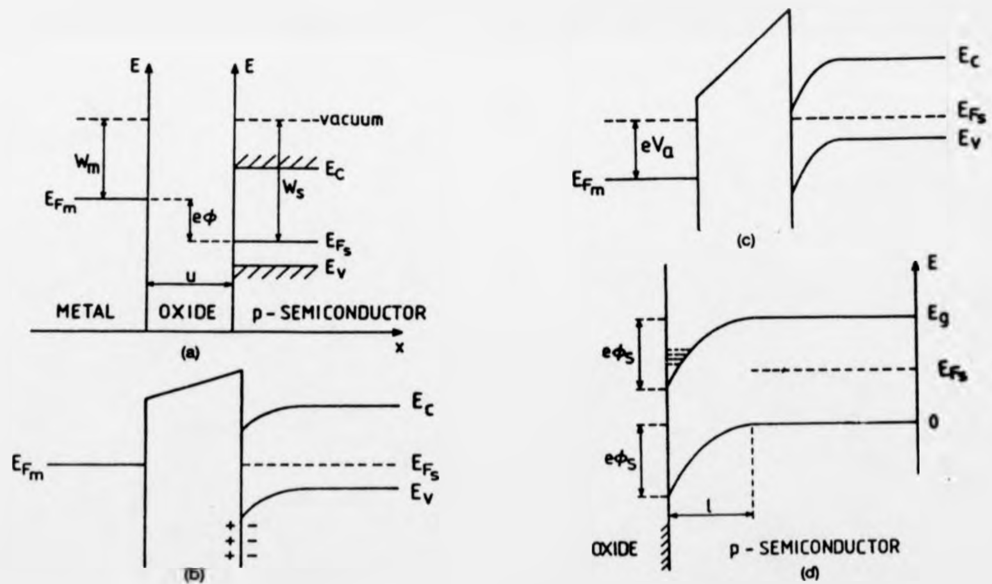

Figure 1.3: Band profile in Si-MOSFET.

duction band edge drops below the Fermi level in the Si, an n-type inversion layer is formed near the interface as shown in figure 1.3d. More electrons can be dragged into the inversion layer by increasing the applied gate voltage.

1.3.2 GaAs/$Al_xGa_{1-x}As$ heterojunction

A confining potential similar to the Si-MOSFET is created at the GaAs/ $Al_xGa_{1-x}As$ heterojunction, when the wide gap material ($Al_xGa_{1-x}As$) is n-doped, while the narrow gap material (GaAs) is p-doped or is essentially undoped. The two materials have different band gaps E_g (1.52 eV at 4 K in GaAs and about 2 eV in the alloy for $x = 0.3$) which gives rise to a discontinuity ΔE_g shared unequally by the conduction band edge (ΔE_c) and valence band edge (ΔE_v). The band profile is shown in figure 1.4a. Under equilibrium conditions,

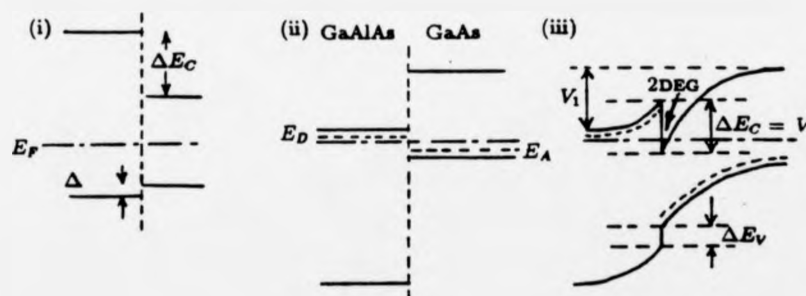

Figure 1.4: Band profile in the heterojunction.

(i) Before doping (including discontinuities), (ii) after doping, by matching ε_f and (iii) the observed profile (including discontinuities).

electrons in donor levels of the $Al_xGa_{1-x}As$ are transferred to the GaAs layer, leading to considerable band bending and forming a two-dimensional electron gas in the GaAs. When the two-dimensional system is in equilibrium with the donor levels in the alloy layer, the following condition is satisfied (in MKS units) [3]:

$$\varepsilon_o + \varepsilon_f = V_o - E_B - \frac{e^2}{2\epsilon_o \kappa}\frac{(N_s + N_{depl})^2}{N_D} - \frac{e^2}{\epsilon_o \kappa}(N_s + N_{depl})d \qquad (1.4)$$

where ϵ_o is the permittivity of free space, κ is the static dielectric constant (assumed to be the same for both GaAs and $Al_xGa_{1-x}As$), d is the thickness of the undoped $Al_xGa_{1-x}As$ layer (spacer layer), N_D is the ionized donor concentration, N_s is the surface density of electrons and N_{depl} is the the surface density of ionized acceptors in the GaAs. Finally, $-E_B$ is the energy of a donor measured from the bottom of the $Al_xGa_{1-x}As$ conduction band and ε_o is the ground subband energy measured from the bottom of the conduction band of GaAs at the interface. The electron density in this system can be changed by illumination. As far as the subband structure is concerned, the heterojunction is almost equivalent to the usual inversion layer in a Si-MOSFET. The only difference is that the wave function has a non-vanishing amplitude in the $Al_xGa_{1-x}As$ layer because the barrier height V_o is typically not particularly large (~ 300 meV).

The main advantages of the MOSFET in low-dimensional structure experiments are the oxide stability, the low interface states density and the high breakdown field ($10^9 Vm^{-1}$) which allows a variation of the surface electron density over the range $10^{15} - 10^{17} m^{-2}$ [2]. The lower limit is determined by the influence of disorder. The advantage of the heterojunction is the high mobility resulting by the interface quality and modulation doping (i.e. the separation between the electrons and the charged centers by an undoped spacer layer).

1.4 Electron confinement in inversion layers

The electron envelope function in the confinement direction can be accurately calculated self-consistently [2]. It is also satisfactorily described by an appropriate variational wavefunction which has the advantage of having an analytical form. In the independent particle effective-mass approximation, the envelope function should describe the electron confinement and reflect the structure properties such as effective mass, doping level etc. in a reliable way. It is commonly characterized by a single parameter which is determined by the standard vari-

ational procedure.

The simplest variational wave function is the one first proposed by Fang and Howard [4]:

$$\zeta(z) = (\frac{b^3}{2})^{1/2} z e^{-bz/2} \tag{1.5}$$

for which the average penetration of the charge into the semiconductor is:

$$z_o = \frac{3}{b}. \tag{1.6}$$

The simplicity of this wave function enables the evaluation of the expectation values of all the terms in the Hamiltonian. It is found that [2]:

$$< T >= \frac{\hbar^2 b^2}{8m_z}, \tag{1.7}$$

$$< V_d >= \frac{3e^2 N_{depl}}{\epsilon_o \kappa_{sc} b} - \frac{6e^2 N_A}{\epsilon_o \kappa_{sc} b^2}, \tag{1.8}$$

$$< V_s >= \frac{33e^2 N_s}{16\epsilon_o \kappa_{sc} b}, \tag{1.9}$$

and

$$< V_I >= \frac{\kappa_{sc} - \kappa_{ins}}{\kappa_{sc} + k_{ins}} \frac{e^2 b}{32\pi\epsilon_o \kappa_{sc}}. \tag{1.10}$$

In these equations T, V_d, V_s and V_I respectively denote the kinetic energy, the potential energy of an electron interacting with the depletion charges, the potential energy of an electron interacting with the other electrons in the inversion layer and the image potential. The total energy per electron is the quantity to be minimized and it is:

$$\frac{E}{N} =< T > + < V_d > + \frac{1}{2} < V_s > + < V_I > . \tag{1.11}$$

The factor 1/2 in the above equation prevents double counting of electron-electron interactions. Neglecting exchange, correlation and quadratic terms in the depletion energy, the standard variational procedure gives for b [5]:

$$b = \frac{b_{SH}}{\beta} \tag{1.12}$$

where

$$b_{SH}^3 = \frac{12e^2 m_z^*}{\epsilon_o \kappa_{sc} \hbar^2}(N_{depl} + \frac{11}{32}N_s), \tag{1.13}$$

$$\beta = \delta^{1/2} cosh(\frac{1}{3} cosh^{-1}(4\delta^{-3/2})), \tag{1.14}$$

and

$$\delta = \frac{3}{8}\frac{m_z^*(\kappa_{sc} - \kappa_{ins})e^2}{4\pi\epsilon_o \hbar^2 b_{SH}(\kappa_{sc} + \kappa_{ins})\kappa_{sc}}. \tag{1.15}$$

Neglecting the image term, b becomes equal to b_{SH}.

1.5 Outline of the thesis.

In this chapter an introduction to the physics and the applications of two-dimensional semiconductor structures has been given and the systems to be investigated in this thesis have been described. The two-dimensional character of the carriers is expected to modify electron transport and to generate novel phenomena. For instance, the presence of heterointerfaces not only affects the electron scattering but also introduces additional optical phonon modes and therefore changes the electron-phonon interaction at high temperatures. Longitudinal optical phonons in AlAs/GaAs/AlAs quantum wells are examined in chapter 2, where a simple continuum model is proposed. The remaining chapters concentrate on electron transport at low temperatures, where the optical phonon contribution can be safely neglected. In chapter 3, the theoretical background of this study is briefly presented. Zero-magnetic field electron transport is extensively discussed in chapter 4. Simultaneous consideration of two transport properties, the mobility and the thermopower of Q2DEGs in Si-MOSFETs

and GaAs/AlGaAs heterojunctions, leads to improved understanding of the details of electron transport in these systems. In chapter 5, the existing semi-classical formalism is extended to accommodate the effect of a non-quantizing magnetic field applied perpendicular to the Q2DEG on the mobility and the thermopower. In chapter 6, the main conclusions are summarized and the possibilities for further investigation, as indicated by this study, are discussed.

Chapter 2

Longitudinal optical phonons in a AlAs/GaAs/AlAs quantum well.

2.1 Introduction.

Raman scattering experiments [6]-[9] and measurements on physical quantities such as transport coefficients that depend upon electron-phonon scattering, have stimulated a lot of interest in the properties of optical phonon modes of semiconductor heterostructures. In the case of polar semiconductor layers, the dispersion relation of optical phonons and their effective interaction with two-dimensionally confined electrons can be strongly modified compared to the three-dimensional case. The understanding of optical phonons in such situations has considerably improved in the last few years [10]-[14]. The physical problems that involve electron-phonon interaction require a reliable description of optical phonons. Lattice dynamic calculations based on reliable microscopic models [15]-[18] have been reported. Macroscopic models have also been proposed, but these often present different and sometimes controversial points of view and only

partially interpret the experiments. Raman experiments show the existence of different types of modes. Additionally to the bulklike modes there appears to be a series of interface phonon modes [6].

The straightforward approach to the problem is the microscopic one, which necessarily involves extensive numerical calculations. There are two main difficulties with this. Firstly, because the results are almost exclusively numerical, and their physical interpretation is not easily identified. Secondly, the electron-phonon interaction also has to be treated numerically. A simple macroscopic theory giving analytical results close to those of microscopic models would therefore be useful in studies of the interaction of phonons with electrons and light. Additionally, the Frölich interaction and electron-phonon scattering are dominated by long wavelength phonons and a continuum description would be well justified. On this basis an abundance of macroscopic models have been proposed, in which, after the differential equations in each layer are defined, connection rules are identified in order to match the solutions at the interfaces.

In the case of acoustic phonons in the long wavelength limit, macroscopic theories deal with the displacement of the ions which has to be continuous at the interfaces. In the case of optical phonons, the theory deals with relative displacements between the ions and the boundary conditions at the interfaces are now not at all obvious. Moreover, it has been argued that the differential equations do not hold at the interfaces and therefore cannot be used to derive the boundary conditions [19]. Indeed, one must accept that a continuum model of the matching problem is necessarily an approximation and cannot be rigorously justified. By recalling the motivation that lead to the continuum theory, one can convince hiself that the aim should not be to obtain results in perfect quantitative agreement with microscopic models, but rather solutions that have the general properties of the microscopic results and that are in good agreement with the experiments. After considerable debate on the points of controversy, it is now a general belief that macroscopic models can be formulated along these lines and that they work very well.

The work presented in this chapter was one of the first dispersive macro-

scopic models that, although not very rigorously formulated, provided a description of the longitudinal modes that was consistent with microscopic calculations. The proposed phonon modes are described by fields more complex than simple sinusoidal functions, and allow both electromagnetic and mechanical type boundary conditions to be satisfied [13]. In the following section, macroscopic models that neglect bulk dispersion, and thereby raise points of controversy, are discussed. The Modified Dielectric Continuum Model is formulated in section 2.3, and the results are extensively discussed in section 2.4.

2.2 Dispersionless Continuum Models.

The problem of the correct choice of the connection rules for the optical phonons at the interfaces has raised much controversy. Three different analytical expressions for optical phonon modes in GaAs/AlAs heterostructures have been proposed. In the continuum theory of the optical modes the dynamical fields are the electric field $\mathbf{E}$, and $\mathbf{w}(\mathbf{r}) = \rho^{1/2}\mathbf{u}(\mathbf{r})$, where $\mathbf{u}(\mathbf{r})$ is the relative displacement from equilibrium of the positive ions from the negative ions, $\mathbf{r}$ is the position vector and ρ is the reduced mass per unit volume of the lattice [20]. The interfaces of an AlAs/GaAs/AlAs quantum well, of width $L = 2d$, are taken parallel to the xy plane at $z = \pm d$ and translational invariance is assumed in this plane. For the longitudinal optical vibrations, $\mathbf{w}$ and $\mathbf{E}$ can be written inside the well as the gradient of a mechanical and electrostatic scalar potential:

$$\mathbf{w}(\mathbf{r}) = -\nabla(f(z)e^{i\mathbf{k}_{\parallel}\mathbf{x}_{\parallel}}) \tag{2.1}$$

$$\mathbf{E}(\mathbf{r}) = -\nabla(\Phi(z)e^{i\mathbf{k}_{\parallel}\mathbf{x}_{\parallel}}) \tag{2.2}$$

where $\mathbf{x}_{||} = (x, y)$ lies in the xy plane, $\mathbf{k}_{||}$ is a wave vector in that plane and $\mathbf{r} = (\mathbf{x}_{||}, z)$. When the bulk dispersion due to long-range forces between the ions is ignored, it can be proved (see equation (2.15)) that Φ is proportional to f.

The first model was based on the dispersionless dielectric continuum theory. The significant parameters in the theory are the bulk LO and TO mode frequencies in the GaAs layer at $k_{\|} = 0$, which we denote by ω_L and ω_T respectively. The model predicts two distinct types of optical phonon modes: interface modes and bulklike modes [21, 22, 23]. The bulklike optical phonon modes derived in the Dielectric Continuum Model (DCM) are usually called slab modes. They were first derived by Fuchs and Kliewer [21] and have electrostatic potential nodes and optical displacement antinodes at the interfaces. They are described by:

$$\Phi_{nk_{\|}} = \begin{cases} cos[(n+1)\pi z/L] & n\ even \\ sin[(n+1)\pi z/L] & n\ odd \end{cases} \tag{2.3}$$

Here, the symmetric (antisymmetric) vibrations correspond to even (odd) n.

The interface modes are orthogonal to the bulklike modes and their electrostatic potential is non-zero at the interfaces. They are waves having maximum amplitude at the interfaces and decaying away from it:

$$\Phi_{nk_{\|}} \sim \begin{cases} e^{k_{\|}z} & z < -d \\ e^{k_{\|}z} \pm e^{-k_{\|}z} & -d < z < d \\ \pm e^{-k_{\|}z} & z > d \end{cases} \tag{2.4}$$

where $\pm$ correspond to the symmetric and antisymmetric interface vibration respectively. Unlike the bulklike modes which are degenerate at ω_L, the frequencies of the interface modes depend on $k_{\|}$ and lie between ω_L and ω_T. The dispersion of the interface modes is an effect of the inhomogeneity of the structure. The difficulty with the DCM is connected with the boundary conditions, since the predicted modes have antinodes in the normal component of the GaAs relative displacement at the interfaces in a AlAs/GaAs/AlAs quantum well, which is contrary to the results of the microscopic calculations [16].

The second model, proposed by Huang and Zhu (HZ), is based on results calculated with a simple microscopic model [15]. The proposed expressions for the scalar potential are:

$$\Phi_{nk_{\|}}(z) = \begin{cases} cos[n\pi z/L] - (-1)^{n/2} & n = 2,4,... \\ sin(\mu_n \pi z/L) + c_n z/L & n = 3,5,... \end{cases} \tag{2.5}$$

with n even and odd for the symmetric and antisymmetric vibrations respectively and μ_n and c_n are constants to be determined by the boundary conditions. By critical comparison of microscopic results with the slab modes, HZ have shown that both the scalar potentials and optical displacement of the bulklike modes in GaAs/AlAs heterostructures have nodes at the interfaces, i.e. these vibrations are chosen so that $\Phi_{nk_{\|}}$ and $\Phi'_{nk_{\|}}$ vanish at the interfaces. Thus, they represent pure bulklike vibrations. However, these vibrations deviate from orthogonality and completeness as $k_{\|}$ is increased from zero. A refinement of the vibrations of equation (2.5) are the reformulated slab vibrations which obey the same boundary conditions [24, 25]. They have the form

$$\Phi_{nk_{\|}}(z) = \begin{cases} cos(k_n z) + D_{nk_{\|}} cosh(k_{\|} z) & even \\ sin(k_n z) + D_{nk_{\|}} sinh(k_{\|} z) & odd \end{cases} \tag{2.6}$$

where k_n is an eigenvalue of the component of the wavevector in the GaAs layer in the confinement direction. These formulae are preferable to those of HZ, because they represent distortions which are orthogonal, and which remain solutions of the continuum problem when isotropic dispersion is introduced. These modes can be called bulklike waves in the sense that the scalar potential has nodes at the interfaces.

The third model [6, 9] suggests that, the modes with zero $k_{\|}$ have optical displacements with nodes and electrostatic potentials with antinodes at the interfaces; they are usually denoted as guided modes and their scalar potential can be expressed as:

$$\Phi_{nk_{\|}} = \begin{cases} cos[n\pi z/L] & n\ even \\ sin[n\pi z/L] & n\ odd \end{cases} \tag{2.7}$$

where n is even (odd) for the symmetric (antisymmetric) vibrations. The optical

displacements predicted by this model agree with the results of a realistic linear chain model restricted to zero $k_{||}$, so that no interface modes are allowed [26, 27]. As an extension of this model to the case of finite $k_{||}$, Ridley and Babiker (RB) proposed the so-called hydrodynamic model (HD) [28, 29, 30], in which, besides the guided modes, HD-type interface modes are also allowed. It is well known that the number of modes is determined solely by the number of degrees of vibrational freedom. For a fixed phonon wave vector, there are altogether 3(M+N) optical phonon modes for $(GaAs)_M(AlAs)_N$ superlattices. For zero $k_{||}$, the linear chain calculation has clearly shown that there are M(N) LO modes and 2M(2N) TO modes confined respectively in GaAs(AlAs), which exhausts all the optical vibration degrees of freedom. Thus, with a finite $k_{||}$, it is impossible to retain all the guided modes found in the zero $k_{||}$ case and add some extra interface modes. Zhu showed [10] that the 'even solution' of the HD-type interface mode suggested by Ridley strongly overlaps with the $n = 1$ TO mode and the odd solution overlaps with the $n = 1$ LO mode. Unlike the slab and the reformulated slab modes, the guided vibrations are not bulklike vibrations since they are defined to obey $\Phi'_{nk_{||}} = 0$ at the interfaces in order to agree with the $k_{||} = 0$ modes observed in Raman backscattering [6]. They are actually linear combinations of the bulklike and interface vibrations.

Models which ignore bulk dispersion are inherently forced to predict vibrational modes ambiguously. These modes cannot be directly compared to experiments because they are infinitely degenerate at the bulk frequency ω_L and their potential patterns are therefore not uniquely defined. This problem indicates that the identification of the appropriate continuum model for optical phonons in heterostructures is only possible in a different framework, that of dispersive models. However, the inclusion of bulk dispersion does not trivially lead to a correct treatment of the problem. Some models followed the bulk situation very closely and they resulted in misleading solutions that did not represent the novel features of the heterostructures, such as the hybrid character of the modes predicted by microscopic calculations [19, 28]. A differential equation suitable for the present problem is considered in the next section. Its

solutions coincide with the reformulated slab vibrations of equation (2.6) and its eigenvalues are found by applying appropriate boundary conditions. Both the dispersive and non-dispersive cases are examined, with the latter treated as a limit of the former.

2.3 The Modified Dielectric Continuum Model (MDCM)

We use the phenomenological equations of Born and Huang [20] modified to include parabolic bulk dispersion [28]. Symmetry considerations [19] imply that the mechanical long range forces that are responsible for bulk dispersion are expressed by second order derivative terms. In esu the equations for LO phonons are:

$$\ddot{\mathbf{w}} = -\omega_T^2\mathbf{w} + (\frac{\varepsilon_o - \varepsilon_\infty}{4\pi})^{\frac{1}{2}}\omega_T\mathbf{E} - b_L^2\nabla^2\mathbf{w} \tag{2.8}$$

$$\mathbf{P} = (\frac{\varepsilon_o - \varepsilon_\infty}{4\pi})^{\frac{1}{2}}\omega_T\mathbf{w} + \frac{(\varepsilon_\infty - 1)}{4\pi}\mathbf{E} \tag{2.9}$$

where $\mathbf{w}$ is the displacement of the positive ions relative to the negative ions multiplied by the square root of the reduced mass per unit volume, $\mathbf{P}$ is the dielectric polarization, $\mathbf{E}$ is the electric field, ε_o and ε_∞ are the static and the high frequency dielectric constants respectively and ω_T is the transverse optical resonant frequency. The parameter b_L introduces parabolic dispersion. We ignore retardation so that:

$$\nabla \times \mathbf{E} = 0 \tag{2.10}$$

For LO modes in the quantum well structure a scalar electrostatic potential and a scalar mechanical potential can be defined as in equations (2.1, 2.2). The definition of the dielectric displacement $\mathbf{D}$ and equations (2.1), (2.2), and (2.9) give:

$$\nabla \cdot \mathbf{D} = \nabla \cdot [\varepsilon_\infty \mathbf{E} + 4\pi\gamma\mathbf{w}] = 0 \quad (2.11)$$

with $\gamma = \omega_T[(\varepsilon_o - \varepsilon_\infty)/4\pi]^{1/2}$.

We find from (2.8), (2.9) and (2.10) that Maxwell's equation (2.11) leads in each material to a fourth order differential equation for the z dependence of the mechanical scalar potential f:

$$b_L^2(f^{(4)} - k_\parallel^2 f'') + (\omega_L^2 - \omega^2 - b_L^2 k_\parallel^2)(f'' - k_\parallel^2 f) = 0 \quad (2.12)$$

in which $\omega_L = (\varepsilon_o/\varepsilon_\infty)^{1/2}\omega_T$. It follows that

$$f = \alpha e^{ik_n z} + be^{-ik_n z} + ce^{k_\parallel z} + de^{-k_\parallel z} \quad (2.13)$$

where

$$k_n^2 \equiv \frac{\omega_L^2 - \omega^2 - b_L^2 k_\parallel^2}{b_L^2} \quad (2.14)$$

Equation (2.14) is equivalent to the bulk dispersion relation for LO phonons: $\omega^2 = \omega_L^2 - b_L^2(k_\parallel^2 + k_n^2)$. The relation between the electrostatic scalar potential and the mechanical scalar potential is:

$$\Phi = \frac{(\omega^2 - \omega_T^2 + b_L^2 k_\parallel^2)f - b_L^2 f''}{\gamma} \quad (2.15)$$

and therefore, with the help of (2.13), we obtain:

$$\Phi = Ae^{ik_n z} + Be^{-ik_n z} + Ce^{k_\parallel z} + De^{-k_\parallel z} \quad (2.16)$$

The coefficients A,B,C,D and k_n in (2.16) remain to be determined by the interface boundary conditions.

We confine our attention to modes with frequencies close to ω_L for GaAs. Then, the effect of dispersion in the AlAs is unimportant and we set $b_L = 0$ there. This approximation is valid, since the amount of dispersion, i.e. the

bandwidth of bulk phonons, is smaller than the energy separation between the optical phonons in bulk GaAs and AlAs. We also set $A = B = 0$ there, because propagating modes are not possible without dispersion. Finally, we keep Φ finite as $z \rightarrow \pm\infty$ by putting $C = 0$ in the righthand AlAs region (in which $z \rightarrow +\infty$) and $D = 0$ in the lefthand AlAs region. Six coefficients remain to be determined by applying the appropriate boundary conditions.

Several authors have derived the connection rules on the interfaces by comparison of microscopic and continuum theories. Huang and Zhu [15] found that the solutions of a microscopic model of the lattice mechanics in the zero-dispersion limit with small $k_{||}$, can be approximated by the interface modes and the vibrations described by equations (2.5). A similar approach was adopted by Gerecke and Bechstedt [17] whose macroscopic model is the limit of a microscopic model in which the lattice constant tends to zero. Ando et al [16] use a dynamical equation equivalent to (2.8), but include anisotropy and impose either the boundary condition $\mathbf{w} = 0$ at the faces of the slab or connection rules from microscopic theory. In the first case the results were compared with those of microscopic calculations with good agreement.

The connection rules that relate the fields on either side of an interface can also be derived from a continuum theory [14], if the bulk equations (2.8-2.10) are assumed to hold on the interfaces. Equation (2.10) ensures that, the parallel-to-the-interface component of the electric field $E_{||}$ and therefore the scalar potential Φ are continuous at the interfaces. Φ, being continuous, can be used as one of the fields in the differential equation (2.8). The relative displacement $\mathbf{u}$ should also be continuous at the interfaces, in order to be consistent with the validity of the differential equations. These boundary conditions, together with the continuity of D_z implied by equation (2.11), are sufficient to determine the phonon modes in the quantum well considered here. By integrating equation (2.8) across the interfaces, additional connection rules can be obtained which would be required to treat additional phonon modes such as TO phonons. Nash showed [14] that for LO phonons the above connection rules reduce to the the continuity of Φ, D_z and $\rho^{-1/2}w_z$, by taking into ac-

count discontinuities produced to the relative displacement and its derivatives by rapidly decaying vibrations associated with the assumptions of the model for the form of the dispersion. Nash's analysis is based on the Euler-Lagrange equations derived from the appropriate Lagrangian including isotropic bulk dispersion. Equations (2.8-2.11) coincide with the bulk Euler-Lagrange equations of [14]. In the present calculations, the applied boundary conditions are as in [14] with the only difference being that the continuity of u_z is approximated by the continuity of w_z. This approximation is not very crude because the ratio of the square roots of the reduced mass densities for GaAs and AlAs, $\rho^{1/2}_{GaAs}/\rho^{1/2}_{AlAs}$, is ~ 1.3, and the MDCM can be considered equivalent to that of [14]. The derived connection rules do not contradict those of the non-dispersive theory. The effect of the additional connection rule is simply to lift the degeneracy of the modes and, at small $k_{||}$, to govern the mixing between interface and reformulated modes.

It is convenient to measure z from the middle of the quantum well because the system is symmetrical about the plane $z = 0$. Consequently, we find modes for which $\Phi(z)$ is even (even modes) and modes for which $\Phi(z)$ is odd (odd modes). The matching conditions and determinental consistency conditions are easily derived in both cases. Let d be the half-width for the GaAs layer. Then the consistency conditions for even and odd modes are respectively:

$$k_n tan(k_n d)\alpha = k_{||} tanh(k_{||} d)\frac{\varepsilon_2 a_1 - \varepsilon_1 a_2}{\varepsilon_1 + \varepsilon_2 tanh(k_{||} d)} \qquad (2.17)$$

and

$$k_n cot(k_n d)\alpha = -k_{||} coth(k_{||} d)\frac{\varepsilon_2 a_1 - \varepsilon_1 a_2}{\varepsilon_1 + \varepsilon_2 coth(k_{||} d)} \qquad (2.18)$$

where k_n is given by (2.14) in the GaAs layer with $b_L \neq 0$.In these equations

$$\varepsilon_j = \varepsilon_{\infty j}\frac{\omega_{Lj}^2 - \omega^2}{\omega_{Tj}^2 - w^2} \qquad (2.19)$$

$$a_j = (\frac{\varepsilon_{oj} - \varepsilon_{\infty j}}{4\pi})^{\frac{1}{2}}\frac{\omega_{Tj}}{\omega_{Tj}^2 - \omega^2} \qquad (2.20)$$

$$\alpha = \left(\frac{\varepsilon_{o2} - \varepsilon_{\infty 2}}{4\pi}\right)^{\frac{1}{2}} \frac{\omega_{T2}}{\omega_{T2}^2 - \omega^2 - b_L^2 k^2} \tag{2.21}$$

with j=1,2 denoting AlAs and GaAs respectively.

The solutions of (2.17) and (2.18) as a function of $k_{||}$ give the dispersion relation for each mode. Once this is obtained the coefficients in (2.16) can be determined.

2.4 Results and Discussion.

The values of the parameters for bulk GaAs and AlAs used in our calculations are given in Appendix A. We set $d = 50\AA$ and begin by discussing the non-dispersive limit when $b_L \rightarrow 0$. There are two possibilities allowed by equations (2.17) and (2.18). In the first case k_n remains finite. Then we see from (2.14) that $\omega \rightarrow \omega_{L2}$ and from (2.19) that $\varepsilon_2 \rightarrow 0$. Hence (2.17) and (2.18) reduce to

$$k_n tan(k_n d) = -k_{||} tanh(k_{||} d) \tag{2.22}$$

$$k_n cot(k_n d) = k_{||} coth(k_{||} d) \tag{2.23}$$

which determine k_n uniquely. The corresponding potential functions are shown by solids lines in figure 2.1(a) for $k_{||}d = 0.05\pi$ and in figure 2.1(b) for $k_{||}d = 0.5\pi$. The dashed lines show the results obtained in the microscopic calculations of Huang and Zhu [15]. Where the microscopic model curves are omitted, it is because they are indistinguishable from the results of our macroscopic model on the scale of the graphs. The dotted lines show a rough analytical fit to the microscopic results which are described in [15]. We see that the model used here provides an almost perfect fit to the microscopic results. These modes with finite k_n were first proposed by Dharssi [25] without recourse to the limiting procedure used here. The argument was open to the objection that the propagating modes are infinitely degenerate when there is no dispersion, so that there is no reason to take just two propagating waves in (2.16). This difficulty is removed by first putting dispersion in so that k_n is uniquely defined and then letting $b_L \rightarrow 0$ so

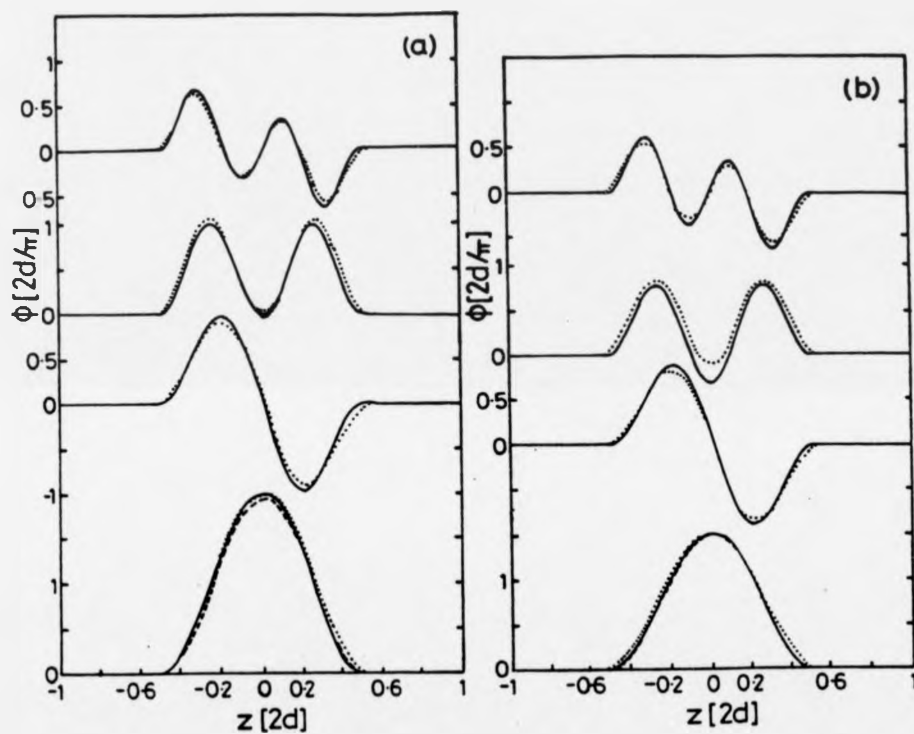

Figure 2.1: Scalar potential as predicted by MDCM in the dispersionless limit
The potential functions for (a) $k_{\parallel}d = 0.05\pi$ and (b) $k_{\parallel}d = 0.5\pi$ predicted by (i) the MDCM in the dispersionless limit (full lines) (ii) Huang and Zhu's microscopic model in the dispersionless limit (dashed lines) (iii) Huang and Zhu's macroscopic model (dotted lines).

as to simplify the results. We see that all the modes are confined to the GaAs layer. Moreover, it is easy to verify that $\partial\Phi/\partial z$ (and hence w_z) vanishes at the interfaces as well as Φ. The values of k_n when $k_{||} \rightarrow 0$ may be determined from (2.22) and (2.23). They are $k_n = n\pi/2d$ with $n = 2, 4, 6, ..$ for the even modes and $n \sim 3, 5, 7, ...$ for the odd modes. Huang and Zhu obtain the same results and give exact values of n in the odd case [15].

The second possibility when $b_L \rightarrow 0$ is that k_n diverges, because $\omega \neq \omega_{L2}$. When $\omega > \omega_{L2}$ we see from (2.14) that k_n becomes purely imaginary as well as having a magnitude which tends to infinity. Consequently, the left-hand sides of (2.17) and (2.18) both diverge so that the dispersion relations reduce to

$$\varepsilon_1 + \varepsilon_2 tanh(k_{||}d) = 0 \tag{2.24}$$

$$\varepsilon_1 + \varepsilon_2 coth(k_{||}d) = 0 \tag{2.25}$$

These are just the dispersion relations of the interface modes of the DCM which Huang and Zhu find are reproduced by their microscopic calculations in the non-dispersive limit [15]. When $\omega < \omega_{L2}$, k_n remains real but becomes infinitely large so that equations (2.24) and (2.25) are satisfied again. Considering equations (A.1) and (A.6) together with the conditions (2.24) and (2.25) when $k_n \rightarrow \infty$, we find again a z-variation of the scalar potential appropriate to interface vibrations of the type given in equation (2.4).

The above discussion shows that there is a sharp distinction between interface and confined modes in the dispersionless limit. We turn now to the case when the GaAs dispersion is kept finite and show that the modes are hybrids, having both interface and confined phonon character. Figure 2.2a shows the dispersion curves for even modes which are the solutions of equation (2.17). The potential functions are presented in figure 2.3 for $k_{||}d = 0.05\pi$ (figure 2.3a) and $k_{||}d = 0.5\pi$ (figure 2. 3b). At high frequencies the even modes have dispersion curves which are parabolic (figure 2.2a) and potential functions which are confined (figure 2.3). The potential functions do not differ significantly from those shown in figure 2.1 for the dispersionless limit. On the other hand, we see

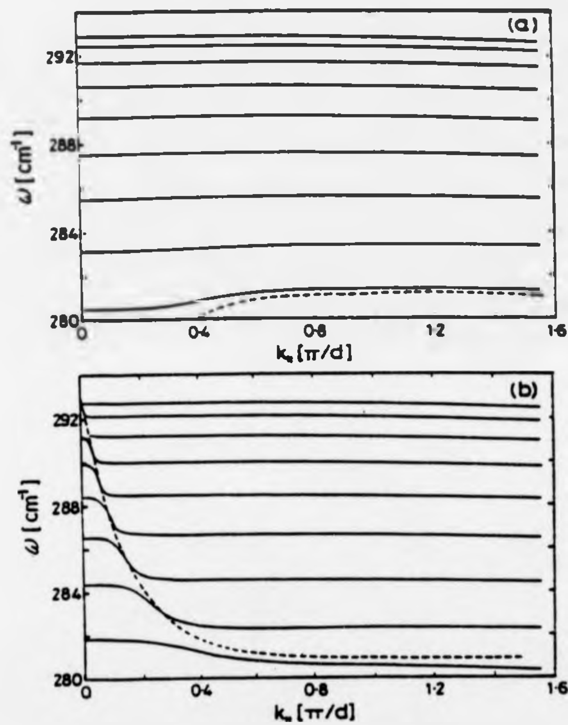

Figure 2.2: Dispesion curves for LO phonon modes.

The dispersion curves (full lines) for (a) even modes and (b) odd modes. The dashed curves are the dispersion curves for the corresponding interface phonons in the DCM.

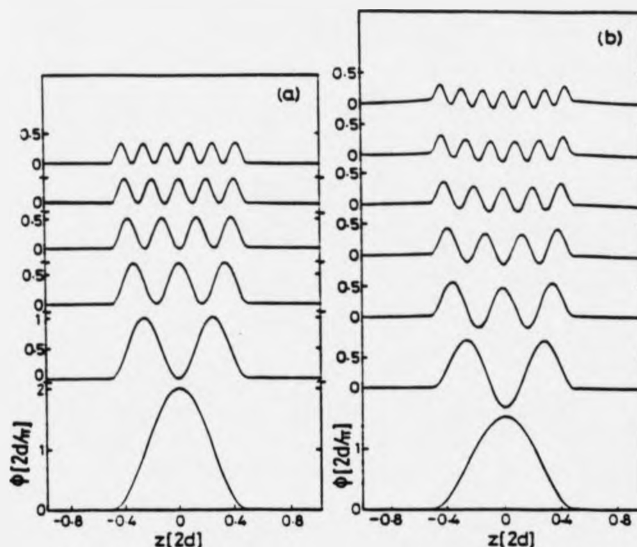

Figure 2.3: Scalar potential for even modes.
The potential functions for even modes for (a) $k_{\|}d = 0.05\pi$ and (b) $k_{\|}d = 0.5\pi$.

in figure 2.2a that for modes with a frequency approaching $(\omega_{LO2} + \omega_{TO2})/2$ the parabolic dispersion is distorted. The distortion is due to the interface vibration admixture which increases with $k_{\|}$ because the dispersion curve comes closer to that for the even interface phonon (dashed curve in figure 2.2a) when $k_{\|}d = 0.5\pi$. This behaviour is particularly clear for the last mode in figure 2.2a. Another result of the increase of the interface admixture with $k_{\|}$ is that for $k_{\|}d = 0.5\pi$, the modes after the sixth leak into the AlAs (see figure 2.3b) which does not happen when $k_{\|}d = 0.05\pi$. Finally, we note that in the long-wavelength limit $k_{\|} \rightarrow 0$ equation (2.17) gives $k_n = n\pi/2d$, $n = 2, 4, 6, \ldots$ in agreement with the theory in the dispersionless limit.

Figure 2.2b shows the dispersion curves for odd modes which are the solutions of equation (2.18). The potential functions are presented in figure 2.4 for $k_{\|}d = 0.05\pi$ (figure 2.4a) and $k_{\|}d = 0.5\pi$ (figure 2.4b). We see by inspection of figure 2.2b that, for large $k_{\|}$, the dispersion is again almost parabolic. The corresponding modes (figure 2.4b) are confined and have potential functions close to those predicted in the dispersionless limit. The odd modes with lower fre-

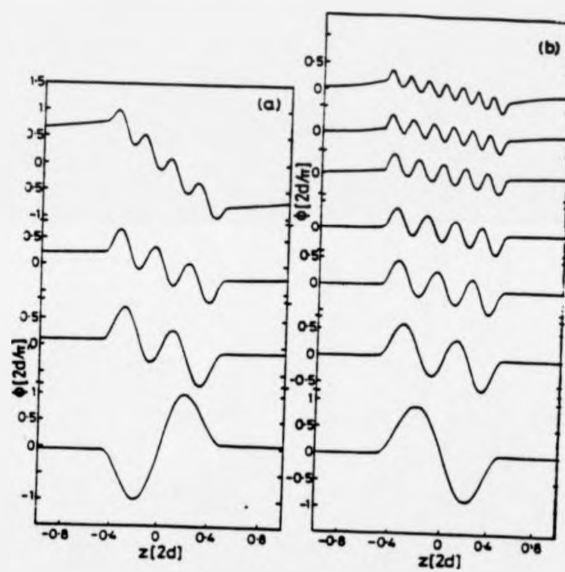

Figure 2.4: Scalar potential for odd modes.

The potential functions for odd modes for (a) $k_{\|}d = 0.05\pi$ and (b) $k_{\|}d = 0.5\pi$.

quency, closer to $(\omega_{LO2} + \omega_{TO2})/2$, begin to leak into the AlAs layers and show stronger interface character. As $k_{\|}$ becomes smaller the parabolic dispersion is distorted. The distortion follows the odd interface phonon dispersion curve [21] which is plotted as a dashed line in figure 2.2b. The number of modes that acquire interfacial character is larger for $k_{\|}d = 0.05\pi$ than for $k_{\|}d = 0.5\pi$, because the odd interface phonon is more dispersive for small $k_{\|}$. The dispersion curves for the odd modes are almost horizontal straight lines when $k_{\|}$ is large because b_L is rather small in GaAs. If these lines are extrapolated to $k_{\|} = 0$ we find points of intersection with the dashed curve for the corresponding interface phonon. Strong admixture of the confined and interface character of the true modes occurs near these points. Moreover, we see that the true dispersion curves bend up there and, when $k_{\|} \rightarrow 0$,they follow the extrapolated dispersion curves for the confined mode with one less node. (In this limit, equation (2.18) gives $k_n = n\pi/2d$, $n = 3, 5, 7, ...$ We note that n assumes **exactly** odd values and not **approximately** odd integer values as in the dispersionless limit).

The above discussion indicates that for both even and odd modes, when $k_{\|} \rightarrow 0$ the eigenvalues of reformulated modes tend to those of the guided modes, as can be deduced from equation (2.7) and the associated boundary conditions. When $k_{\|} >> k_n$, $k_n L/\pi$ tends to an integer. In this regime the interface vibrations are rapidly varying with respect to z, and the reformulated slab vibrations tend towards the slab vibrations (see equation (2.3) and associated boundary conditions). Both in the small and in the large $k_{\|}$ regimes, the frequency depends only weakly on $k_{\|}$. The crossover between the two regimes is identical to the interface-mode dispersion curve calculated in the absence of bulk dispersion. It is remarkable that when (2.24) and (2.25) are satisfied, equations (A.1), (A.6) give potential functions varying as interface vibrations modulated by a k_n-dependent amplitude. The dispersive behaviour of the antisymmetric modes in the crossover regime can be considered as due to the interaction of the bulklike modes with the GaAs antisymmetric interface mode. This behaviour is particularly clear at high values of k_n. In [14] it is shown that the electron-phonon scattering by guided vibrations or reformulated slab

slab vibrations is very weak at large k_n; thus the scattering by large k_n modes is strong only in the crossover regime in which the modes have a large projection onto the interface vibrations.

The interface mode no longer exists as a distinct branch in the presence of bulk dispersion because of the interface/bulklike interaction. In RB theory this mixing is absent because not all the waves are included in the formalism of [28]. In fact, the interface waves are excluded as solutions in the step leading to (2.16) of [28]. Moreover, $\Phi \propto f$ in RB theory which is incorrect when dispersion is included as equation (2.15) shows, and leads in the exclusion of electrostatic boundary conditions in the theory.

RB argued that the Fuchs and Kliewer interface modes correspond to polaritons and, being a dressed electromagnetic wave in materials, they do not possess a scalar potential and should therefore be excluded from the model for LO phonons. Zhu in [10] shows that this argument is not correct. An electric field can be divided into two parts: a longitudinal field E_l which is irrotational and a transverse field E_t which is solenoid. The longitudinal field is related to a non vanishing scalar potential unless the induced charge density is identically zero. In an inhomogeneous layered structure, although the electric field associated with the interface polariton satisfies the relation $\nabla \cdot \mathbf{E} = 0$ within each layer, owing to continuity of D_z at the interfaces and the different dielectric constants of GaAs and AlAs, E_z and P_z are discontinuous across the interfaces. Therefore, there must be a polarization interface charge density, and looking the structure as a whole, $\nabla \cdot \mathbf{E} \neq 0$. It is the interface polarization charge density that results in the scalar potential and the longitudinal electric field.

In a complete theory of optical phonon modes, electromagnetic retardation should be included. This can be done by keeping the magnetic field energy contribution in the Lagrangian of the problem and by dropping the irrotational conditions for the electromagnetic field in Maxwell's equations. The non-retarded theory agrees well with the retarded theory in a heterostructure, provided the boundary conditions, the phonon modes, and finally the electron scattering rates, are the same. These conditions are not generally satisfied, but

in the cases where they are, the non-retarded theory can safely be used. We have ignored retardation throughout our calculations for the following reason. The space scale of the system is set by the width of the GaAs layer which is typically $100\mathring{A}$. An electromagnetic wave will traverse this distance in the order of 10^{-17}s which is much less than the period (10^{-13}s) of the LO phonons with which we are concerned (e.g. [27]). It has also been shown in microscopic calculations of the polaritons in superlattices [27] of period L that, since $k_0 = \omega_{TO}/c$ is small compared with the size of the superlattice Brillouin zone ($2\pi/L$), even in the region of $k_{||} < k_0$, the retardation will only slightly affect the macroscopic Coulomb potential. When $k_{||}$ is much larger than k_0, the potential will be almost unchanged.

Retardation can be incorporated in the macroscopic theory as indicated at the beginning of last paragraph. Continuum model calculations [14] show that retardation does not introduce additional boundary conditions, and that there is one-to-one correspondence as far as the phonon mode branches are concerned. Retardation does not affect the LO phonons at all, but the TO phonons may be seriously altered [14, 10]. The interface phonons of the retarded theory coincide with those found in the dispersionless DCM for all values of $k_{||}$ except those which yield modes which are close to the light line. Retardation effects introduce additional structure in the dispersion curves which is very difficult to observe by Raman scattering, because it is very strongly dispersive and occupies a very small area of the $k_{||}/\omega$ space, resulting in a small integrated scattering strength. One can therefore conclude that both microscopic and continuum calculations agree that a non-retarded theory is suitable in describing optical phonons in heterostructures and the discrepancies, when they occur, have negligible effects on electron-phonon scattering.

Chapter 3

Electron transport: theoretical considerations

3.1 The transport coefficients

The physical processes that accompany the motion of charge carriers in a 2DEG under temperature gradients and internal or external fields are called transport phenomena. The equilibrium electron distribution is perturbed by the application of external stimuli resulting in the flow of macroscopic currents. Assuming that these stimuli are small, we can relate them linearly to the electric and heat current densities, **J** and **Q** respectively, by the macroscopic transport equations [31]:

$$\mathbf{J} = \sigma \mathbf{E}' + L\nabla T \tag{3.1}$$

$$\mathbf{Q} = M\mathbf{E}' + N\nabla T \tag{3.2}$$

where $\mathbf{E}'$ is the electromotive force and ∇T is the temperature gradient (both in the xy plane). The electromotive force $\mathbf{E}'(= \mathbf{E} + |e|^{-1}\nabla\mu)$ is equal to the external electric field **E** for steady homogeneous situations in which the gradient of the chemical potential μ vanishes.

The coefficients σ, L, M, N are usually calculated in transport theory. How-

ever, in experiments it is usually easier to fix **J** and ∇T and measure **E** and **Q**. It is therefore convenient to rewrite the above equations as:

$$\mathbf{E}' = \rho \mathbf{J} + S\nabla T \tag{3.3}$$

$$\mathbf{Q} = \pi \mathbf{J} - K\nabla T \tag{3.4}$$

The expressions for the resistivity ρ, the thermoelectric power S, the Peltier coefficient π and the thermal conductivity K in terms of σ,L,M,N are:

$$\rho = \sigma^{-1} \tag{3.5}$$

$$S = -\sigma^{-1} L \tag{3.6}$$

$$\pi = M\sigma^{-1} \tag{3.7}$$

$$K = M\sigma^{-1} L - N \tag{3.8}$$

In general, these coefficients are second order tensors. In the absence of magnetic fields and for 2DEGs which are isotropic in the xy plane, the transport coefficients reduce to scalars.

3.2 Two-dimensional Boltzmann transport theory

The transport coefficients are determined by the perturbed electron distribution which is described statistically by the probability f(**k**,**r**,t) of an electron occupying a state with wave vector **k** and a given spin orientation in the neighborhood of the point **r** at time t. Then, for a 2DEG, the electric and heat current densities are given for single subband occupation by [31, 32]:

$$\mathbf{J} = -\frac{e}{2\pi^2} \int f\mathbf{v}(\mathbf{k}) d\mathbf{k} \tag{3.9}$$

$$\mathbf{Q} = \frac{1}{2\pi^2} \int f\mathbf{v}(\mathbf{k})[\varepsilon(k) - \varepsilon_f] d\mathbf{k} \tag{3.10}$$

where ε_f is the Fermi energy, $\varepsilon(k)$ is the energy of the ground subband and $\mathbf{v}(\mathbf{k})$ is the associated group velocity.

The perturbed electron distribution $f(\mathbf{k}, \mathbf{r}, t)$ obeys a continuity equation that expresses the conservation of electrons as they follow semiclassical trajectories in $\mathbf{k}$, $\mathbf{r}$ space.

$$\frac{\partial f}{\partial t} + \mathbf{v} \cdot \nabla_{\mathbf{r}} f + \dot{\mathbf{k}} \cdot \nabla_{\mathbf{k}} f = (\frac{\partial f}{\partial t})_c \tag{3.11}$$

where $\nabla_{\mathbf{r}} = (\frac{\partial}{\partial x}, \frac{\partial}{\partial y})$, $\nabla_{\mathbf{k}} = (\frac{\partial}{\partial k_x}, \frac{\partial}{\partial k_y})$.

The right hand side of equation (3.11) is the rate of change of the distribution function f due to collisions. The Boltzmann equation (3.11) represents the competition between the applied fields which tend to drive the system away from equilibrium and scattering (contained within the collision term) which tends to restore it. The collision term has the form:

$$(\frac{\partial f}{\partial t})_c = (\frac{\partial f}{\partial t})_s + (\frac{\partial f}{\partial t})_{\alpha(e)}. \tag{3.12}$$

where the first term of the right hand side is due to static imperfections and the second is due to phonon absorption and emission. In sufficiently small external fields the electrons move according to the following semiclassical equations.

$$\hbar \dot{\mathbf{k}} = e[\mathbf{E} + \mathbf{v}(\mathbf{k}) \times \mathbf{B}] \tag{3.13}$$

and

$$\mathbf{v}(\mathbf{k}) = \hbar^{-1} \nabla_{\mathbf{k}} \varepsilon(\mathbf{k}) \tag{3.14}$$

where $\mathbf{E}$ and $\mathbf{B}$ are the applied electric and magnetic field respectively. In this chapter and in the following chapter we use these equations to study the effects of an external electric field and temperature gradient in the xy plane and in

chapter 5 we also study the effect of a magnetic field perpendicular to the xy plane.

Since the applied electric fields and temperatures gradients are small, we assume that they cause a small perturbation to both the electron distribution f and the phonon distribution function $N_{\mathbf{Q}}$, which we can write as :

$$f^1 = f - f^o \tag{3.15}$$

and

$$N^1_{\mathbf{Q}} = N_{\mathbf{Q}} - N^o_{\mathbf{Q}} \tag{3.16}$$

where f^o and $N^o_{\mathbf{Q}}$ are the distributions in thermal equilibrium.

A relaxation time, $\tau(\varepsilon)$, is associated with the electron scattering by static imperfections and another, $\tau_p(Q)$, with the phonon scattering by the boundaries and by static defects. For weak electron-phonon interaction it can be shown that [33, 34]:

$$(\frac{\partial f}{\partial t})_c = -\frac{f^1}{\tau(\varepsilon)} + U(\mathbf{k}) \tag{3.17}$$

where

$$U(\mathbf{k}) = \frac{1}{k_B T} \sum_{\mathbf{k}'\mathbf{Q}} \frac{1}{F} \frac{dN^o_{\mathbf{Q}}}{\partial d\hbar\omega_{\mathbf{Q}}} \frac{\hbar\omega_{\mathbf{Q}}}{T} \mathbf{v_p} \cdot \nabla_{\mathbf{r}} \mathbf{T} (\Gamma_{\mathbf{k}'\mathbf{k}} - \Gamma_{\mathbf{k}\mathbf{k}'}), \tag{3.18}$$

and

$$F = -\frac{dN^o_{\mathbf{Q}}}{d\hbar\omega_{\mathbf{Q}}} \frac{1}{\tau_p(\mathbf{Q})}. \tag{3.19}$$

Here:

$$\Gamma_{\mathbf{k}'\mathbf{k}} = f^o_{\mathbf{k}}(1 - f^o_{\mathbf{k}'}) P^{ao}_{\mathbf{k}\mathbf{k}'}(\mathbf{Q}) \tag{3.20}$$

is the average rate of absorption of phonons of wave vector $\mathbf{Q}$ resulting in electron transitions from $\mathbf{k}$ to $\mathbf{k}'$ when the whole system is in thermal equilibrium. In accordance with the standard methods for solving the linearized Boltzmann equation, use has been made of the detailed balance relationship to simplify the formulae by expressing the phonon emission term in terms of the phonon

absorption term [32, 33]. $\hbar\omega_{\mathbf{Q}}$ and $\mathbf{v_p}$ are respectively the phonon energy and velocity. An explicit expression for the rate $P^{ao}_{\mathbf{kk'}}(\mathbf{Q})$ at which the electron will transfer from $\mathbf{k}$ to $\mathbf{k}'$ by absorbing one phonon with wave-vector $\mathbf{Q}$ is given in the last section of this chapter.

In response to an in-plane electromotive force $\mathbf{E}$ and an in-plane temperature gradient ∇T, the linearized Boltzmann equation for the electrons can be written as:

$$-\frac{f^1}{\tau(\varepsilon)} - \mathbf{v}\cdot\nabla_{\mathbf{r}} f^o - \frac{e}{\hbar}\mathbf{E}\cdot\nabla_{\mathbf{k}} f^o + U(\mathbf{k}) = 0 \tag{3.21}$$

where the charge on the electron is denoted by e which is negative. Equation (3.21) is solved in Appendix B. For weak electron-phonon interactions the external fields and the electron-phonon interaction contribute independently to the perturbation of the electron distribution. By 'weak' it is meant that the electron scattering rate due to impurities is much greater than that due to phonons absorption or emission. For the phonons, the scattering rate from the boundaries and from the phonons must be greater than that from the electrons. The solution of (3.21) can be formally written as:

$$f^1 = f^1_d + f^1_g \tag{3.22}$$

where the diffusion and phonon drag terms are respectively given by the following equations:

$$f^1_d(\mathbf{k}) = -\frac{df^o}{d\varepsilon}\tau(\varepsilon)\mathbf{v}\cdot[e\mathbf{E} - (\varepsilon - \varepsilon_f)\frac{\nabla_{\mathbf{r}} T}{T}] \tag{3.23}$$

and

$$f^1_g(\mathbf{k}) = \tau(\varepsilon)U(\mathbf{k}) \tag{3.24}$$

3.3 Electron screening

Many media respond to an applied field so that carrier redistribution cancels the electric field at large distances. The carriers increase in number where their

potential energy is lowered and decrease in number where their potential energy is raised.

Due to the electron-electron interaction, the bare potential $V^b(\mathbf{r})$ is converted into the screened potential $V(\mathbf{r})$. To calculate $V(\mathbf{r})$, the perturbation in the electron density can be described by an expansion in terms of the set of unperturbed electron states. For a strict 2DEG confined to $z = 0$ a simple relation between V and V^b can be written down in Fourier space [2]:

$$V(\mathbf{q}) = V^b(\mathbf{q})/\epsilon(\mathbf{q}) \tag{3.25}$$

where $V(\mathbf{q})$ and $V^b(\mathbf{q})$ are the 2D Fourier transforms of $V(\mathbf{r})$ and $V^b(\mathbf{r})$ respectively and $\epsilon(\mathbf{q})$ is the static dielectric function.

The Thomas-Fermi approximation provides the simplest way to approach the screening problem [37]. The electrochemical potential $\mu_{ec}(\mathbf{r}) = \varepsilon_f(\mathbf{r}) - e\Phi(\mathbf{r})$ of an electron in the potential $V(\mathbf{r})$ is approximated by a constant value of ε_f at $T = 0$ K. For a 2DEG the result is:

$$\epsilon(q) = 1 + q_s/q \tag{3.26}$$

where the Thomas-Fermi screening wave vector q_s is obtained from:

$$q_s = \frac{g_v e^2 m^*}{2\pi\kappa\epsilon_o \hbar^2}, \tag{3.27}$$

where κ is the relative permitivity of the 3D host, g_v is the valley degeneracy and m^* is the electron in-plane effective mass. It is remarkable that the predicted screening is independent of the electron density when stronger screening is expected at high compared to low electron densities. This problem is resolved in the Random Phase Approximation (RPA) which leads to the Lindhart dielectric function [38],

$$\epsilon(q) = 1 + \frac{q_s}{q}\xi(q) \tag{3.28}$$

with

$$\xi(q) = \begin{cases} 1 & q \le 2k_f \\ 1 - (1 - (2k_f/q)^2)^{1/2} & q > 2k_f \end{cases} \tag{3.29}$$

Each electron is assumed to move in an unscreened potential plus a potential which is induced by the redistribution of all the electrons and is obtained from the solution of Poisson's equation. The RPA remains valid at large q and reduces to the Thomas-Fermi result at small q. The electrons are assumed to respond as free particles to the mean field. In reality, the electrons are not free and the field seen locally is not the mean value. Many improvements have been suggested and the shorter range exchange and correlation interactions can be included [2, 39]. These effects are of minor importance in transport calculations [2, 36, 40].

In a quasi-2DEG the finite well width must be allowed for. Translational invariance is retained only in the xy-plane. Moreover, since the z dependence of the perturbed electron density is conveniently expanded in the set $\phi_\alpha(z)$, all the subbands are included in the screening whether they are occupied or not. These ideas lead to the result of Siggia and Kwok [41] that:

$$V^b_{\alpha\beta} = \sum_{\mu,\lambda} \epsilon_{\alpha\beta\mu\lambda}(\mathbf{q}) V_{\mu\lambda}(\mathbf{q}) \tag{3.30}$$

where

$$V_{\alpha\beta}(\mathbf{q}) = \langle \alpha, \mathbf{k} + \mathbf{q} | V(\mathbf{r}) | \beta, \mathbf{k} \rangle \tag{3.31}$$

and is equal to the matrix element between subbands α and β of the 2D Fourier transform of $V(\mathbf{r})$. The quantity $V^b_{\alpha\beta}(\mathbf{q})$ has the same interpretation in terms of $V^b(\mathbf{r})$.

The elements $\epsilon_{\alpha\beta\mu\lambda}$ in equation (3.30) are given by:

$$\epsilon_{\alpha\beta\mu\lambda}(\mathbf{q}) = \delta_{\mu,\alpha}\delta_{\lambda,\beta} - V^c F_{\alpha\beta\mu\lambda}(\mathbf{q}) \Pi_{\mu\lambda}(\mathbf{q}) \tag{3.32}$$

In (3.32) the multisubband polarizability is:

$$\Pi_{\mu\lambda}(\mathbf{q}) = \lim_{\eta \to 0^+} \frac{2g_v}{A} \sum_{\mathbf{k}} \frac{f_\lambda(\mathbf{k}) - f_\mu(\mathbf{k}+\mathbf{q})}{\varepsilon_\lambda(\mathbf{k}) - \varepsilon_\mu(\mathbf{k}+\mathbf{q}) + i\eta}, \tag{3.33}$$

and the form factor is given by:

$$V^c F_{\alpha\beta\mu\lambda}(\mathbf{q}) = \int g(\mathbf{q}, z, z')\phi^*_\alpha(z)\phi_\beta(z)\phi_\mu(z')\phi^*_\lambda(z')dzdz' \tag{3.34}$$

where $g(\mathbf{q}, z, z')$ is the 2D Fourier component of the Coulomb interaction between electrons at z and z'. The quantity $V^c F_{\alpha\beta\mu\lambda}(\mathbf{q})$ is the average of $g(\mathbf{q}, z, z')$ weighted by the α-th and β-th subbands electron distribution over z and z'. In the pure 2DEG limit the denominators of all $\Pi_{\mu\lambda}(\mathbf{q})$ become very large except for $\Pi_{11}(\mathbf{q})$ and only the case $\alpha = \beta = 1$ is of interest. Hence, only $\epsilon_{1111}(\mathbf{q})$ is significant. Moreover, the form factor $F_{1111}(\mathbf{q})$ tends to unity in the 2D limit. Thus the 2D result is recovered. The single subband approximation (SSA) gives for the quasi-2D dielectric function:

$$\epsilon_s(\mathbf{q}) = 1 - V^c\Pi(\mathbf{q})F_{1111}(\mathbf{q}) = 1 + \frac{q_s}{q}\xi(\mathbf{q})F_{1111}(\mathbf{q}) \tag{3.35}$$

The SSA is commonly used because of its simplicity. The validity of this approximation is discussed for the Si-MOSFET by Smith [35] and for the GaAs/AlGaAs heterojunction by Tang [42].

At low temperatures, the dielectric function can be approximated by its value at $T = 0$ K:

$$\epsilon(q) = 1 + \frac{e^2}{2\epsilon_o\kappa q}F(q)\Pi_o(q) \tag{3.36}$$

where $\Pi_o(q)$ is the static polarizability in the extreme quantum limit:

$$\Pi_o(q) = \frac{g_v m^*}{\pi\hbar^2}\xi(q) \tag{3.37}$$

The wavevector dependence of the normalized polarizability associated with the dielectric response is shown in figure 3.1. At $q = 2k_f$ the polarizability

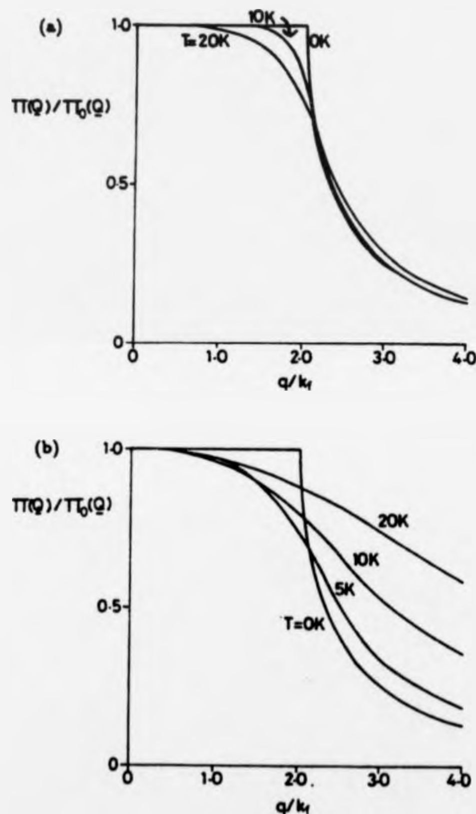

Figure 3.1: 2D polarizability at finite T in Si and GaAs.

Plots of $\Pi(q)/\Pi_o(q)$ against q for $N_s = 2 \times 10^{15} m^{-2}$ in (a) GaAs and (b) Si for a range of temperatures T.

decreases steeply. F(q) is the form factor in the SSA, which for the Fang-Howard wavefunction is:

$$F(q) = \frac{1}{16}(1 + \frac{\kappa_{ins}}{\kappa_{sc}})(1 + \frac{q}{b})^{-3}(8 + 9\frac{q}{b} + 3\frac{q^2}{b^2}) + \frac{1}{2}(1 - \frac{\kappa_{ins}}{\kappa_{sc}})(1 + \frac{q}{b})^{-6} \quad (3.38)$$

where κ_{ins} and κ_{sc} are respectively the dielectric constants of the insulator and the semiconductor. The temperature dependence of the screening is determined by the polarizability. At $T = 0$ K this has been evaluated by taking the zero temperature value of the Fermi function. At higher T, the finite T value of the Fermi function can be written as [43]:

$$f(\varepsilon, \varepsilon_f) = \frac{1}{4k_B T} \int_0^\infty d\mu \frac{f_o(\varepsilon, \mu)}{cosh^2[(\varepsilon_f - \mu)/(2k_B T)]} \tag{3.39}$$

Using the definition of $\Pi_o(q)$, and transforming the sum over wavevectors **k** to an integral, but performing the integrals over **k** and μ in reverse order, we get:

$$\Pi(q, \varepsilon_f, T) = \frac{1}{4k_B T} \int_0^\infty d\mu \frac{\Pi(q, \mu, 0)}{cosh^2[(\varepsilon_f - \mu)/(2k_B T)]} \tag{3.40}$$

Consequently, $\xi(q)$ in (3.29) can be replaced by:

$$\xi(q) = \frac{1}{e^{\varepsilon_f / k_B T} + 1} - \alpha \int_0^1 dx \frac{x^2}{cosh^2[a(x^2 - b)]} \tag{3.41}$$

where $\alpha = (\hbar^2 q^2)/(16 m^* k_B T)$ and $b = 1 - (2k_f/q)^2$. The important feature of thermal broadening is the rounding of the sharp corner in the polarizability at $q = 2k_f$ and therefore a diminished screening of the scattering potentials. For $q = 2k_f$ the effect of finite temperature is greatest (figure 3.1). Away from $2k_f$ the change in polarizability is much less. For $q > 2k_f$ the polarizability is slightly increased and for $q < 2k_f$ it is decreased. The resultant effect depends on the mean value of q, denoted by $\bar{q}$. For low T, $\bar{q} < 2k_f$ and $k_B T/\varepsilon_f$ is reduced so that $\Pi(q) \to \Pi_o(q)$. When N_s becomes higher, $k_B T/\varepsilon_f$ is further reduced and the effect of finite T on screening is even smaller.

3.4 Electron scattering by static defects.

The electrons in inversion layers are scattered by defects and phonons. At very low temperatures the role of phonons is negligible and they can safely be ignored. Scattering from defects such as charged impurities or irregularities in the interface will then dominate, and may be treated in the Born approximation. The relevant formalism is presented in this section.

3.4.1 Ionized impurity scattering.

The problem of elastic electron scattering by ionized impurities in the electric quantum limit has been formulated by Stern and Howard [44] and is treated here following their approach. We assume that the impurity charge is $\pm e$.

Using the image method, the two-dimensional Fourier transform of the effective potential for electrons in the inversion layer is given by:

$$U_q = \frac{e^2}{2\epsilon_o \kappa q} F(q, z_i) \tag{3.42}$$

where for impurities located on a plane $z = z_i$ with $z_i < 0$,

$$F(q, z_i) = e^{qz_i} \int_0^\infty dz |\zeta_0(z)|^2 \tag{3.43}$$

and for $z_i > 0$

$$F(q, z_i) = \frac{1}{2} \int_0^\infty dz |\zeta_0(z)|^2 [(1 + \frac{\kappa_{ins}}{\kappa_{sc}}) e^{-q|z-z_i|} + (1 - \frac{\kappa_{ins}}{\kappa_{sc}}) e^{-q(z+z_i)}] \tag{3.44}$$

In (3.42) $\kappa = (\kappa_{sc} + \kappa_{ins})/2$.

The transport relaxation rate for an electron with energy ε, in the Born approximation, is [2]:

$$\frac{1}{\tau(\varepsilon)} = \frac{2\pi}{\hbar} \int dz N_i(z) \sum_{\mathbf{q}} \frac{|U_q^\mu(z)|^2}{\epsilon(q, T)^2} (1 - cos\theta) \delta(\varepsilon(\mathbf{k}) - \varepsilon(\mathbf{k} + \mathbf{q})) \tag{3.45}$$

where $\varepsilon = \frac{\hbar^2 k^2}{2m^*}$, θ is the scattering angle, $N_i(z)$ is the impurity density with

i indicating the location of the ionized impurities, inside or outside of the inversion layer. The form factor can be expressed in terms of the variational wavefunction as follows [2]:

For remote impurities ($z_i < 0$):

$$F(q, z_i) = P_o e^{qz_i} \tag{3.46}$$

For background impurities ($z_i > 0$):

$$F(q, z_i) = [P(z_i) + \delta_k P_o e^{-qz_i}] \tag{3.47}$$

where

$$P(z) = \begin{cases} \frac{b^3}{(b-q)^3}[e^{-qz} - (\alpha_o + \alpha_1 z + \alpha_2 z^2)e^{-bz}] & q \neq b \\ \frac{1}{8}[1 + 2bz + 2b^2z^2 + \frac{4}{3}b^3z^3]e^{-bz} & q = b \end{cases} \tag{3.48}$$

with

$$\alpha_o = \frac{2q(3b^2 + q^2)}{(b+q)^3}, \tag{3.49}$$

$$\alpha_1 = \frac{4bq(b-q)}{(b+q)^2}, \tag{3.50}$$

$$\alpha_2 = \frac{q(b-q)^2}{b+q}, \tag{3.51}$$

$$\delta_k = \frac{\kappa_{sc} - \kappa_{ins}}{\kappa_{sc} + \kappa_{ins}}, \tag{3.52}$$

and

$$P_o = \frac{b^3}{(b+q)^3}. \tag{3.53}$$

Finally, for ionized impurities located on the interface at $z_i = 0$:

$$F(q, z_i) = P_o \tag{3.54}$$

The electron mobility is given by:

$$\mu = \frac{e\tau}{m^*} \tag{3.55}$$

Since the form factor depends on the position of the charged centers, the dependence of the mobility on the electron density also does. Numerical calculations show that the variation is the slowest when the impurities are on the interface and the steepest when they are distributed in the insulator (see chapter 4).

3.4.2 Interface roughness scattering.

Any deviation from the perfect interface causes electron scattering. The nature of interface asperities is not exactly known but they are expected to be more important for interfaces between materials with a lattice mismatch and this is why interface roughness is believed to be higher in a Si-MOSFET than in a GaAs/AlGaAs heterojunction. Because of the incomplete knowledge of the interface structure, the roughness is treated in a simple model described in detail by Ando [2]. This model assumes an infinite barrier at the interface whose position $z = \Delta(\mathbf{r})$ may have a small and slowly varying displacement. The relaxation time is given by:

$$\frac{1}{\tau} = \frac{2\pi}{\hbar} \sum_{\mathbf{q}} \pi \left|\frac{\Delta\Lambda\Gamma(q)}{\epsilon(q,T)}\right|^2 e^{-q^2\Lambda^2/4}(1 - cos\theta)\delta(\varepsilon(k) - \varepsilon(\mathbf{k}+\mathbf{q})) \qquad (3.56)$$

where (assuming a Gaussian form for the correlation of the surface roughness) we obtain for the Fourier transform of the correlation function of $\Delta(\mathbf{r})$:

$$< |\Delta_q|^2 >= \pi\Delta^2\Lambda^2 e^{-q^2\Lambda^2/4} \qquad (3.57)$$

with Δ being the average displacement of the interface and Λ being of the order of its spatial variation in the direction parallel to the interface.

The matrix element is

$$\Gamma(q) = \gamma(q) + \gamma_{im}(q), \qquad (3.58)$$

The first term in equation (3.58) stands for the effective electric field which arises from the positive charges at the gate electrode and those in the depletion layer. The second term is the image term which accounts for the effect of the different dielectric constants of the materials across the interface. We refer to [5] for detailed expressions of the functions in equation (3.58). It is assumed that the rates of simultaneously present scattering mechanisms can be added (Matthiesen's rule). The deviations from this rule with T have been found to be negligible below 10 K and not too low electron densities, for both the Si-MOSFET [45] and the heterojunction [46]. So, the total relaxation rate is given by:

$$\frac{1}{\tau} = \sum_i \frac{1}{\tau_i} \tag{3.59}$$

3.5 Thermopower

The total 2D current density is:

$$J = \frac{2e}{A} \sum_{\mathbf{k}} \mathbf{v} f^1(\mathbf{r}, \mathbf{k}) \tag{3.60}$$

where A is the area of the 2DEG. The thermopower is defined in terms of L and σ which are scalars in the absence of magnetic field:

$$S = -\frac{L}{\sigma} \tag{3.61}$$

The transport coefficients L, σ are deduced by comparing equation (3.60) with the phenomenological equation (3.1).

Equation (3.22) shows that the current and, correspondingly, the transport coefficients arise from two distinct processes: electron diffusion and phonon drag of the electrons. The phonon drag contribution to σ is usually negligible

[47], but phonon drag plays a very important role in thermoelectric transport. The thermopower resulting from these two processes is described here.

3.5.1 Diffusion thermopower

Substituting f_d^1 of equation (3.23) in equation (3.60), it is found that:

$$L = -\frac{|e|}{(2\pi)^2 T}\int \tau(\varepsilon)\frac{df^o}{d\varepsilon}(\varepsilon - \varepsilon_f)v^2 d\mathbf{k} \tag{3.62}$$

and

$$\sigma = -\frac{e^2}{(2\pi)^2}\int \tau(\varepsilon)v^2\frac{df_o}{d\varepsilon}d\mathbf{k}. \tag{3.63}$$

We assume that the 2DEG is isotropic and that the temperature is low. Then, these integrals are easily evaluated [32, 47]. Thus, we find that $\sigma = \sigma(\varepsilon_f)$, where:

$$\sigma(\varepsilon) = \frac{\varepsilon e^2 \tau(\varepsilon)}{\pi\hbar^2} \tag{3.64}$$

is the energy dependent conductivity. Moreover, L is proportional to the derivative of $\sigma(\varepsilon)$ at the Fermi level and (3.64) yields Mott's formula.

$$S^d = -\frac{\pi^2 k_B^2 T}{3e\sigma(\varepsilon_f)}\frac{d\sigma(\varepsilon)}{d\varepsilon}|_{\varepsilon=\varepsilon_f} \tag{3.65}$$

It is convenient to introduce the parameter

$$p = \varepsilon\frac{d\ln\tau}{d\varepsilon}|_{\varepsilon_f} \tag{3.66}$$

The diffusion thermopower can be written:

$$S^d = -\frac{\pi^2 k_B}{3e}\frac{k_B T}{\varepsilon_f}(p+1) \tag{3.67}$$

We see that S^d is negative when $p > -1$ whereas it becomes positive for $p < -1$. This behaviour can be better understood by recalling the procedure followed to obtain Mott's relation. Transforming the integrations in equations (3.62) and (3.63) to energy integrations, it can be seen that:

$$S^d \sim -\int_0^\infty \tau(\varepsilon)h(\varepsilon)d\varepsilon \tag{3.68}$$

with

$$h(\varepsilon) = \frac{\varepsilon(\varepsilon-\varepsilon_f)e^{(\varepsilon-\varepsilon_f)/k_BT}}{(e^{(\varepsilon-\varepsilon_f/k_BT)}+1)^2} \tag{3.69}$$

The function $h(\varepsilon)$ is positive above ε_f and negative below it. When the relaxation time is constant, the positive contribution to the integral is bigger than the negative contribution. When $p > 0$ and τ increases with the energy, higher energies dominate and the above situation is reinforced. When $p < 0$ the relaxation time is larger at low energies and the negative part of the integrand becomes more and more important, resulting in a positive S^d when $p < -1$.

3.5.2 Phonon drag

A formula for the phonon drag contribution, S_g, to the thermopower has been derived in [33], in which the coupled electron and phonon Boltzmann equations are linearized and solved in the relaxation time approximation at low temperatures where only acoustic phonons are important. It is:

$$\begin{aligned} S_g &= \frac{|e|}{\sigma A k_B T^2}\sum_{\mathbf{k}}\sum_{\mathbf{k}'}\sum_{\mathbf{Q},s}\hbar\omega_{\mathbf{Q}s}\tau_{\mathbf{Q}s}f(\mathbf{k})[1-f(\mathbf{k}')]P_{\mathbf{Q}s}(\mathbf{k},\mathbf{k}') \\ &\quad\times(\tau_{\mathbf{k}}\mathbf{v}_{\mathbf{k}}-\tau_{\mathbf{k}'}\mathbf{v}_{\mathbf{k}'})\cdot\nabla_{\mathbf{Q}}\omega_{\mathbf{Q}s} \end{aligned} \tag{3.70}$$

where A is the area of the two-dimensional electron gas, $\hbar\omega_{\mathbf{Q}s}$ is the phonon energy of wave vector $\mathbf{Q}$ and mode s, $\tau_{\mathbf{Q}s}$ is the phonon relaxation time, $f(\mathbf{k})$ is the is the Fermi distribution function, $\tau_{\mathbf{k}}$ is the electron relaxation time, $\mathbf{v}_{\mathbf{k}}$ is the electron velocity and $P_{\mathbf{Q}s}(\mathbf{k},\mathbf{k}')$ is the transition rate for phonon absorption. In this section, we define the quantities involved in equations (3.70) and (3.71) for both the Si-MOSFET and the GaAs/AlGaAs heterojunction and give the final form of S_g, which is evaluated numerically after the sums over $\mathbf{k}$ and $\mathbf{Q}$ have been replaced by integrals. To obtain electron transition rates acoustic phonon scattering is taken into account. Optical phonons are neglected since it is the low temperature limit which is of interest.

The transition rate for the system when one phonon of wave-vector **Q** is absorbed by an electron in state **k** which is promoted to $\mathbf{k}'$ is obtained from the Golden Rule. The result is [33, 36]:

$$P_{\mathbf{Q}_s}(\mathbf{k},\mathbf{k}') = \frac{2\pi}{\hbar}|V_{\mathbf{Q}_s}|^2 N_{\mathbf{Q}_s}\delta(\varepsilon_{\mathbf{k}'} - \varepsilon_{\mathbf{k}} - \hbar\omega_{\mathbf{Q}_s})|Z_{11}(q_z)|^2\delta_{\mathbf{k}',\mathbf{k}+\mathbf{q}} \qquad (3.71)$$

where $N_{\mathbf{Q}_s}$ is the Planck distribution function for the s-th phonon mode of wave vector **Q**, **q** and q_z are the components of the phonon wavevector in the x-y plane and in the z-direction respectively and, $\delta(\varepsilon_{k'} - \varepsilon_k - \hbar\omega_{\mathbf{Q}})$ and $\delta_{\mathbf{k}',\mathbf{k}+\mathbf{q}}$ are the Dirac and Kronecker symbols expressing energy and momentum conservation in the x-y plane respectively. ρ is the density of the material (2.39 g/cm^3 for Si and 5.3 g/cm^3 for GaAs). The overlap integral is [33, 34]:

$$Z_{11}(q_z) = \int \phi^*_{\mathbf{k}'}(z)e^{iq_z z}\phi_{\mathbf{k}}(z)dz \qquad (3.72)$$

where $\phi_{\mathbf{k}}(z)$ is the normalized wavefunction for the z-direction motion in state **k** of the ground subband. For the variational wavefunction it is:

$$Z_{11}(q_z) = b^6/(b^2 + q_z^2)^3 \qquad (3.73)$$

The remaining factor in equation (3.71), $|V_{\mathbf{Q}_s}|^2$, is the square of the matrix element for the electron-phonon interaction. In a Si-MOSFET, electrons are assumed to interact with phonons via a deformation potential. Because of elastic anisotropy the situation is very complicated. Strictly speaking, it is necessary to consider each direction of the phonon wave vector **Q** separately in calculating the transition rate as it has been done by Herring and Vogt in [48]. However, it is possible to adopt a simpler approach which involves an implicit averaging over the azimuthal angle of **Q** and regarding elastic anisotropy as small. Doing so and accounting for both the longitudinal (LA) and the transverse (TA) acoustic phonons the square of the matrix element is taken as [49]:

$$|V_{\mathbf{Q}_s}|^2 = \frac{\hbar\omega_{\mathbf{Q}}}{2\epsilon(q,T)^2\rho c_l^2 V}\begin{cases} \Xi_u^2(q_z^2/Q^2 + D)^2 & LA \\ \Xi_u^2(q^2q_z^2/Q^4) & TA \end{cases} \tag{3.74}$$

Here, V is the volume of the material. Ξ_u is the deformation potential for pure shear strain and $D = \Xi_d/\Xi_u$, with Ξ_d denoting the deformation potential for pure dilation. The values used in the calculations for Si are: $\Xi_u = 9.0eV$ and $\Xi_d = -6.0eV$ [2]. In GaAs, the spherical symmetry of the ground subband prohibits the electrons from interacting with transverse phonons and only longitudinal modes contribute to the drag thermopower. Moreover, shear strains produce no energy change [49]. The value of the deformation potential associated with pure dilation Ξ_d is uncertain. In [46], it is concluded that Ξ_d has to be smaller than 12 eV. In [50] the best fit to experimental values is obtained for $\Xi_d = -11.5 \pm 0.5eV$. It is interesting that practically the same value ($-11.1 \pm 0.1eV$) was obtained by means of a quite different experimental method, the measurements of the energy-loss rate in a 2DEG [51]. In the present calculations $\Xi_d = -11.0$ eV is used. In GaAs, the absence of inversion symmetry introduces, in addition to the deformation potential electron-phonon interaction, the piezoelectric potential interaction. Both longitudinal and transverse phonons contribute to piezoelectric scattering, so that [52, 53]:

$$|V_{\mathbf{Q}_s}|^2 = \frac{\hbar\omega_{\mathbf{Q}}}{2\epsilon(q,T)^2\rho c_l^2 V}\begin{cases} \Xi_d^2 + (eh_{14})^2 A_l/q^2 & LA \\ (eh_{14})^2 A_t/q^2 & TA \end{cases} \tag{3.75}$$

with

$$A_l = \frac{9q_z^2q^4}{2Q^6} \tag{3.76}$$

and

$$A_t = \frac{8q_z^2q^4 + q^6}{2Q^6} \tag{3.77}$$

The value of h_{14} used in the calculations is $1.2 \times 10^9 Vm^{-1}$ [53].

At low temperatures boundary scattering dominates the phonon scattering and if v_s is the phonon velocity and $\tau_p(Q)$ is the phonon relaxation time, then the phonon mean free path is $\lambda_p = v_s \tau_p(Q)$. This equation is used to determine $\tau_p(Q)$ from measured values of λ_p, derived from measured values of the bulk thermal conductivity [37].

When the sums over **k** and **Q** are transformed to integrals the final result for the contribution to S_g^o from mode s is:

$$S_{gs}^o = -\frac{2C_g\tau_f}{\sigma_o} \int\int dq dq_z q^2 F(\mathbf{Q})\lambda^o(\mathbf{Q}) \int_0^\infty du f(u^2+\gamma)[1-f(u^2+\gamma+\hbar\omega_{\mathbf{Q}})] \tag{3.78}$$

Here, τ_f is the relaxation time at the Fermi level,

$$C_g = \frac{|e|\lambda_p g_v (2m^*)^{\frac{1}{2}}}{32\pi^3 \hbar k_B T^2 \rho}, \tag{3.79}$$

$$F(\mathbf{Q}) = \frac{Q|Z_{11}(q_z|^2}{\epsilon^2(\mathbf{Q})} \frac{1-e^{-\hbar\omega_{\mathbf{Q}}/k_BT}}{sinh^2(\hbar\omega_{\mathbf{Q}}/2k_BT)} E_s^2(Q) \tag{3.80}$$

and

$$\lambda^o(\mathbf{Q}) = 1 + p\frac{1}{2}\frac{\hbar\omega_{\mathbf{Q}}}{\varepsilon_f}[1 + \frac{\hbar\omega_{\mathbf{Q}}}{\hbar^2 q^2/2m^*}] \tag{3.81}$$

In equation (3.80), $E_s(Q)$ is the effective deformation coupling function for mode s which appears on the right hand side of equations (3.74) and (3.75).

The factor $\lambda^o(\mathbf{Q})$ is the result of the consideration of an energy dependent relaxation time in the integrand of the phonon drag formula. The valley degeneracy g_v in equation (3.79) is $g_v = 2$ for Si and $g_v = 1$ for the GaAs/AlGaAs heterojunction, and the in-plane effective masses m^* are $0.1905m_e$ and $0.067m_e$ respectively, where m_e is the free electron mass. The temperature dependent dielectric function in equation (3.75) is calculated in the random-phase approximation as described in section 3.3. Finally, the u-integration in equation (3.78) accounts for the spread of electron energies involved in phonon drag with:

$$u^2 = \varepsilon(k) - \gamma \tag{3.82}$$

where

$$\gamma = \frac{(\hbar\omega_{\mathbf{Q}} - \hbar^2 q^2/2m^*)^2}{4(\hbar^2 q^2/2m^*)} \tag{3.83}$$

Neglect of the thermal broadening of the Fermi function would lead to considerably overestimated thermopower values in Si, but to a small effect in GaAs, as it will be seen in the following chapter, where detailed calculations of the electron mobility in both Si-MOSFET and GaAs/AlGaAs heterojunction are discussed.

Chapter 4

Electron transport: calculations

4.1 Introduction

Electron transport in 2D is distinguished from that in 3D by certain special features. For example, the ionized impurities can be classified according to their position relative to the 2DEG. Moreover, an additional scattering mechanism is introduced by the presence of imperfect interfaces.

Electron mobility has extensively been studied both theoretically and experimentally because it reflects these scattering processes. In the temperature range considered here ($T < 7$ K), phonon scattering has been proved unimportant for mobility in both Si-MOSFETs and GaAs/AlGaAs heterojunctions [46, 50, 54, 55, 56, 57] and the mobility is limited by ionized impurities and interface roughness. The peak mobility has often been used to characterize a sample. Improved understanding of the scattering can lead to improvement of the growth technique as well as to the invention of new structures in order to achieve higher mobilities; the modulation doping technique is an example [1].

The thermoelectric properties of electrons in low-dimensional structures have also attracted the interest of researchers. Diffusion thermopower reflects the energy dependence of the relaxation time, and is determined not only by the magnitude of scattering but also by details concerning the distribution and

the type of scatterers. Phonon drag thermopower involves the electron-phonon interaction and is dominant above a temperature of the order of 2 K.

Electron mobility and thermopower have so far been examined independently and from different points of view. In this chapter, detailed calculations of both transport properties are presented in order to obtain a combined knowledge of electron mobility and thermopower, which may help to improve the understanding of the properties of the 2D structures. The need to do this is shown in some special cases where novel phenomena have been observed.

Mobility and diffusion thermopower calculations for Si-MOSFET samples at $T < 2$ K are presented in section 4.2. In section 4.3, electron transport in Si-MOSFETs is discussed for $T > 2$ K. Sections 4.4 and 4.5 respectively deal with electron mobility and thermopower calculations for GaAs/AlGaAs heterojunctions respectively.

4.2 Electron transport in a Si-MOSFET for $T < 2$ K.

The electron mobility and thermopower of two Si-MOSFETs (table 4.1) have been measured by Gallagher et al [58, 59] and they are shown in figure 4.1. The main difference between the two samples is the acceptor concentration

Table 4.1: Data for Si-MOSFET samples (after Oxley)

Device	Sample A	Sample B
Dimensions of chip (mm)	0.38 x 2.9 x 12	0.38 x 1 x 12
Width of gate (mm)	0.5	0.4
Separation of voltage probes (mm)	4.0	1.2
N_s vs V_g (m^{-2})	$(2.67V_g) \times 10^{14}$	$(2.88V_g + 2.87) \times 10^{14}$
V_T	0.0	1.0
Boron doping level ($m^{-3} \times 10^{21}$)	0.015	1.35
Peak mobility at base temperature (m^2/Vs)	1.26	1.53

N_A in the Si, which is two orders of magnitude higher in sample B (N_A =

$1.35 \times 10^{21} m^{-3}$) than in sample A ($N_A = 1.5 \times 10^{19} m^{-3}$). Since the samples were fabricated independently, they are also expected to differ in the ionized impurity concentrations and distributions and in interface quality.

The mobility increases first with N_s, takes a maximum value at N_s of $3 - 7 \times 10^{15} m^{-2}$ and then decreases with increasing N_s (see figure 4.1). The peak mobility is, at $T = 1$ K, 1.26 m^2/Vs for sample A and 1.53 m^2/Vs for sample B. Sample A exhibits higher thermopower magnitudes than sample B. It is notable that in sample B at $T < 1.5$ K and high electron concentrations ($N_s \sim 10^{12} m^{-2}$) positive thermopower values have been measured, whereas in sample A at even higher electron densities and for all temperatures the thermopower remains negative.

The positive thermopower has been attributed to a positive diffusion thermopower which dominates at low temperatures ($T < 2$ K) [58]. Positive thermopower has been observed in other systems [60] and was attributed to second subband occupation. In samples A and B, only the ground subband is thought to be occupied (Gallagher, private communication). As supporting evidence we note that in a Si-MOSFET, where for $N_{depl} = 1.55 \times 10^{15} m^{-3}$ and $N_A = 1.65 \times 10^{21} m^{-2}$ (i.e. similar to the boron doping level in sample B), higher subbands only become occupied at $N_s > 3 \times 10^{16} m^{-2}$ [2]. Furthermore, the subband separation decreases with decreasing N_{depl}, and in sample A the second subband would become occupied well before that in sample B. There has been an attempt to explain the positive thermopower by invoking background impurity scattering [61], and measurements in sample A seem to support this idea. However, the present calculations do not support the theory proposed by Karavolas et al. [61]. In what follows, electron scattering and transport are analyzed in order to evaluate the role of each scattering mechanism in limiting the mobility and explaining the measured transport properties.

4.2.1 Dominant scattering mechanisms.

Two mechanisms are known to contribute to the scattering of electrons in inversion layers in Si at low T: charged impurity and interface roughness scattering.

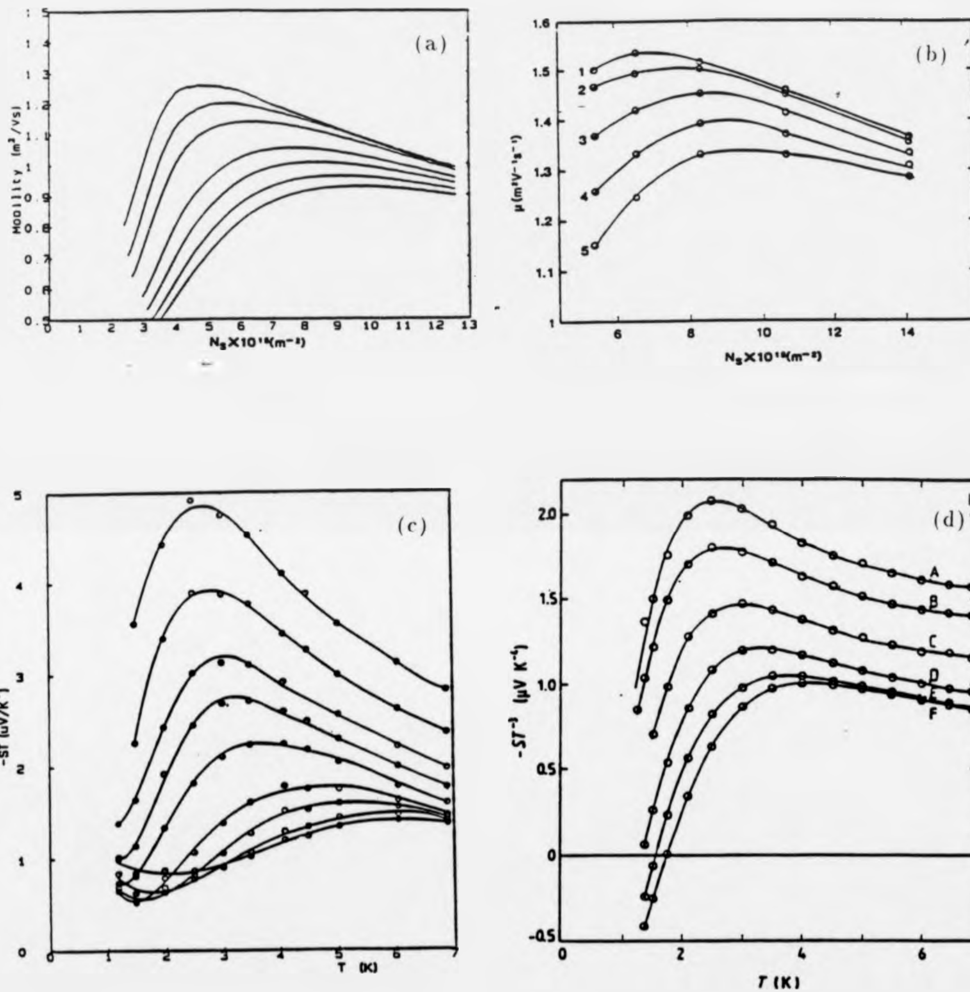

Figure 4.1: Measured mobilities and thermopowers in Si-MOSFETs

Measured mobilities versus areal electron density for sample A (4.1a) at 1, 2, 3, 4, 5, 6, 7 K and for sample B (4.1b) at 1,2,3,4,5 K. Measured thermopower divided by T^3 for sample A (4.1c) for electron densities from uppermost to lower curve 7.08, 8.01, 9.35, 10.7, 13.4, 20, 26.7, 34.7, 42.7 $\times 10^{15} m^{-2}$ and for sample B (4.1d) for electron densities from uppermost to lower curve 4.9, 5.47, 6.57, 8.35, 10.7, 14.1 $\times 10^{15} m^{-2}$. The curves through the experimental points are a guide to the eye.

Scattering associated with Coulomb centers near the plane of the 2DEG can be separated into contributions from the depletion layer, the oxide charge and the interface charge. Due to image forces, sodium ions (probably the main contribution to the interface charge) are attracted towards and (due to the low solubility of sodium in Si) remain close to the interface [57, 62].

In a Si-MOSFET, the electron density can be changed over a wide range by varying the strength of the electric field applied perpendicular to the interface (gate voltage). At low N_s, ionized impurities near or at the interface appear to be important and predict the correct order of magnitude and the right qualitative mobility behaviour in that region. The screening length decreases with increasing N_s and the ionized impurities are screened more effectively, resulting in higher mobilities at higher electron concentrations. Moreover, the important length in scattering is k_f^{-1} and charged centers which contribute to scattering are limited by the condition $|z_i| < k_f^{-1}$, when $< z > < k_f^{-1}$. In a Si-MOSFET this condition is satisfied; for $N_s = 1.07 \times 10^{16} m^{-2}$ ($k_f^{-1} = 55\AA$), and for $N_A = 1.5 \times 10^{19} m^{-3}$ the average position is $< z >= 30\AA$ whereas for $N_A = 1.35 \times 10^{21} m^{-2}$, $< z >= 34\AA$. Many charged centers can contribute at low electron concentrations, but only a small number of centers, especially ones which are located near the interface, contribute to it at high electron concentrations. Since increasing N_s, decreases the number of important Coulomb centers, the mobility increases with increasing N_s when ionized impurity scattering dominates. This dependence also explains the steeper N_s dependence of the mobility limited by a uniform distribution of remote or background impurities, rather than by a fixed concentration of charged centers at the interface. In the latter case, the important charged center concentration does not depend upon N_s, because the impurity location does not change with respect to the electron gas.

Although remote and background Coulomb centers are undoubtedly present, it is common [57] to consider only surface charges, because only the charged centers near the plane of the 2DEG contribute effectively to the total scattering rate of the electrons. Contributions to the scattering by depletion and oxide

charge are assumed to give effectively an increased interface charge.

Interface roughness is proposed as the explanation for the low temperature experimental results at high electron densities. This mechanism is associated with the surface inhomogeneities of the Si-SiO_2 interface. Since the crystal structures and the energy band structures of Si and SiO_2 differ greatly, the interface between them differs from an ideal plane. The scattering on the random potential produced by the interface inhomogeneities can provide a qualitative explanation for the mobility drop; as the surface field increases, carriers are drawn closer to the surface and consequently the effect of the fluctuating potential becomes much stronger. The relaxation time due to this mechanism then dominates over that due to Coulomb scattering. We note that low temperature data for p-type channels show [54] that the mobility at high surface fields only depends on sample preparation and becomes independent of the density of surface ionized impurities, whereas the situation is reversed at low fields.

Before proceeding with the presentation of calculated mobilities, it is interesting to discuss further some of the factors that determine the electron scattering.

4.2.2 More on electron scattering.

The effectiveness of each scattering potential can be measured by the change of the direction of the wave vector. In figure 4.2, the angular distribution of the normalized scattering rate at the Fermi level is shown for interface roughness (IFR) and charged impurity scattering when the charges are in the background (BI) of the electron gas, when they are located on the interface (IF) and when they are on the other side of the interface (RI). It can be seen that interface roughness primarily scatters the electrons at large angles. For Coulombic scattering, the angular distribution is more extended and depends strongly on the position of the charged centers with respect to the electron gas. The electrons are scattered more effectively (i.e. at large angles) the closer the impurities are to the electrons. The full dependence of the scattering on the scattering angle θ and the electron wave vector k is shown in figure 4.3, where the integrands of

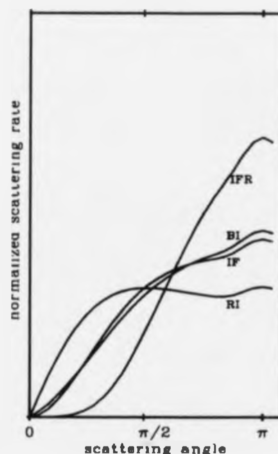

Figure 4.2: Scattering angle distribution for various processes
Normalized scattering rate at the Fermi level versus scattering angle for scattering by interface roughness (IFR), background (BI), interface (IF) and remote (RI) ionized impurities.

equations (3.45) and (3.56) are plotted against k/k_f and θ.

Figures 4.2 and 4.3 indicate that the scattering is small or large angle dominated depending on both the electron energy and position of the impurities with respect to the electron gas. The structure seen in figure 4.3 is caused by screening, which is stronger when the change in the electron wave vector $q = 2ksin(\theta/2)$ is less than $2k_f$ (also see figure 3.1). For $ksin(\theta/2) > k_f$, the reduced screening enhances the scattering rate and dominant scattering angles. If zero temperature screening is considered, the gradual change in the neighborhood of ε_f is replaced by a sharp change at ε_f, as it is shown in figure 4.2e for interface roughness. This is the effect of the sharp corner of the zero temperature polarizability when the change of the electron wave vector due to scattering is equal to $2k_f$ (figure 3.1), and is consequently eliminated when temperature broadening of the screening is allowed for. In a zero temperature treatment of screening, the calculated relaxation times are 'kinked' at ε_f (figure 4.4), and so calculated values of p [61] can not be trusted. Screening is thus important for

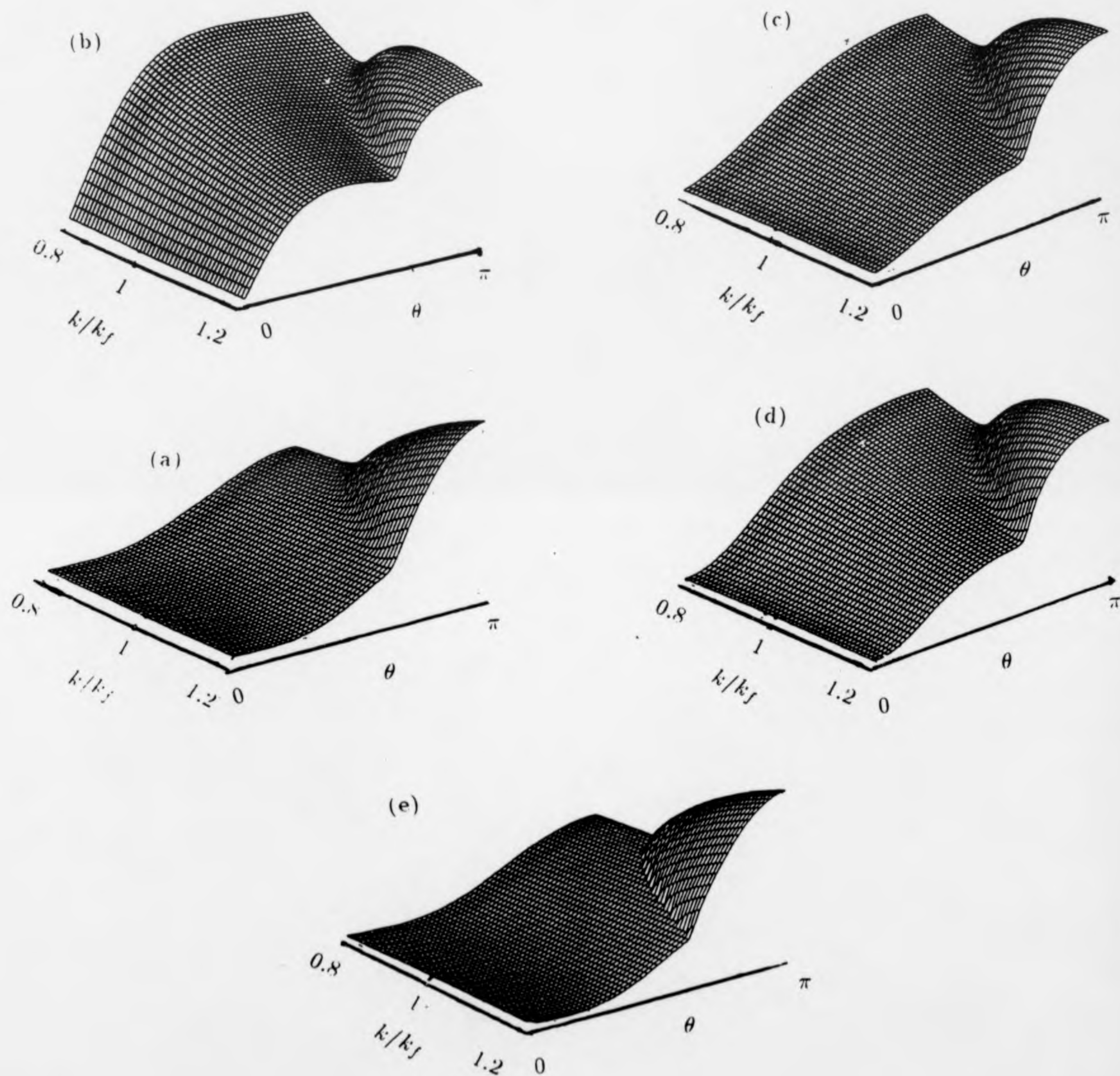

Figure 4.3: Wavevector and scattering angle distributions

Scattering rates versus the scattering angle θ and k/k_f for interface roughness (a),remote (b), background (c) and interface (d) ionized impurities. 4.3e is as in 4.3a but when the temperature broadening of the polarizability is neglected.

the energy dependence of the relaxation time τ around ε_f, and it is consequently crucial for the determination of the diffusion thermopower, as equations (3.65) and (3.66) show.

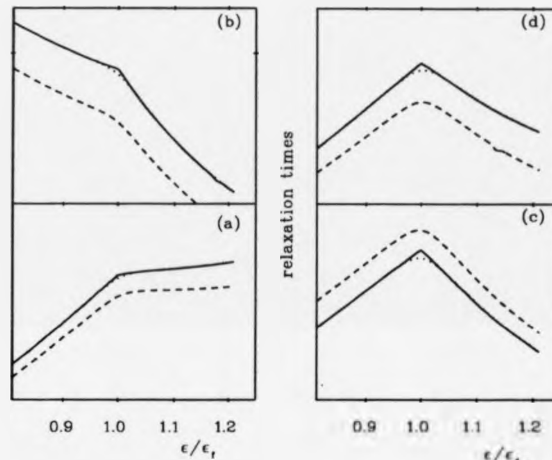

Figure 4.4: The effect of image potential and temperature dependence of screening on electron relaxation times

The electron relaxation times limited by remote impurities (a), interface roughness (b), background (c) and interface impurities (d) are plotted against $\varepsilon/\varepsilon_f$ when image effects are neglected (dashed lines), temperature broadening of screening neglected (solid lines) and when all corrections are included (dotted lines).

For the sake of simplicity, some many body energy terms have been omitted from the electron energy so that an analytical expression can be obtained for the parameter b (equation 1.12). However, it is possible to add the exchange energy and the image term. The former is attractive and contracts the wave function, while the latter is repulsive and expands it. At high densities it is better to omit both terms than to include either alone [2]. For low carrier densities, $N_s + N_{depl} \sim 10^{15}m^{-2}$ (i.e. $N_s \sim 6 \times 10^{15}m^{-2}$ for sample A and $N_s \sim 7 \times 10^{15}m^{-2}$ for sample B) the exchange term is negligible but the image term must be included in equation (1.11) [2]. Figure 4.4 shows that the image

potential reduces the scattering in all cases except for background impurities. This behavior can be interpreted in terms of the expansion of the electron wave function, which means that the mean separation of electrons from the interface increases. This explains the reduced interface roughness scattering and the reduced scattering by ionized impurities in the oxide near or at the interface. On the other hand, the expansion of the wavefunction enhances scattering by background impurities because the effective region of interaction increases. It is found that the image potential changes the relaxation time almost uniformly for all the energies (figure 4.4), so that the derivative of τ at ε_f and consequently the diffusion thermopower are not altered. The mobility is, however, affected, since it is proportional to the magnitude of τ (see equation 3.55).

Usually, the charged acceptors in bulk Si play little role as scatterers except at extremely small electron concentrations. For bulk doping of $10^{22}m^{-3}$, there are only $\sim 10^{14}m^{-2}$ acceptors within 10 nm of the interface in most samples. Background impurity scattering has been found to be negligible even for sample B (the corresponding relaxation time is of the order of 10^2 ps), in contrast to the predictions of references [61, 63]. Gallagher's experiments also indicate that background impurities do not dominate at high N_s, since the measured mobilities of sample B (high N_A) are bigger than those of sample A (low N_A).

Another important difference between our calculations and those presented in [61, 63] is the electron density dependence of the mobility limited by background impurities. We find the same behaviour for background impurities as for the other ionized impurities. Our findings are supported by similar calculations presented in [64]. Furthermore, for background impurity scattering p is found here (see figure 4.7) to be only slightly negative (in [61] $p = -3$), and it is therefore impossible to attribute positive thermopower to background impurity scattering.

Values of p are shown in figure (4.7) for both samples and all the scattering mechanisms. By comparing figures 4.7b and 4.7d, it can be seen that the value of p for each scattering mechanism is only slightly affected by N_A. For interface roughness scattering, p is very sensitive to the parameters Λ and Δ. The sign

of p is determined by the effectiveness of the scattering potential and it is positive (negative) for small (large) angle dominated scattering mechanisms. It has already been mentioned that the further removed from the electrons the impurities are, the more small angle scattering dominates. It is therefore not surprising that p is positive for remote impurities, slightly negative for interface ionized impurities and even more negative for background impurities. Strongly negative values of p are found for interface roughness scattering, in agreement with the observation that short range roughness causes large angle scattering (figure 4.2).

The concentration of Coulomb centers at and near the interface on the oxide side does not affect p very much. It primarily modifies the strength of the process as a proportionality constant. This explains why the calculated values of p for remote impurities and impurities on the interface are almost the same in both samples, irrespective of the different impurity concentrations (figures 4.7 b and d). The cause of any changes in p for the individual scattering processes is the different acceptor concentration of the two samples, since N_A influences the electron distribution as shown in equation (1.12). Nevertheless, all the ionized impurity concentrations are important in determining the value of the total p, since now they determine the weight of each scattering process in the total scattering rate according to equation (3.59). Finally, for interface roughness the strength of scattering depends on the values of both Λ and Δ whereas p depends only on the value of Λ and varies from system to system as Λ does.

4.2.3 Calculated transport coefficients.

The weight of each scattering mechanism in limiting the electron mobility can only be found by trying to fit the experimental data. After a systematic search, it is concluded that the experiments can be satisfactorily explained by ionized impurities at the interface and interface roughness scattering. The variation of the total relaxation time with N_s is shown in figure 4.5.

In the same figure, the relaxation time due to ionized impurities at the

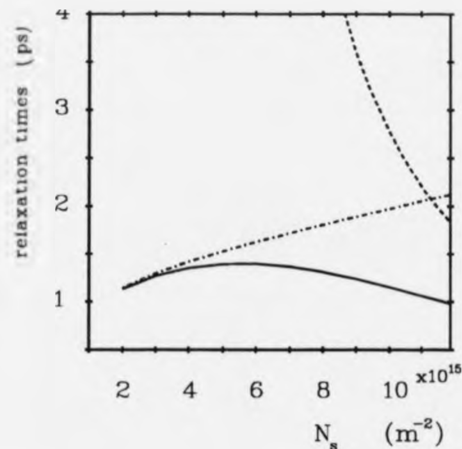

Figure 4.5: Electron density variation of the relaxation times

The electron relaxation times limited by remote impurities (dashed line), interface roughness (broken line) and all the scattering processes (solid line) against the areal electron density.

interface and interface roughness scattering are shown. The former increases with N_s, the latter decreases with N_s. According to equation (3.59) the smaller relaxation time dominates. Therefore, at low N_s ionized impurity scattering dominates and the mobility increases with N_s. At higher N_s, scattering by interface roughness takes over and the mobility decreases with N_s.

Calculated mobilities together with the experimental data are shown in figure 4.6 for both samples. The concentration of interface impurities is chosen $N_{IF} = 7.5 \times 10^{14} m^{-2}$ for sample A and $5.4 \times 10^{14} m^{-2}$ for sample B. The interface roughness parameters are estimated to be $\Lambda = 82A^o$, $\Delta = 6A^o$ for sample A and $\Lambda = 76A^o$, $\Delta = 4A^o$ for sample B.

At low electron concentrations a more elaborated theory is needed. Gold et al. [65] applied a current-relaxation theory to study the crossover from insulating to conducting behaviour in inversion layers. Scattering and screening are treated within a self consistent scheme. The theory shows a stronger decrease in the mobility at low N_s side when multiple scattering is included, than

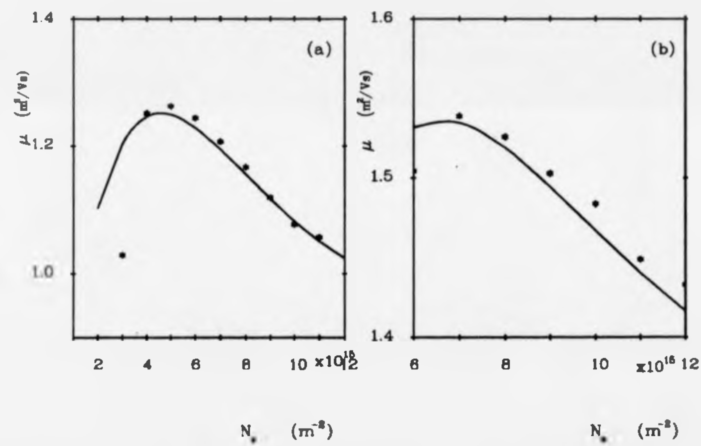

Figure 4.6: Independently fitted electron mobilities

The electron density variation of the calculated electron mobilities (solid curves) are compared with that of the measured at $T = 1$ K for (a) sample A; $N_{IF} = 7.5 \times 10^{14} m^{-2}$, $\Lambda = 82\AA$ and $\Delta = 6\AA$ and (b) sample B; $N_{IF} = 5.4 \times 10^{14} m^{-2}$, $\Lambda = 76\AA$ and $\Delta = 4\AA$.

is apparent from the curve without multiple scattering. However the strong decrease of mobility occurs at much lower electron density than is observed in the experiment. To proceed with that Kruitof et al. [57] used the idea of band tailing. This approach focuses on the 2D density of energy states. As was discussed in chapter 1, this is step-like. However, in a real situation the steps are rounded. When ε_f approaches the subband edge, the small value of the density of states leads to a smaller screening wavevector and therefore to a decrease of mobility. One can show that this effect only influences a narrow range of electron densities and because it has no effect on the mobility when surface roughness scattering dominates, it is neglected in the present calculations.

Although the measured mobilities are very well explained by the above interface impurity concentrations and interface roughness parameters, both sets of parameters give high values of thermopower at low T ($T < 2$ K), where diffusion dominates in a MOSFET. Moreover, no positive thermopower is found for sample B. The problem arises from the positive values of p for the assumed parameters; the observed thermopower magnitudes require negative p. Positive values of p are associated with the assumed long range roughness, characterized by $\Lambda > k_f^{-1}$. Under this condition the screening dominates over the roughness, and as the electron gas becomes more dense the carriers see less roughness; they are less effectively scattered and p is therefore positive. When $\Lambda < k_f^{-1}$, the electrons feel the interface irregularities and as their density increases, they are dragged closer to the interface and they are scattered more effectively, so that p is negative. It can be concluded that the present samples may exhibit short range roughness.

To study the consequences of this idea, the scattering parameters are now modified as follows. The concentration of interface impurities is estimated $N_{IF} = 8 \times 10^{14} m^2$ for sample A and $2 \times 10^{14} m^{-2}$ for sample B. It is noted that these densities are in agreement with [54, 57], where the surface charge is estimated $\sim 10^{14} m^{-2}$. The interface roughness parameters are estimated to be $\Lambda = 35 A^o$, $\Delta = 7 A^o$ for sample A and $\Lambda = 20 A^o$, $\Delta = 9 A^o$ for sample B. The calculated mobilities and thermopowers of the two samples are shown in figures

4.7 and 4.8.

Quantitatively, the results are in a very good agreement with the data, with the exception of the mobility of sample B. Although the assumed height of the roughness (Δ) is relatively high in both samples, it can be considered acceptable for sample A ($\Delta = 7\mathring{A}$), since similar values have been reported elsewhere [65]. The roughness is very sensitive to the conditions of fabrication, and microscopic investigation is the only reliable way to estimate its form and magnitude; the large Δ ($9\mathring{A}$) for sample B would not therefore be an insurmountable problem, if the mobility could be satisfactorily explained. Here, a much steeper decrease of the mobility with N_s is calculated than is measured. It seems that the present isotropic statistical theory of interface roughness is inadequate to describe the magnitude and the correct density dependence of the mobility, assuming an energy dependence of the relaxation time compatible with the observed thermopower values.

Goodnick et al. [66] studied the statistical properties of random fluctuations at the interface boundary using cross-sectional high-resolution transmission electron microscopy (HRTEM). The observed spectral properties of the roughness on normally prepared and intentionally roughened samples appear to be well characterized by an exponential decay in the autocovariance function, rather than the Gaussian approximation. However, they found that the difference in the statistical properties of the interface does not lead to significant changes in the dependence of the mobility on N_s, particularly when $\Lambda < k_f^{-1}$ [67]. The parameters characterizing the roughness are only slightly different when either the Gaussian or the exponential correlation is used. We also note that in this analysis the interface boundary is chosen as the last discernible lattice fringe corresponding to the periodicity of the Si. This procedure is somewhat arbitrary at many points, as an abrupt change from crystalline Si to non-crystalline SiO_2 is not always apparent. The analysis also neglects the contribution to the interface width of intermediate bonding states and the existence of a transition layer between Si and SiO_2. Stern [68] estimates the transition layer width to be of the order of 5 $\mathring{A}$ and suggests that electrons in the lowest

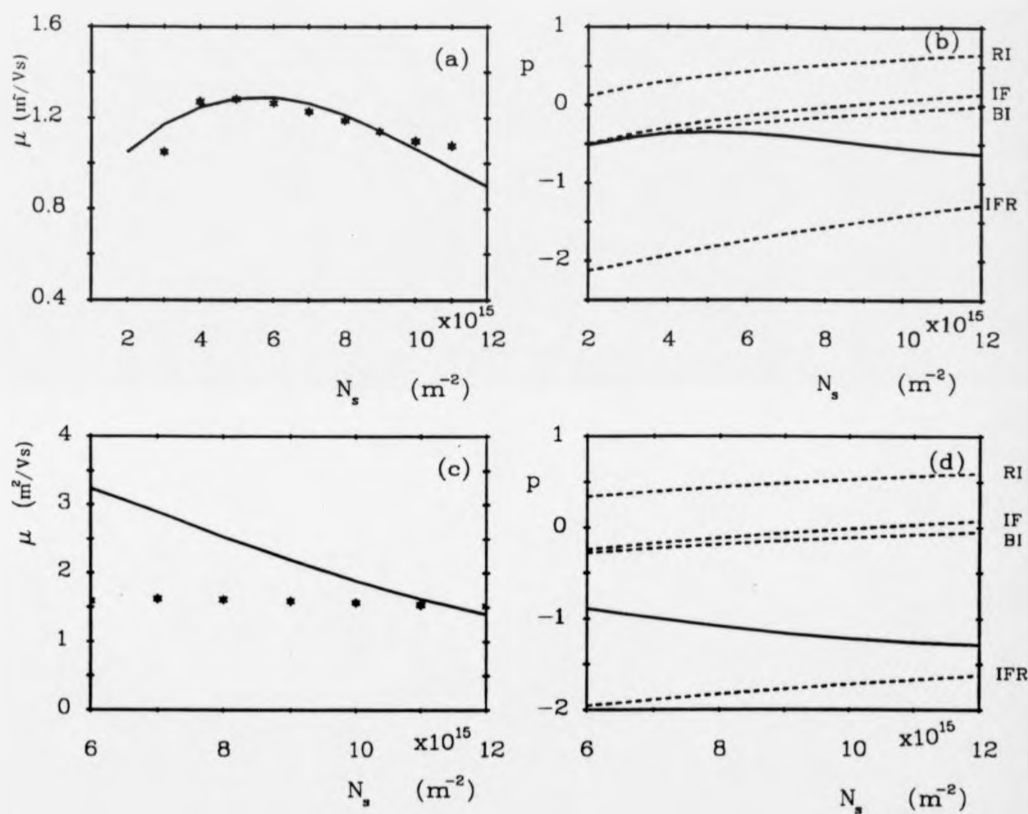

Figure 4.7: Calculated mobilities and values of p

The electron density variation of the calculated electron mobilities (solid curves) are compared with that of the measured at $T = 1$ K for (a) sample A: $N_{IF} = 8 \times 10^{14} m^{-2}$, $\Lambda = 35 \AA$ and $\Delta = 7 \AA$ and (c) sample B: $N_{IF} = 2 \times 10^{14} m^{-2}$, $\Lambda = 20 \AA$ and $\Delta = 7 \AA$. The calculated logarithmic derivative p for all the scattering processes are shown for sample A in (b) and for sample B in (d).

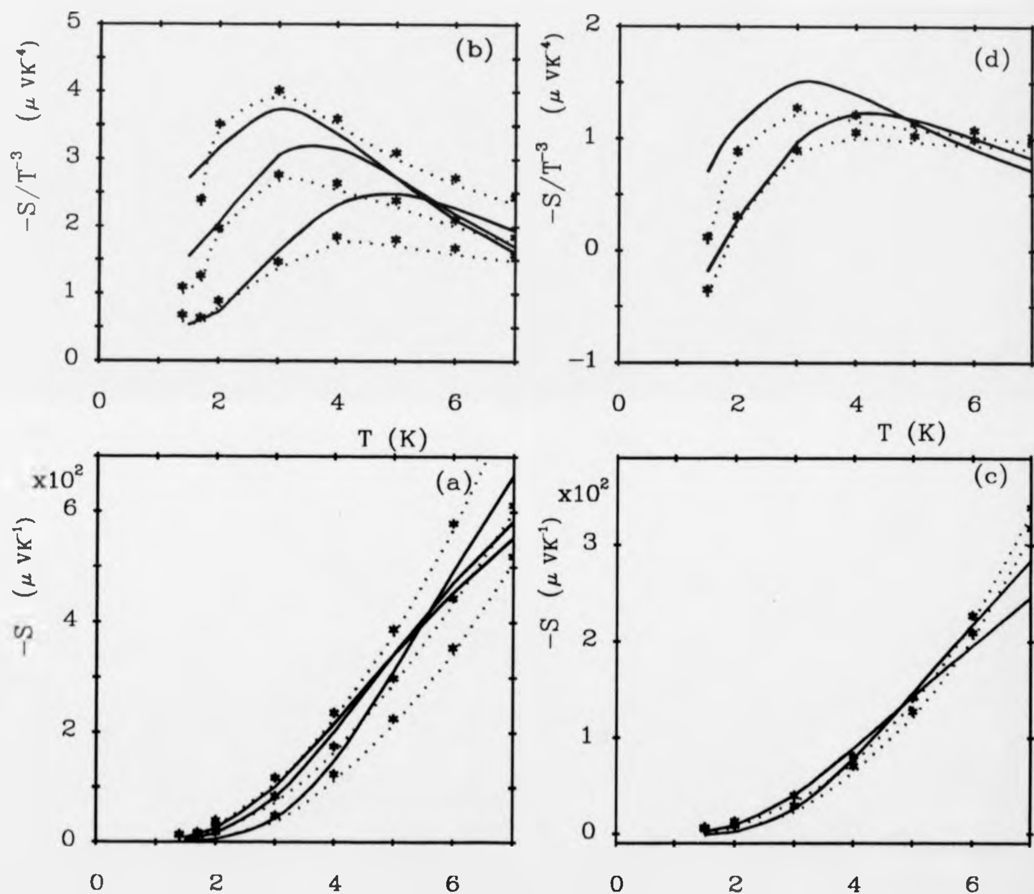

Figure 4.8: Calculated and measured thermopowers

The temperature variations of -S and -S/T^3 are plotted for different electron densities in (a,c) and (b,d) respectively for both samples. The solid lines are the calculated values and the stars the measured values; the curves through the stars are guide to the eye. From the uppermost to the lowest curve the corresponding electron densities are (i) for sample A: 8.01, 10.7, 20 $\times 10^{15} m^{-2}$; figures (a,b) and (ii) for sample B: 8.35, 14.1 $\times 10^{15} m^{-2}$; figures (c,d).

subband for a (001) interface have up to 1 % of their charge within the transition layer at large interface electric fields. He also supposes that scatterers in the transition layer can account for interface scattering which has generally been attributed to surface roughness.

The exact form of the power spectrum of the roughness and its anisotropy is determined by the oxidation process and varies from sample to sample. Only a precise knowledge of the physics involved in oxide growth would permit a more detailed theoretical description. Scanning tunneling microscopy might be able to reveal the importance of anisotropy of the correlation [57]. The details of the surface structure are more important at high N_s and N_A, because in both cases the electrons are close to the interface. In sample A the electron's mean position $< z >\sim 35\AA$, and in sample B $< z >\sim 30\AA$. It appears possible that the carriers in sample B, being closer to the interface than those in sample A, and therefore having a bigger proportion of the wavefunction in the transition layer, are more sensitive to disorder in the neighborhood of the interface.

Finally we note that p, as defined by equation (3.66), is appropriate for the calculation of S_d and it is not at all obvious that it coincides with $dln\tau/dln\varepsilon_f$, as it has sometimes been assumed. In sample B , at high densities, $dln\tau/dln\varepsilon_f \sim -0.2$ and cannot explain the positive values of thermopower.

4.3 Electron transport in a Si-MOSFET for $T > 2$ K.

The discussion in section 4.2 concerned temperatures below 2 K, where diffusion thermopower dominates. We now turn to the temperature range $2 < T < 7$ K. Although S_d is proportional to the electronic specific heat ($C_e \sim T$) in Mott's formula, the total thermopower, i.e. the sum of S_d and S_g, displays a non-linear temperature dependence, because S_g is not linear in temperature. The drag calculations are based on the formalism presented in section 3.5.2. A detailed analysis will be attempted, in order to extract the underlying physics of the problem.

In the 3D case there are simple formulae which provide an insight to the dependence of S_g on T, N_s and the phonon mean free path l_p. In [69] interesting arguments are presented to show how these formulae can be extended to quasi-2D systems, as well as how the full phonon-drag formula proposed by Cantrell and Butcher (CB) [33] can be simplified. By appropriate averaging of the relaxation times, the CB formula can be expressed in the form:

$$S_g \propto -\frac{1}{3}\frac{C_v}{|e|N_s}\frac{l_p}{v_s}\alpha \tag{4.1}$$

where v_s is the average phonon velocity , C_v is the lattice specific heat and α accounts for the electron-phonon interaction. According to equation (4.1), S_g varies as T^3 because of the low temperature dependence of the lattice specific heat. This dependence is modified by the enhancement due to favoured phonon absorption which is incorporated in α. The resulting structure of $-S/T^3$ is illustrated in figure 4.8. To interpret this structure we consider unscreened longitudinal acoustic phonon deformation scattering as being approximately elastic. Then, for strictly 2D electrons, equation (3.78) contains the factor:

$$S_g \propto \int_0^{\infty}\int_0^{2k_f} \frac{P(\mathbf{Q})}{(1-(q/2k_f)^2)^{1/2}}dq dq_z \tag{4.2}$$

with

$$P(\mathbf{Q}) = \frac{q^2Q^2|Z_{11}(q_z)|^2}{sinh^2(\hbar\omega_{\mathbf{Q}}/2k_BT)} \tag{4.3}$$

The integrand of (4.2) contains two factors. The first factor, P(Q), describes the phonon distribution and the second factor describes the electron-phonon scattering. P(Q) depends on T and as the temperature increases its peak (at q_D) is shifted to higher Q's (see figure 4.9). The inverse square root factor describes the enhanced phase space available for scattering when q approaches $2k_f$. At low T, q_D lies far below $2k_f$ and the peak of the scattering factor contributes very little. With increasing T an increase in $-S_g/T^3$ is expected because the integrand in (4.2) is increasingly enhanced as q_D moves towards

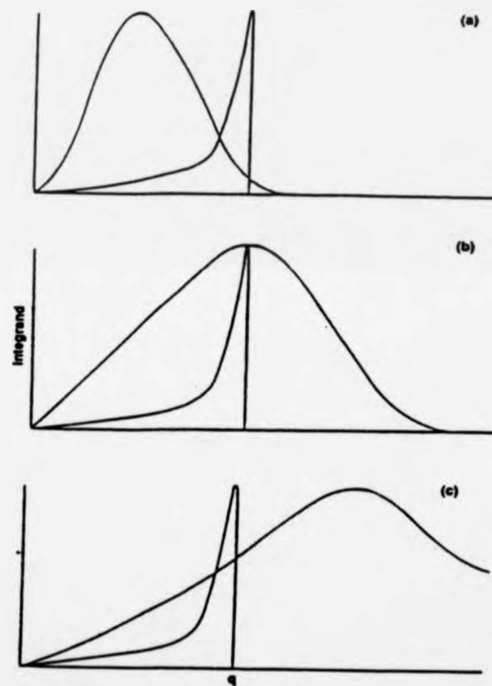

Figure 4.9: Simplified picture for electron-phonon interaction resonance

Plots for the phonon distribution (smooth peak) and the electron-phonon scattering rate (sharp peak) against q for $q_z = 0$. (a) $T < T_p$, temperature at which peak occurs in $-S_g/T^3$; (b) $T = T_p$; (c) $T > T_p$ (after Cantrell and Butcher 1987).

$2k_f$. At a characteristic temperature T_p it becomes a maximum when $q_D \sim 2k_f$. As T moves above T_p, less phonons contribute to the scattering and $-S_g/T^3$ is reduced.

The analytical expression for T_p is [70]:

$$T_p \sim \sqrt{\frac{N_s}{\pi}}\frac{hv_s}{5k_B} \tag{4.4}$$

This expression successfully predicts that T_p moves towards higher temperatures as the electron density increases so as to increase $2k_f$.

T_p is only approximately estimated by (4.4), because the effect of screening, inelasticity and the quasi-2D character of electrons is, in most cases, not negligible. For instance, thermal broadening and inelasticity should explain the smooth structure at high N_s. Here, T_p is higher and both the scattering rate and phonon distribution are broadened. Moreover, the occurrence of the peak is due to the crossing of the maximum of the electron-phonon interaction and the maxima in the thermal distributions of both longitudinal and transverse phonons. The two phonon modes have different velocities and peak at different temperatures, which makes the experimental peak quite broad.

The simple proportionality of S_g and l_p predicted by the simplified models, is also found in equation (3.78). It has been verified by Fletcher [71]. The experiment involves polishing the rear surface of the GaAs substrate on which the heterojunction was grown in order to increase the phonon mean free path. This results in an increase of the thermopower by about a factor of 2, even though the electrical resistivities were unaffected. Measurements of the thermal conductivity K are used in conjunction with the kinetic formula [37] which relates the thermal conductivity K to the phonon mean free path at low T,

$$K = \frac{1}{3}C_v v_s l_p \tag{4.5}$$

where v_s is the average phonon velocity and C_v is the lattice specific heat. Since $C_v \propto T^3$, deviations of K from a T^3 dependence should be attributed to the

temperature dependence of l_p. At very low T, phonons are scattered by the sample boundaries and l_p is independent of T. Additional scattering becomes important at higher T and causes l_p to decrease with T. In the temperature range considered here, the additional scatterers can be point defects intrinsic to the material or extrinsic (boron) impurities. The calculated values of l_p obtained by the measured thermal conductivities and equation (4.5) are shown in figure (4.10) for both samples [59]. In sample A, the boron concentration is too low to affect l_p. In sample B, the contribution of boron to phonon scattering results in a sharper decrease of l_p at $T \sim 2$ K, before point defect scattering starts dominating.

Gallagher et al provide plots of S^{-1} against N_s for a range of T [59]. The N_s^{-1} dependence of S_g predicted by simple models is supported by the experimental data, except at the highest electron densities. The curves intercept the N_s-axis at $N_{MIT} = 1.2 \times 10^{15} m^{-2}$ for sample A and $N_{MIT} = 1.75 \times 10^{15} m^{-2}$ for sample B. This point corresponds to the transition value between strongly and weakly localized electron states [72, 73]. If the Coulomb centers near the interface are positively charged, they attract electrons and form bound states whose behaviour depends strongly on the amount of screening by inversion layer electrons. In Si inversion layers the bound states in the absence of screening are deep enough to trap the first electrons which enter the inversion layer at low T. As the gate voltage is increased and more electrons are added, some will enter the electric subband and will contribute to screening thus weakening the attractive potential. At sufficient high N_s the screening will reach its full value and the energy levels will be so shallow that the orbits of inversion layer electrons bound to adjacent Coulomb centers overlap. Under these conditions the bound states merge with the bottom of the lowest electric subband and effectively disappear [44]. Above N_{MIT}, conduction by free electrons is considered to occur. Since phonons are assumed to interact with free electrons, the appropriate electron concentration in the calculation of S_g, is $N_{sfree} = N_s - N_{MIT}$, if delocalization is neglected. This correction causes an enhancement of $-S_g$, because the corresponding N_s is reduced and there is also a shift of the posi-

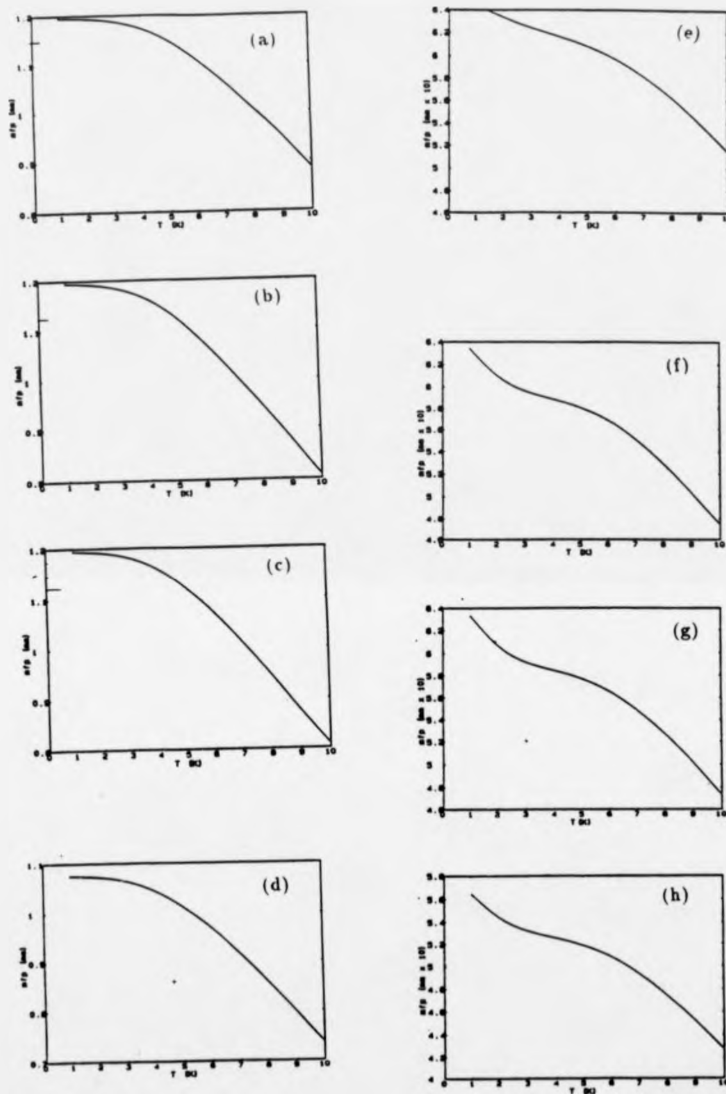

Figure 4.10: Temperature dependence of phonon mean free paths

Temperature variation of the phonon mean free paths for sample A (a-d) and sample B (e-h). (a),(e) longitudinal; (b),(c),(f),(g) transverse; (d),(h) calculated from the thermal conductivity assuming $C_v \propto T^3$.

tions of the peak in $-S_g/T^3$ to lower T. The calculated peaks now lie very close to the measured ones. In figure 4.11 the results including this correction are compared with those obtained neglecting it.

Electron screening reduces the effectiveness of the momentum transfer from phonons to electrons. An extensive quantitative analysis is presented by Smith [35] and it is shown that the calculated magnitudes of S_g are lowered by up to a factor of 20 by screening so that its inclusion in the theory makes possible a quantitative comparison with experiment. The small effect of a T-dependent screening is presented in figure 4.12a. Thermal broadening of the electron distribution function diminishes the screening at $q \leq 2k_f$ and enhances $|S_g|$. At electron concentrations greater than $10^{16}m^{-2}$, the calculations seem to overestimate $|S_g|$. One reason for that might be the single subband screening approximation (SSA) which fails at high N_s. The subband separation decreases with decreasing N_A and it seems possible that screening is underestimated by the SSA.

Calculations in which the temperature dependence of the screening, image potential corrections and the energy dependence of the electron relaxation time are omitted (see figure 4.12), show that these have only a small effect on S_g. What does become important as T approaches 7 K is the thermal tail on the Fermi function. The present calculations allow for non-degeneracy of the electron energy by properly dealing with the u-integration. At $T = 7$ K, $|S_g|$ is reduced by between 30 and 40 % for N_s between 3.5 and $12.7 \times 10^{15}m^{-2}$. At $T = 3$ K, the corresponding reductions are between 14 and 50 % [36]. Neglecting the non-degeneracy effect would overestimate the thermopower.

4.4 Electron mobility in a GaAs/AlGaAs heterojunction.

It is well known that high low-temperature mobilities can be achieved by the modulation doping technique in a GaAs/AlGaAs heterojunction. This is due to the separation between the carriers and the charged scatterers. The undoped

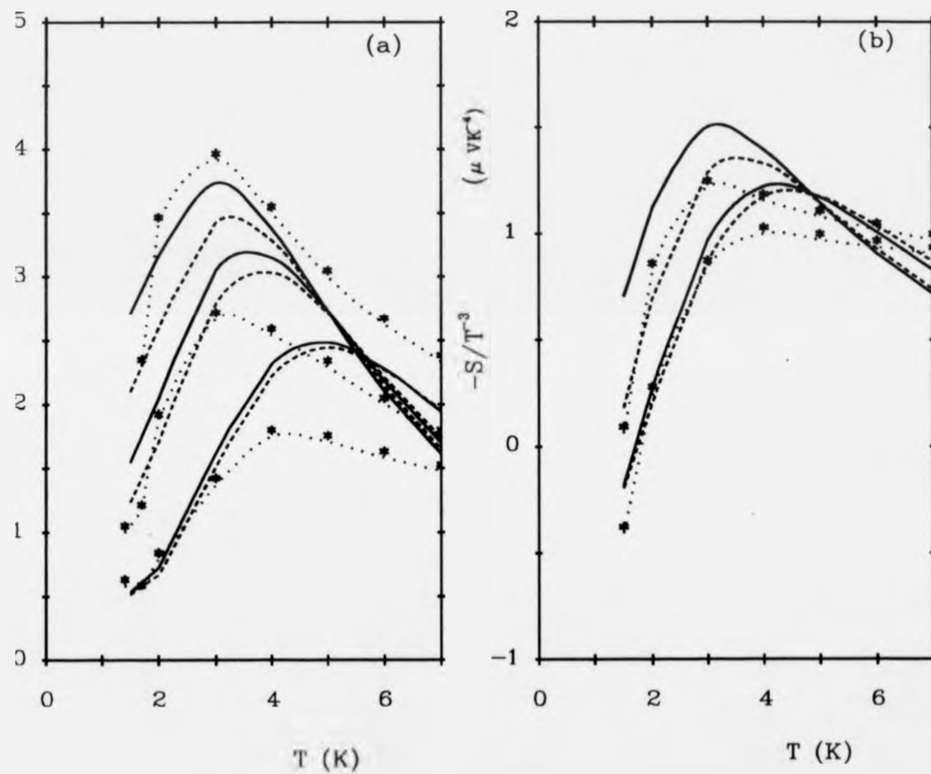

Figure 4.11: Effect of N_{free} in S_g calculations

As in figures 4.8 b and d with the additional broken curves showing the calculated values when the metal insulator transition in N_s is neglected.

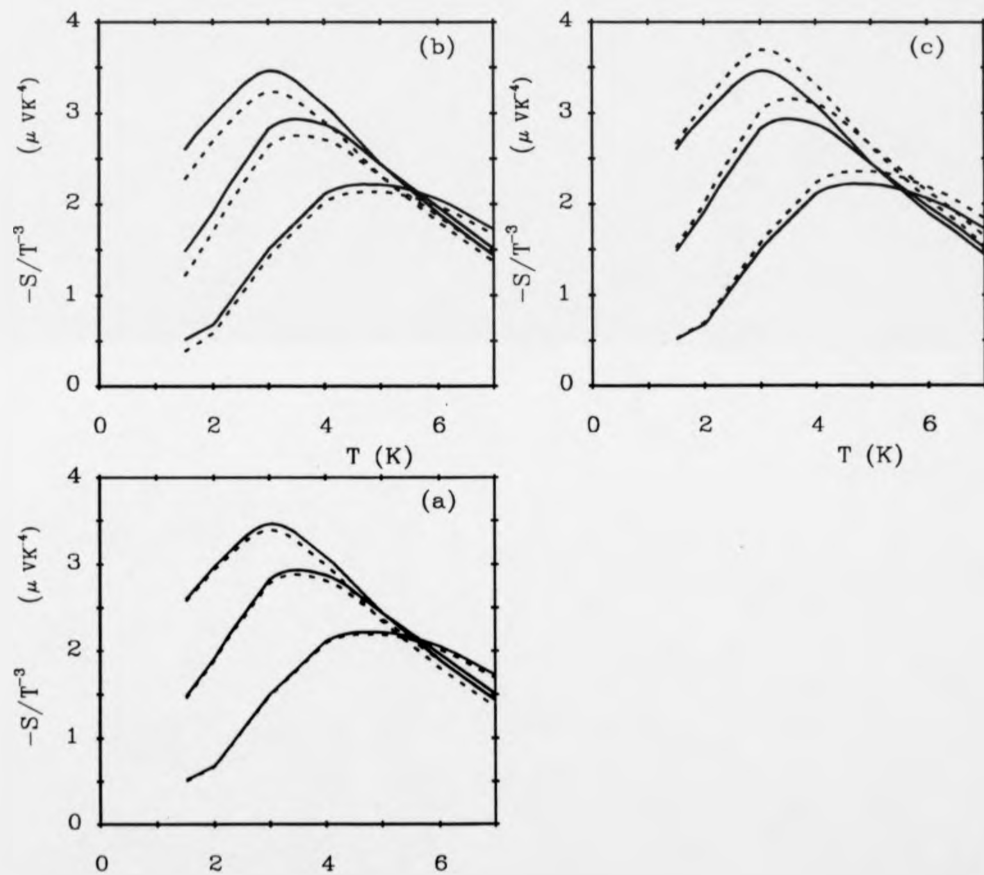

Figure 4.12: Effect of temperature dependence of screening, of image potential and energy broadening of the relaxation time

The calculated thermopowers as in 4.8 b (solid lines) with the broken curves being the corresponding calculated values when the following are neglected: (a) temperature broadening of screening, (b) image effect corrections and (c) energy broadening of the relaxation time.

layer in the alloy region is called the spacer layer and the wider it is, the more the scattering of the inversion layer electrons is reduced. The electrons in the inversion layer in the GaAs come from the ionization of the donors in the AlGaAs, and therefore the electron concentration increases with the concentration of the ionized donors. Moreover, this introduces an upper limit for the electron concentration under equilibrium conditions and further increase is only possible by illumination. In thermodynamic equilibrium (see equation (1.4)), the electron concentration is reduced as the width of the spacer layer increases. This puts a practical limit on the enhancement of the mobility that can be achieved using modulation doping.

One of Fletcher's samples has been chosen for the analysis [71, 74]. A single heterojunction was grown on a pure GaAs semi-insulating substrate and consists of 1.5 μm of p-GaAs ($\sim 10^{15} cm^{-3}$), a 110 $\AA$ spacer of undoped $Ga_{0.68}Al_{0.32}As$, a 200 $\AA$ layer of Si-doped ($3 \times 10^{18} cm^{-3}$) $Ga_{0.68}Al_{0.32}As$ and a 140 $\AA$ GaAs cap layer. Before illumination, the system (sample A1) is in thermodynamic equilibrium, and the charge state of a donor is dictated by the position of the donor level relative to a common chemical potential. The electron density is changed by illuminating the sample until saturation (sample A4). Red radiation is absorbed through the production of electron-hole pairs in the GaAs, either in the cap layer or in the layer forming the junction. In the latter case the pair is separated by the junction electric field with the electron going to the 2DEG and the hole neutralizing a negatively ionized acceptor in the GaAs depletion layer. After the acceptor depletion layer has been neutralized, a further production of electron-hole pairs by the red light is followed by recombination. The continued increase of the 2DEG density can be explained in terms of DX-center (deep-donor) ionization [75]. Here it is assumed that N_{depl}, estimated initially equal to $3.1 \times 10^{15} m^{-2}$ for $N_A = 4.5 \times 10^{21} m^{-3}$, decreases by the same amount as the electron density is increased in the illuminated samples and becomes almost zero in sample A4, so that the increase of the electron density is explained throughout by electron-hole ionization. In a GaAs/AlGaAs heterojunction with $N_{depl} = 5 \times 10^{14} m^{-2}$ a second subband becomes occupied when the electron

density exceeds $N_s = 7.3 \times 10^{15} m^{-2}$ [76]. Since the subband separation depends on N_{depl} and increases with it, for $N_{depl} \sim 10^{15} m^{-2}$ and $N_s = 10^{15} - 10^{16} m^{-2}$ only the ground subband is occupied.

The calculated mobilities, assuming surface roughness with parameters $\Lambda = 45\mathring{A}$, $\Delta = 4\mathring{A}$, are in very good agreement with the experiment as is shown in table 4.2. The ionized remote donor concentration is not influenced by the red

Table 4.2: Mobilities for Fletcher's GaAs samples

N_s $\times 10^{15}(m^{-2})$	$\mu^{measured}$ (m^2/Vs) $T = 4.2$ K	$\mu^{calculated}$ (m^2/Vs) $T = 4.2$ K
2.21	4.20	4.90
2.82	6.40	6.25
3.9	9.30	9.04
5.95	19.30	19.38

illumination and is determined by the thermodynamic equilibrium condition to be $N_{RIN} = 3.6 \times 10^{23} m^{-3}$. In figure 4.13a the calculated mobilities limited by the charges in the AlGaAs are shown. It can be seen that when $N_s << N_{depl}$, the mobility increases because ionization of some donors increases N_s which reduces the strength of the scattering from each impurity as well as the number of impurities effective in scattering. When $N_s > N_{depl}$, the concentration of ionized donors increases much faster (figure 4.13b) and the mobility starts to decrease with N_s. In figure 4.13a the change of μ with the width of the spacer is also shown and the effectiveness of the modulation doping is demonstrated.

The total mobility, under thermodynamic conditions, exhibits the same behaviour with N_s as in Si, as can be seen in figure 4.13c. Here, the electron densities are small because the equilibrium condition demands that N_s be below $\sim 6 \times 10^{15} m^{-2}$ for the given level of Si donor doping. At very low N_s, background and remote impurities are responsible for the increase of the mobility with N_s. At higher N_s, interface roughness and the high increase of the effective doping cause the mobility to decrease. The values of p for the different

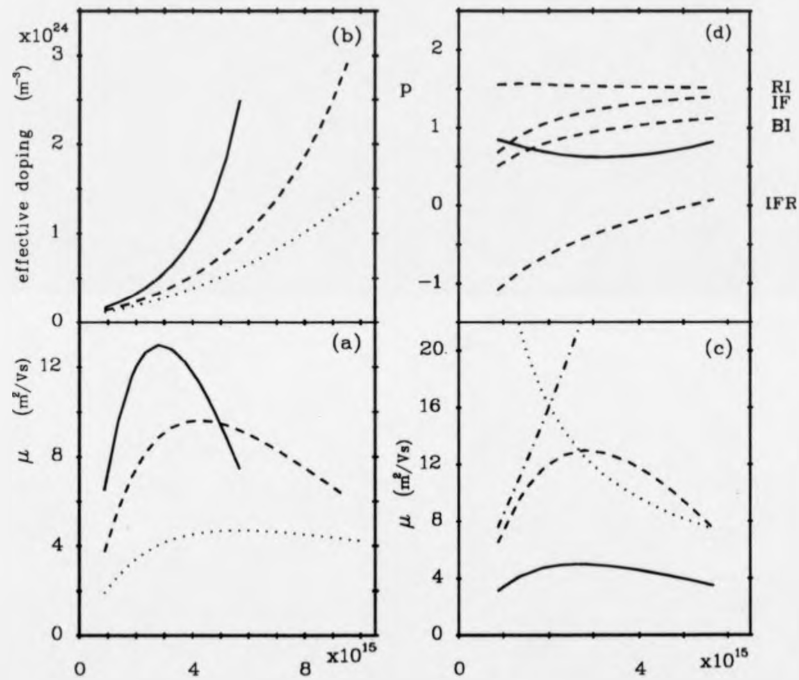

Figure 4.13: Electron mobilities in GaAs/AlGaAs heterojunctions

(a) Mobility limited by remote ionized impurities versus electron density for three values of the space layer width d; solid line for $d = 110\mathring{A}$, broken line for $d = 50\mathring{A}$ and dotted line for $d = 0A$.(b) Effective doping (i.e. ionized remote impurities) versus electron density for space layer widths as in (a). (c) Mobility limited by remote impurities (broken line), background impurities (dashed line), interface roughness (dotted line) and by all the scattering processes (solid line) for $d = 110\mathring{A}$. (d) Logarithmic derivative of τ, p, versus electron density for different scattering processes.

positions of the ionized impurities and for interface roughness, are shown in figure 4.13d. For remote impurities $p \sim 1.5$, and the similarity with the bulk value suggests that the effect of screening is small. For interface roughness, p has values below -1 for very low N_s, increases with N_s and becomes positive at the highest values of electron density. With increasing N_s, k_f^{-1} decreases approaching Λ and at $N_s = 5 \times 10^{15} m^{-2}$, where p changes sign, $(k_f)^{-1}$ becomes approximately equal to Λ .

In the heterojunction the finite barrier height (300 meV) allows a small penetration of the electrons into the alloy. The theoretical limit for the mobility from alloy disorder scattering is of the order of $10^3 m^2/Vs$ [77]. This is 2-3 orders of magnitude larger than comparable predictions due to other scattering mechanisms for heterojunction layers with comparable 2DEG densities. Since the mobility of the heterojunctions used in this work have mobilities closer to 1-10 m^2/Vs, we may safely assume that alloy disorder scattering is not important.

4.5 Thermopower in a GaAs/AlGaAs heterojunction

In GaAs the electrons interact with the phonons via deformation potential and piezoelectric scattering. The phonon drag thermopower results given in figure 4.14 show that the electron-phonon coupling via deformation potential dominates for most temperatures and piezoelectric coupling is only dominant when $T < 2$ K. Electron-phonon interaction becomes weaker as the electron density increases. The coupling is predominantly due to longitudinal phonons and the sharper peak in $-S/T^3$ shown in figure 4.15b is thereby justified. Extension of the experiments to lower temperatures is needed to find the true location of the peaks in these samples.

The phonon mean free path l_p can be estimated from the measured thermal conductivity. This is only available for one of the samples but is assumed approximately the same for all the samples. The thermal conductivity shows a T-dependence deviating from a T^3 dependence, and this is attributed to the

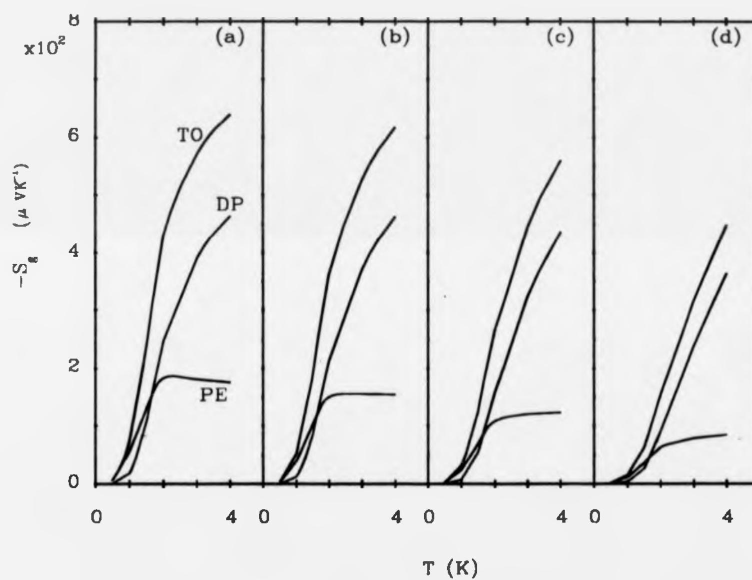

Figure 4.14: Piezoelectric scattering and deformation potential in heterojunctions

Calculated -S_g versus temperature for piezoelectric potential (PE), deformation potential (DE) and total (TO) for N_s = 2.21, 2.82, 3.9, 5.95 $\times 10^{15} m^{-2}$ in (a),(b),(c),(d) respectively.

temperature dependence of l_p. The values used in the calculations are given in table 4.3.

Table 4.3: Estimated phonon mean free path values

T (K)	L (mm)
0.5	1.40
1.0	1.40
2.0	1.30
3.0	0.90
4.0	0.75

The calculated thermopower values are in very good agreement with the measured ones as it can be seen in figure 4.15. In the GaAs/AlGaAs heterojunctions investigated here the temperature dependence of the screening and the energy dependence of the relaxation time have negligible effects. Moreover, because ε_f is so large the effects of the thermal spread of the Fermi function is less significant than was the case for the Si-MOSFETs studied in section 4.3.

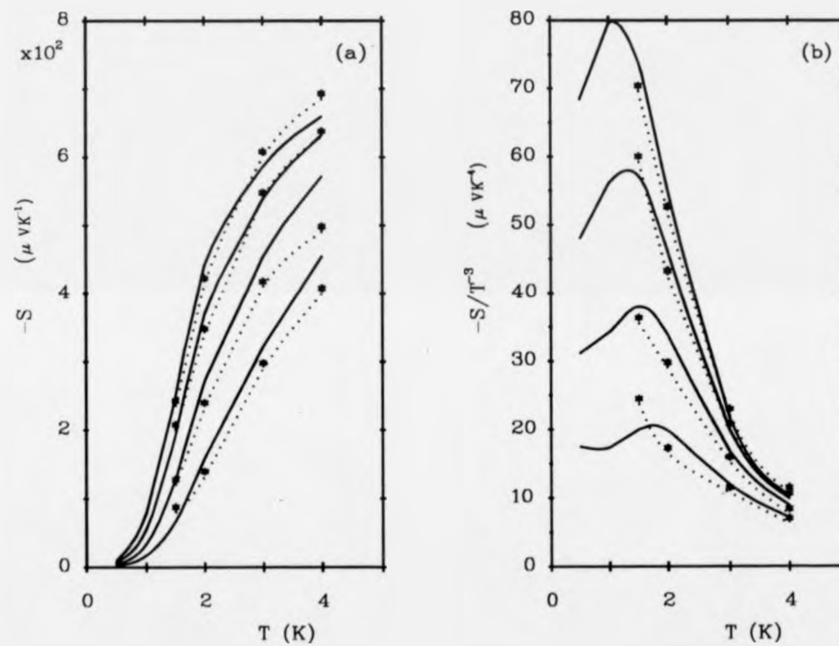

Figure 4.15: Calculated and measured thermopowers for GaAs/AlGaAs heterojunctions

The calculated thermopowers (solid lines) are compared with the measured (stars); the curves correspond to the four electron densities with the upper curve being for the lower N_s and the lowest for the bigger N_s.

Chapter 5

Semiclassical magnetothermopower of a two-dimensional electron gas

5.1 Introduction

The physical effect of a perpendicular magnetic field on the thermoelectric transport properties of a two-dimensional electron gas (2DEG) at low temperatures depends upon the strength of the applied field. Weak localization effects are important below a cut-off field $B_{wl} \sim (4\mu k_f l)^{-1}$, where μ is the mobility, k_f is the Fermi wavevector and l is the electron mean free path [78]. Recent experiments on highly disordered Si on Sapphire MOSFETs ($\mu \sim 500$ $cm^2V^{-1}s^{-1}$, $k_f l \sim 3$) have clearly demonstrated the importance of weak localization effects up to fields ~ 1 T (in these samples $B_{wl} \sim 1.5$ T) [79]. Of course, in higher mobility samples localization effects are much less important and B_{wl} is correspondingly a lot smaller. Much attention has also been given to the behaviour observed in the Landau quantization regime [80, 70, 81], which may be defined as occurring for fields $B > \mu^{-1}\tau_t/\tau_s$, where τ_t is the transport relaxation time and τ_s is the single particle (state) relaxation time [82]. What has been largely ignored, however, both experimentally and theoretically, is the

intermediate regime which lies between the weak localization regime and the Landau quantization regime, in which the transport behaviour is dominated by scattering processes which can be treated semiclassically. For a typical Si MOSFET one might have $\mu \sim 1 m^2 V^{-1} s^{-1}$, $k_f l \sim 10$ and $\tau_t/\tau_s \sim 1$ (since short range potential fluctuations dominate the scattering), in which case this intermediate regime extends from $\sim$ 25 mT to $\sim$ 1 T. In modulation doped GaAs/AlGaAs heterojunctions one might have $\mu \sim 30\ m^2 V^{-1} s^{-1}$, $k_f l \sim 100$ and $\tau_t/\tau_s \sim 10$ (since long range potential fluctuations dominate the scattering), whereupon the intermediate regime extends from $\sim$ 0.083 mT to $\sim$ 300 mT. In this chapter, a Boltzmann equation approach is used to calculate the relevant magnetothermopower tensor of an isotropic 2DEG in this semiclassical intermediate regime. Detailed consideration is given not only to the diffusion thermopower, but also to the less well understood contribution arising from phonon-drag. A number of important observations are made which should be directly amenable to experimental verification.

The chapter is set out as follows. The Boltzmann equation and its formal solutions are given in the following section. In section 5.3 these solutions are used to derive the thermopower tensor. Detailed results are presented in section 5.4 for typical 'higher mobility' samples such as those discussed above.

5.2 The Boltzmann equation.

In response to an in-plane electromotive force $\mathbf{E}$, an in-plane temperature gradient ∇T and a perpendicular magnetic field $\mathbf{B}$, the linearized Boltzmann equation for the electrons can be written:

$$-\frac{f^1}{\tau(\varepsilon)} - \mathbf{v}\cdot\nabla_{\mathbf{r}} f^o - \frac{e}{\hbar}\mathbf{E}\cdot\nabla_{\mathbf{k}} f^o - \frac{e}{\hbar}(\mathbf{v}\times\mathbf{B})\cdot\nabla_{\mathbf{k}} f^1_{\mathbf{k}} + U(\mathbf{k}) = 0 \qquad (5.1)$$

where the functions and parameters are as described in Chapter 3 in connection with equations (3.15) to (3.21). In Appendix B, it is shown that equation (3.22) also holds in the presence of a magnetic field B. Now, the diffusion and drag

contributions to f, are respectively given by the following equations:

$$f_d^1(\mathbf{k}) = -\frac{df^o}{d\varepsilon}\frac{\mathbf{v}\cdot\mathbf{A} - \omega\tau_f(\mathbf{v}\times\mathbf{A})_z}{1+\omega^2\tau_f^2} \tag{5.2}$$

and

$$f_g^1(\mathbf{k}) = \int_0^{2\pi}\frac{d\theta^*}{\omega}G(\theta,\theta^*)U(k,\theta^*) \tag{5.3}$$

with

$$\mathbf{A} = \tau(\varepsilon)[e\mathbf{E} - (\varepsilon - \varepsilon_f)\frac{\nabla_\mathbf{r}T}{T}] \tag{5.4}$$

Here, ω is the cyclotron frequency, τ_f is the (scattering) relaxation time at the Fermi level and $G(\theta,\theta^*)$ is the Green function defined in Appendix B.

5.3 Calculation of the thermopower and the Nernst-Ettinghausen coefficient.

The thermoelectric tensor obtained from the two processes (electron diffusion and phonon drag), according to equations (3.1), (3.9) is described below.

5.3.1 Diffusion.

The transport coefficients are calculated in Appendix C for a degenerate electron gas. It is shown that:

$$\sigma_{xx} = \sigma_{yy} = \frac{\sigma_o}{1+\omega^2\tau_f^2} \equiv \sigma_B \tag{5.5}$$

and

$$\sigma_{xy} = -\sigma_{yx} = -(\omega\tau_f)\sigma_{xx} \tag{5.6}$$

where

$$\sigma_o = \frac{e^2}{m^*}\tau_f N_s \tag{5.7}$$

is the zero magnetic field conductivity, m^* is the effective mass and N_s is the areal density of electrons.

These equations are the well known outcome of the Drude model of the electrical conductivity. It is also shown in Appendix C that the two independent elements of L reduce to:

$$L_{xx} = L_{yy} = \frac{\pi^2 k_B}{3|e|} k_B T \frac{d\sigma_B}{d\varepsilon}|_{\varepsilon_f} \tag{5.8}$$

and

$$L_{yx} = -L_{xy} = \frac{\pi^2 B}{3m^*} k_B^2 T \frac{d(\tau\sigma_B)}{d\varepsilon}|_{\varepsilon_f} \tag{5.9}$$

The thermopower may be expressed in terms of L and σ [31]:

$$S_{xx} = -\frac{\sigma_{xx} L_{xx} - \sigma_{xy} L_{yx}}{\sigma_{xx}^2 + \sigma_{xy}^2} \tag{5.10}$$

$$S_{xy} = \frac{\sigma_{xx} L_{yx} + \sigma_{xy} L_{xx}}{\sigma_{xx}^2 + \sigma_{xy}^2} \tag{5.11}$$

We easily find from equations (5.5)-(5.11) that

$$S_{xx}^d = -C_d(1 + \frac{p}{1 + \omega^2 \tau_f^2}), \tag{5.12}$$

and

$$S_{xy}^d = pC_d \frac{\omega\tau_f}{1 + \omega^2 \tau_f^2} \tag{5.13}$$

with

$$C_d = \frac{\pi^2 k_B}{3|e|} \frac{k_B T}{\varepsilon_f} \tag{5.14}$$

where the energy dependence of τ is again expressed through the quantity p: $p = \varepsilon_f(d\ln\tau/d\varepsilon)|_{\varepsilon_f}$.

The equations for S^d show that the magnetic field dependence of the thermoelectric power tensor is proportional to p. We see that, for a strongly degenerate, isotropic electron gas with $p = 0$, the changes in L in a magnetic field result in zero magnetothermopower $\Delta S_{xx} \equiv [S_{xx}(B) - S_{xx}^0]$ and Nernst-Ettinghausen coefficent S_{xy}.

5.3.2 Phonon drag.

The contribution to the current due to phonon drag can be obtained by combining equations (3.9),(3.18) and (5.3):

$$J^{g}_{2D} = -\frac{2|e|}{k_B T^2 A}\sum_{\mathbf{k}} \mathbf{v} \int_0^{2\pi} \frac{d\theta^*}{\omega} G(\theta,\theta^*) \sum_{\mathbf{k}',\mathbf{Q}} \tau_p(Q)\hbar\omega_{\mathbf{Q}}(\Gamma_{\mathbf{k}'\mathbf{k}^*} - \Gamma_{\mathbf{k}^*\mathbf{k}'})\mathbf{v_P}\cdot\nabla_{\mathbf{r}}T \tag{5.15}$$

where $\mathbf{k}^* = (k,\theta^*)$ and $\mathbf{v_P}$ denotes the phonon velocity.

The components of L are therefore given by:

$$L_{ij} = -\frac{2|e|}{k_B T^2 A}\sum_{\mathbf{k}} v_i \int_0^{2\pi} \frac{d\theta^*}{\omega} G(\theta,\theta^*) \sum_{\mathbf{k}',\mathbf{Q}} \tau_p(Q)\hbar\omega_{\mathbf{Q}}(\Gamma_{\mathbf{k}'\mathbf{k}^*} - \Gamma_{\mathbf{k}^*\mathbf{k}'})v_{pj}. \tag{5.16}$$

We assume that, since we are restricting ourselves to the regime where Landau quantization is unimportant, the electron rates themselves are not affected by the field, in which case $\Gamma_{\mathbf{kk}'}$ is independent of magnetic field. The application of a magnetic field perpendicular to the electron gas does not affect the uniformity of the electron-phonon interaction in the x-y plane. For a given electron energy this interaction depends only on the angle between the phonon and electron wave vectors. This fact simplifies the analytical expressions obtained for L. There are two independent coefficients given by:

$$L_{xx} = L_{yy} = -C_g \int\int dq dq_z F(\mathbf{Q})[(\frac{2m^*}{\hbar}\omega_{\mathbf{Q}} - q^2)I_{00} - (\frac{2m^*}{\hbar}\omega_{\mathbf{Q}} + q^2)I_{01}] \tag{5.17}$$

and

$$L_{yx} = -L_{xy} = -C_g \int\int dq dq_z F(\mathbf{Q})[(\frac{2m^*}{\hbar}\omega_{\mathbf{Q}} - q^2)I_{10} - (\frac{2m^*}{\hbar}\omega_{\mathbf{Q}} + q^2)I_{11}] \tag{5.18}$$

with C_g is given in equation (3.79).

$$I_{nm} = \int_0^{\infty} du O_n(u^2 + \gamma + m\hbar\omega_{\mathbf{Q}}) f(u^2+\gamma)[1 - f(u^2 + \gamma + \hbar\omega_{\mathbf{Q}})], \tag{5.19}$$

Here:

$$O_n = \frac{\omega^n \tau^{n+1}}{1 + \omega^2 \tau^2} \tag{5.20}$$

where u and γ are given by equations (3.82) and (3.83.

The occupancy factor $f(u^2 + \gamma)[1 - f(u^2 + \gamma + \hbar\omega_{\mathbf{Q}})]$ in equation (5.19) is, for $k_B T << \varepsilon_f$, non-zero only in a restricted region around the Fermi level. Moreover the relaxation time does not change rapidly near ε_f. Consequently we can approximate using first order expansions at ε_f or $\varepsilon_f + \hbar\omega_{\mathbf{Q}}$ depending on which integral I_{nm} is involved. By proceeding in this way and using equations (5.10) and (5.11) we find that:

$$S^g_{xx} = S^o_g + p\frac{\omega^2 \tau_f^2}{1 + \omega^2 \tau_f^2} S^1_g \tag{5.21}$$

and

$$S^g_{xy} = p\frac{\omega \tau_f}{1 + \omega^2 \tau_f^2} S^1_g \tag{5.22}$$

where

$$S^o_g = -\frac{2C_g \tau_f}{\sigma_o} \int\int dq dq_z q^2 F(\mathbf{Q}) \lambda^o(\mathbf{Q}) \int_0^\infty du f(u^2 + \gamma)[1 - f(u^2 + \gamma + \hbar\omega_{\mathbf{Q}})] \tag{5.23}$$

and

$$S^1_g = \frac{2C_g \tau_f}{\sigma_o} \int\int dq dq_z q^2 F(\mathbf{Q}) \lambda^1(\mathbf{Q}) \int_0^\infty du f(u^2 + \gamma)[1 - f(u^2 + \gamma + \hbar\omega_{\mathbf{Q}})] \tag{5.24}$$

with

$$\lambda^o(\mathbf{Q}) = 1 + p\lambda^1(\mathbf{Q}) \tag{5.25}$$

and

$$\lambda^1(\mathbf{Q}) = \frac{1}{2}\frac{\hbar\omega_{\mathbf{Q}}}{\varepsilon_f}[1 + \frac{\hbar\omega_{\mathbf{Q}}}{\hbar^2 q^2 / 2m^*}] \tag{5.26}$$

Finally, by summing the contributions to the thermopower tensor elements given in these equations and in equations (5.12) and (5.13), we see that the total magnetothermopower and the Nernst-Ettinghausen coefficient are:

$$\Delta S_{xx} = p\frac{\omega^2\tau_f^2}{1+\omega^2\tau_f^2}C \tag{5.27}$$

$$S_{xy} = p\frac{\omega\tau_f}{1+\omega^2\tau_f^2}C \tag{5.28}$$

where

$$C = S_g^1 + C_d \tag{5.29}$$

It can be seen from equations (5.14),(3.79) and (5.24) that C is independent of the magnetic field B.

5.4 Discussion.

The magnetothermopower tensor dependence upon B is predicted by equations (5.27) and (5.28). Interestingly, the structural simplicity of the diffusion terms are maintained when drag processes are taken into account. Since ΔS_{xx} is proportional to $\omega^2\tau_f^2/(1+\omega^2\tau_f^2)$, the rate of decrease of $|\Delta S_{xx}|$ increases below $\omega\tau_f = 1$ and decreases above it with the sign of ΔS_{xx} being determined by the sign of p. S_{xy} is proportional to $\omega\tau_f/(1+\omega^2\tau_f^2)$. Hence $\omega\tau_f = 1$ is predicted to be a stationary point with the extreme value being $Cp/2$. S_{xy} has a maximum at $\omega\tau_f = 1$ when $p > 0$ (GaAs/AlGaAs heterojunction) and a minimum when $p < 0$ (Si-MOSFET), according to the calculations presented in Chapter 4.

Both the magnitude and the sign of the derivative of τ with respect to energy in the neighborhood of ε_f are important in determining the behaviour of the elements of the magnetothermopower tensor. Their sign is determined by the sign of p, as can be seen in equations (5.30) and (5.31). In figure 5.1 S_{xx}^d and S_{xy}^d are plotted against $\omega\tau_f$ for various values of p. The diffusive case has been chosen for qualitative discussion. The magnitude of p is particularly important for the sign of the diffusion thermopower, as is predicted by equation (5.12). If $p < -(1+\omega_c^2\tau_f^2)$, S_{xx}^d changes sign (figure 5.1). This can lead to the observation of a positive S_{xx} at low temperatures, where diffusion dominates.

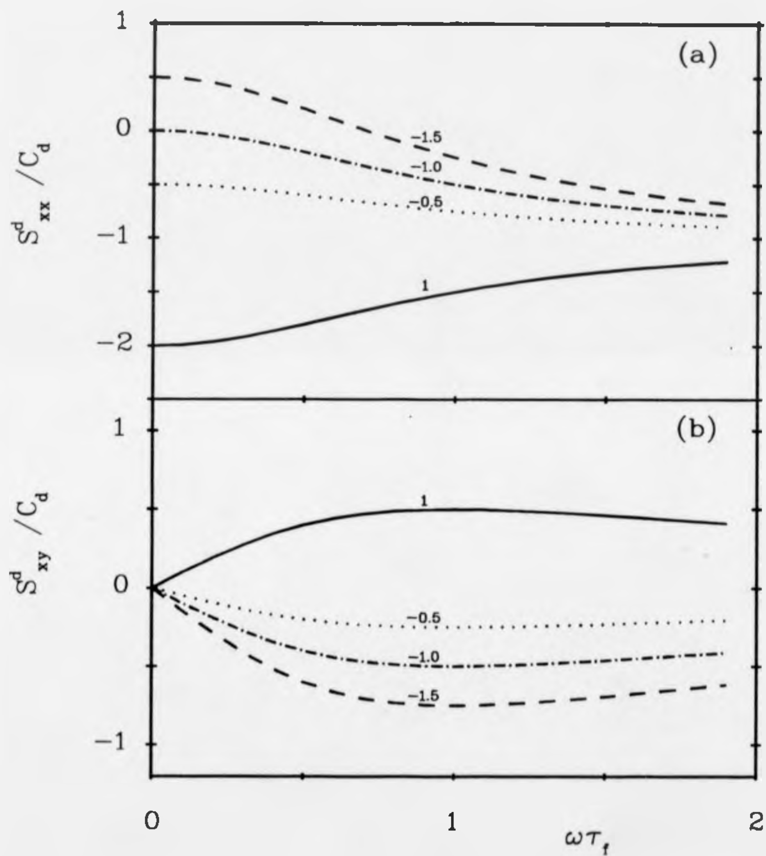

Figure 5.1: Thermopower tensor versus $\omega\tau_f$.

S^d_{xx}/C_d (5.1a) and S^d_{xy}/C_d (5.1b) are plotted versus $\omega\tau_f$ for different values of p.

Such an observation has already been reported for the 2DEG embedded in a Si-MOSFET in zero magnetic field and it has been discussed in Chapter 4. Here, it is predicted that the electron density at which the thermopower vanishes changes with applied magnetic field.

Detailed numerical calculations for a Si-MOSFET used in recent experiments (Chapter 4) are presented in figures 5.2, 5.3 and 5.5. The electron den-

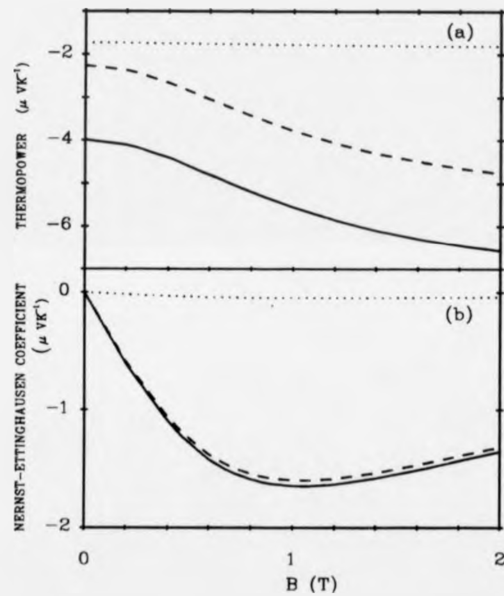

Figure 5.2: Magnetothermopower tensor in a Si-MOSFET at T = 1.5 K. S_{xx} (5.2a) and S_{xy} (5.2b) are plotted versus B for drag (dotted line), diffusion (dashed line) and total (solid line). Si-MOSFET with $N_s = 10.7 \times 10^{15} m^{-2}$ at $T = 1.5$ K.

sity is $N_s = 10.7 \times 10^{15} m^{-2}$ and the measured mobility at T=1 K is $\mu \sim 1 m^2/Vs$ [58, 59]. This value has also been found theoretically by considering interface ionized impurities and interface roughness to dominate the electron scattering, as it has been shown in Chapter 4. The calculated value for p is -0.6. Since $\mu B \sim 1$ at $B \sim 1$T semiclassical behaviour is expected to be observed for this Si-MOSFET, at low temperatures and for magnetic fields well above the local-

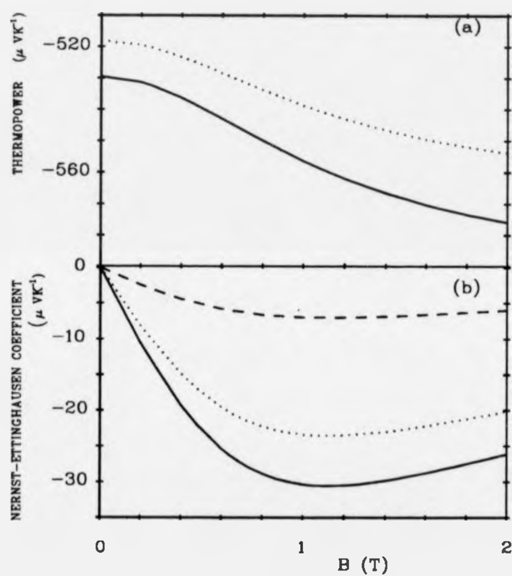

Figure 5.3: Magnetothermopower tensor in a Si-MOSFET at $T = 7$ K.
In 5.3a S_{xx} is plotted versus B for drag (dotted line) and for total thermopower (solid line). In 5.3b S_{xy} is plotted versus B for diffusion (dashed line), drag (dotted line) and total thermopower (solid line). Si-MOSFET with $N_s = 10.7 \times 10^{15} m^{-2}$ at $T = 7$ K.

ization regime until the onset of the Landau quantization. The high field limit of the semiclassical regime coincides with the onset of Landau quantization and measurements there would indicate the nature of cross-over.

As is illustrated in figure 5.2, the main contribution to both the magnetothermopower ΔS_{xx} and the Nernst-Ettinghausen (S_{xy}) coefficients is due to electron diffusion when $T < 2$ K. We see from equations (5.21) and (5.22) that the phonon-drag contribution is determined by the magnitude of S_g^1 which depends on the ratio $\hbar\omega_{\mathbf{Q}}/\varepsilon_f$. At low T the mean phonon energies are small resulting in a small value of S_g^1. Increasing T increases the mean phonon energies with the result that S_g^1 goes up. We see from figure 5.3 that the phonon-drag contribution dominates when $T = 7$ K.

The same magnetic field dependence is predicted for GaAs/AlGaAs heterojunctions by equations (5.27) and (5.28) and is shown in figures 5.4a and b respectively. In this case, both the magnetothermopower ΔS_{xx} and the Nernst-Ettinghausen coefficient S_{xy} are positive because p is positive (the calculated value for p is 0.9). Moreover, as a result of modulation doping and low interface roughness the mobility of electrons in a heterojunction is much higher than that of electrons in a Si-MOSFET. Typically, for $N_s = 6.82 \times 10^{15} m^{-2}$ and at $T = 4.2$ K, $\mu \sim 25\ m^2V^{-1}s^{-1}$ [80]. Semiclassical effects are expected to be seen up to $B \sim \mu^{-1}\tau_t/\tau_s \sim 400$ mT. The characteristic behaviour is analogous to that described for the Si-MOSFET but the peak in S_{xy} and the turning point in S_{xx} are observed at $B \sim 150$ mT (figure 5.4). Because of the higher electron mobility in the heterojunction, most of the variation with magnetic field is now observed in a narrow range of values around $B \sim 150$ mT which is well below the onset of the Landau quantization. On the other hand, weak localization is important only for $B < 0.1$ mT. Therefore, the region where semiclassical effects occur is completely distinct and direct measurements should confirm the above predictions. Drag dominates at almost all temperatures in GaAs/AlGaAs heterojunctions because m^* is considerably smaller than in Si-MOSFETs.

Equations (5.27),(5.28) can be expressed in the following way:

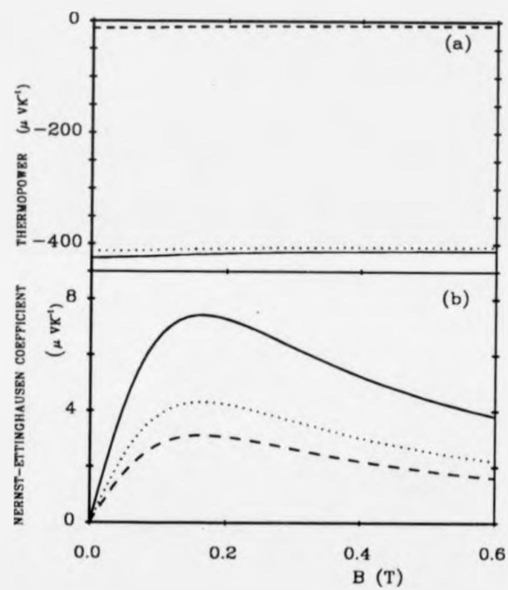

Figure 5.4: Magnetothermopower tensor in a GaAs/AlGaAs heterojunction at $T = 7$ K.

S_{xx} (5.4a) and S_{xy} (5.4b) are plotted versus B for drag (dotted line), diffusion (dashed line) and total (solid line). GaAs/AlGaAs heterojunction with $N_s = 6.82 \times 10^{15} m^{-2}$ at $T = 7$ K.

$$\frac{\Delta S_{xx}}{C} = p\frac{\mu^2 B^2}{1 + \mu^2 B^2} \tag{5.30}$$

$$\frac{S_{xy}}{C} = p\frac{\mu B}{1 + \mu^2 B^2} \tag{5.31}$$

The quantity p reflects the dominant scattering process and will vary from system to system. The direct relation between magnetothermopower effects and p is expected to prove useful in determining p experimentally. At a particular temperature both μ and N_s (and consequently ε_f) are usually known from Hall effect and conductivity measurements. The parameters λ_p, Ξ_u, Ξ_d can be estimated experimentally. Therefore C in the above equations can be calculated for a given T and N_s. Hence, we can determine the value of p by fitting either equation (5.30) or equation (5.31) to experimental data points for either ΔS_{xx} or S_{xy} as functions of B. At low temperatures ($T < 2$ K for Si-MOSFET and $T < 0.4$ K for GaAs/AlGaAs heterojunction) phonon-drag effects are negligible and we can see from equation (5.29) that $C = C_d$. Therefore, the value of p can be deduced from diffusion magnetothermopower effects. It should be noticed that even zero-magnetic field thermopower data at low temperatures (where the diffusion thermopower is practically the only contribution to the total thermopower) can give an estimate for the value of p. The new prediction of the present theory is that the magnetothermopower effects due to phonon-drag depend on p in the same way as those due to diffusion. Thus, even at comparatively high temperatures the experimental data can be processed to yield a value of p in a similar way to that for low temperatures. At higher temperatures the values of both ΔS_{xx} and S_{xy} are much larger than they are at low temperatures which makes their experimental determination as function of B much easier.

Another consequence of equations (5.27),(5.28) is:

$$\frac{\Delta S_{xx}(B)}{S_{xy}(B)} = \mu B \tag{5.32}$$

Equation (51) implies that a plot of $\Delta S_{xx}/S_{xy}$ versus B should be straight line with slope μ. Since the mobility is usually known from other experiments, this plot provides a simple check of the theory.

The validity of equations (5.21) and (5.22) remains to be discussed. The discussion is concentrated on the situation when phonon-drag dominates ($T > 2$ K for a Si-MOSFET and 0.4 K for a GaAs/AlGaAs heterojunction). The deviation of the results calculated from equations (5.21) and (5.22) from exact results depends on $k_B T/\varepsilon_f$. We compare approximate and exact results in figure 5.5 for Si-MOSFET for $k_B T/\varepsilon_f = 0.09$ and 0.24. From those and similar plots we conclude that the approximate phonon-drag formulae are valid when $k_B T/\varepsilon_f < 0.1$.

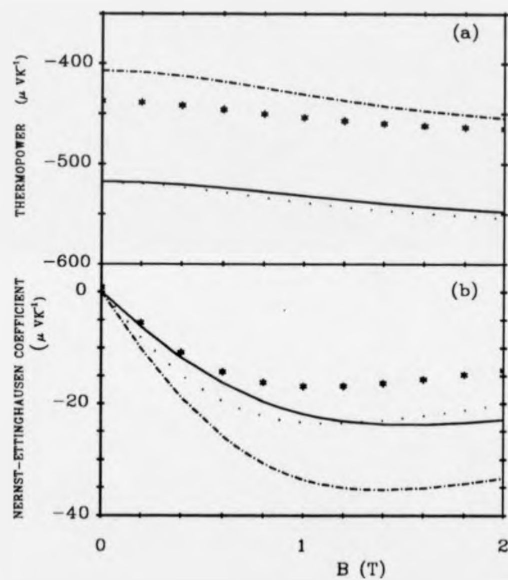

Figure 5.5: Validity of approximations in magnetothermopower calculations. A comparison of exact results with approximations in which functions involving the relaxation time are expanded about the Fermi level. S_{xx} is shown in Fig 5.5a for $T = 7$ K. The full line is exact the dots are approximations for $N_s = 10.7 \times 10^{15} m^{-2}$ and $k_B T/\epsilon_f = 0.09$. The dash-dot line is exact and the stars are approximations for $N_s = 4 \times 10^{15} m^{-2}$ and $k_B T/\epsilon_f = 0.24$. S_{xy} is shown in Fig 5.5b for $T = 7$ K for the same two cases using the same notation.

Chapter 6

Conclusions and suggestions for further work

The objective of the work presented in this thesis is to contribute to the understanding of 2DEG transport and confined LO phonons. We pay particular attention to thermopower at temperatures up to 7 K in zero magnetic field. We have also made calculations of thermopower in the magnetic field window separating weak localization and Shubnikov de-Haas effects.

Low dimensional heterostructures provide model systems in which to study quantum physics. Some of the main achievements in this field have been discussed in the Introduction. It has been shown that the electron motion becomes planar as a result of a confinement potential created by the application of an external electric field or the conduction band discontinuity of the materials across the interface. In addition, in the Introduction we discuss the band profile of the two systems studied extensively in this thesis, the Si-MOSFET and the GaAs/AlGaAs heterojunction, and also the appropriate variational wavefunction for electron transport in these systems.

There has been a great deal of discussion of optical phonons in heterostructures and considerable controversy has resulted from the application of interface connection rules which were either electrostatic or mechanical and the assumption of sinusoidal modes. These modes have either an electrostatic scalar potential or a relative displacement that contradicts the predictions of microscopic

models and Raman experiments. A simple, reliable theory for optical phonons in quantum wells is needed because electron scattering at room temperatures is dominated by LO phonon scattering. The modification of LO phonons from the bulk phonons has an important effect on the scattering rates and consequently on the transport properties (e.g. [83]). The Modified Dielectric Continuum Model (MDCM) that is proposed here was one of the first models to successfully describe the longitudinal optical modes in a AlAs/GaAs/AlAs quantum well. The reformulated slab waves are the normal modes of the present problem and satisfy both electrostatic and mechanical boundary conditions. When the finite bulk dispersion is included, the normal modes are found to be admixtures of the bulklike and interface waves which are the normal modes in the dispesionless limit. These results are in agreement with the findings of microscopic models [15, 17]. The bulk dispersion can never be considered a small perturbation because it lifts the degeneracy of the bulklike modes and causes mixing between bulklike and interface vibrations. The MDCM has been shown to agree very well with the microscopic model of Huang and Zhu in the zero-dispersion limit [15]. Although, a similar comparison with dispersive models would be interesting, it has not been done here because calculations of dispersive microscopic models for AlAs/GaAs/AlAs quantum wells were not available when this work was carried out. Such a comparison would indicate whether the validity of the bulk equations on the interfaces is justified and what modifications would improve the agreement of macroscopic and microscopic models. Raman experiments have verified the existence of bulklike and interface modes independently. Raman scattering can also probe the frequencies and the hybrid character of the modes [6]. However, if the frequency resolution of an experiment is not adequate to resolve the individual phonon branches, then a measurement of the electron-phonon interaction will give very similar results with and without dispersion, in particular the coupling will only be strong near to the LO and interface mode frequencies. High resolution spectroscopy should probe the number of modes, their hybridic character and their frequencies, thus providing a way of quantitatively checking the MDCM. We note, that the symmetric

modes with $\omega \sim \omega_L^{GaAs}$ do not exhibit interface/bulklike mixing, because there is no symmetric interface mode at this frequency.

The main contribution of this work to the understanding of electron transport properties in the absence of magnetic fields is the simultaneous consideration of the mobility and the thermopower. Electron mobility data have been routinely explained in terms of scattering by ionized impurities and by interface irregularities. A simple isotropic theory is usually considered adequate in modelling the interface roughness. This study shows that the quantitative success of such treatments often relies on the freedom used to estimate the relative importance of each scattering mechanism which is involved. The special features of the scattering mechanisms have been studied and a better understanding of the effectiveness of each of them has been gained. The ionized impurities scatter the electrons at small or large angles, depending on whether they are located far from or near to the electron gas respectively. Interface roughness scatters the electrons through large angles and is related to the positive thermopower values which are observed [58].

In almost all the cases, and for both the systems examined, the mobility and the thermopower have been simultaneously explained satisfactorily. A serious discrepancy between theory and experiment is found only for one Si-MOSFET sample, in which a change of sign in the thermopower is observed at low temperatures. This change of sign is attributed to dominant interface roughness scattering. Here, the theory deviates from the measured N_s dependence of the mobility at high electron densities. It is concluded that this discrepancy is due to the failure of the theory of interface roughness to accommodate effects caused by the peculiarities of the structure near the interface. Considerably better agreement between theory and experiment is found in the GaAs/AlGaAs heterojunction samples in which interface roughness scattering does not dominate. The need for a more elaborated theory of interface roughness is indicated. Guidance from experiments can be obtained by a microscopic examination of Si/SiO_2 interfaces in samples that show positive thermopowers at low temperatures and electron densities low enough to exclude second subband occupation.

These experiments should be combined with similar examinations of samples that do not show positive thermopowers data.

Electron mobility calculations are restricted to $T \sim 1$ K, although the variation of the mobility with electron density has been measured at a wide range of temperatures, as it can be seen in figure 4.1. Theory can explain this temperature dependence by the thermal broadening of screening, which enhances the scattering potential and causes a reduction of the mobility as the temperature increases. At low electron densities, typically $N_s < 4 \times 10^{15} m^{-2}$, the mobility decreases very rapidly and the transport behaviour enters the regime of thermally activated hopping where the effects of disorder are important. These effects have been neglected here because they only affect a restricted, low electron density region well below $N_s \sim 10^{16} m^{-2}$ where the change of sign of thermopower is observed.

The phonon-drag calculations are based on Cantrell-Butcher (CB) theory. Some improvement has been made by considering the temperature dependence of screening, the phonon mean free path and the effect of thermal broadening of the Fermi function. It has been confirmed that the existing phonon drag theory is successful in explaining the main features of the thermopower data. Good quantitative agreement is also generally obtained. At $N_s > 2 \times 10^{16} m^{-2}$, the phonon drag is overestimated by the calculations. This might be due to the failure of the single subband approximation for the screening in this region. We also note that an underestimation of the phonon drag can be seen at low N_s and $T > 6$ K. Thermal broadening of the Fermi function did not solve this problem and mechanisms that enhance the electron-phonon interaction should be considered as possible candidates. We believe that the following steps are essential for this purpose. At first, multi-subband screening calculations of electron screening would help to reduce the overestimated thermopower values obtained at high temperatures. A better understanding of the N_s dependence of the interface roughness relaxation time would also be useful and would influence both the diffusion and the phonon-drag thermopower calculations. We note that although in Si the bulk value of Ξ_u has not been questioned (except

in [84]) in GaAs, by fitting mobility experiments, it has been found that an enhanced value, relative to the bulk value, is appropriate for confined electrons [46, 50]. In [50] it is suggested that this enhancement may be caused by interface phonons. However, no interface acoustic phonons exist in the heterojunction and the physical origin of the change of the deformation potential is not clear. Nevertheless, a modification of the deformation potential value in either system is directly reflected in the agreement between theory and experiment. In Si, the lattice anisotropy in the electron-phonon interaction has been regarded as small and instead of considering each direction of the phonon wavevector **Q** separately in calculating the transition rate, as it has been done by Herring and Vogt [48], an implicit averaging over the azimuthial angle of **Q** has been adopted. Proper consideration of the phonon anisotropy would broaden the phonon distribution and further enhance the electron-phonon interaction at high temperatures and low electron densities.

The physics of thermopower shows interesting phenomena. Here, we have concentrated on electron scattering by ionized impurities, interface roughness and the electron-phonon interaction in Si-MOSFETs and GaAs/AlGaAs heterojunctions. Similar calculations would apply to different systems such as strained heterojunctions. A good understanding of the zero-magnetic field thermopower is also useful for the non-zero magnetic field case in the quantum limit. An interesting problem is the calculation of phonon drag contribution to transport coefficients in systems where quantum transport takes place (e.g. in quantum point contacts where all transport coefficients exhibit quantum size effects [86]) or when strong magnetic fields are applied. Recently, semimagnetic semiconductor heterostructures have started attracting the attention of scientists. These structures are interesting because the physics of the 'conventional' heterostructures is modified by the magnetic properties of the alloys such as exchange interaction and also novel phenomena may emerge. Calculations and measurements of thermotransport in these systems may prove challenging in the near-future. Finally, we note that thermopower calculations can be extended to higher temperatures, since the present formalism allows for the temperature

dependence of screening and thermal broadening of the electron distribution function. At higher temperatures, mechanisms other than boundary scattering dominate in limiting the phonon mean free path. At room temperature, LO phonons need to be included. Our study of LO phonons could be used in the calculation of the relaxation time, p and thermopower at high temperatures.

Thermoelectric effects have also been examined in the presence of a magnetic field perpendicular to the 2DEG when the magnitude of B is above the weak localization regime and below the Landau quantization regime. The Boltzmann equation has been used to obtain the transport coefficients when electron scattering by ionized impurities and imperfections, as well as electron-phonon interactions, are taken into account. When the electron-phonon coupling is weak and the elastic scattering of the electrons is described by a relaxation time, the magnetothermoelectric effects are similar in the diffusion and phonon-drag dominated regimes. The predicted behaviour is easily verified experimentally and such experiments could provide a convenient route to the direct determination of the logarithmic derivative of the relaxation time at the Fermi level.

Appendix A

Normalized phonon potential functions

The expressions for the normalized potential for a quantum well plotted in figures 2.3 and 2.4 are:

<u>Symmetrical potential function</u>

$$\Phi = \rho \begin{cases} \varepsilon_2 sh(\pi k_{||}) cos(\pi k_n) e^{2\pi k_{||}(\zeta+1/2)} & \zeta < -1/2 \\ \alpha\ cos(2\pi k_n \zeta) - \varepsilon_1 cos(\pi k_n) ch(2\pi k_{||}\zeta) & -1/2 < \zeta < 1/2 \\ \varepsilon_2 sh(\pi k_{||}) cos(\pi k_n) e^{-2\pi k_{||}(\zeta+1/2)} & \zeta > 1/2 \end{cases} \qquad (A.1)$$

with

$$\rho^2[\frac{\alpha^2}{2}(k_n^2 + k_{||}^2) + \frac{\alpha^2}{2}(k_{||}^2 - k_n^2)\frac{sin(2\pi k_n)}{2\pi k_n} + \beta^2 k_{||}^2 \frac{sh(2\pi k_{||})}{2\pi k_{||}} + c^2\frac{k_{||}}{\pi}$$

$$-2\alpha\beta\frac{k_{||}}{\pi} sh(\pi k_{||}) cos(\pi k_n)] = 1 \qquad (A.2)$$

$$\alpha = \varepsilon_2 sh(\pi k_{||}) + \varepsilon_1 ch(\pi k_{||}) \qquad (A.3)$$

$$\beta = \frac{\omega_{L2}^2 - \omega_{T2}^2}{\omega^2 - \omega_{T2}^2}\varepsilon_1 cos(\pi k_n) \qquad (A.4)$$

$$c = (\frac{\varepsilon_{\infty 1}}{\varepsilon_{\infty 2}}\frac{\omega_{L1}^2 - \omega_{T1}^2}{\omega_{L2}^2 - \omega_{T2}^2})^{1/2}\frac{\omega_{L2}^2 - \omega_{T2}^2}{\omega^2 - \omega_{T1}^2}\varepsilon_2 sh(\pi k_{||}) cos(\pi k_n) \qquad (A.5)$$

Antisymmetric potential function

$$\Phi = \rho \begin{cases} \varepsilon_2 ch(\pi k_{||}) sin(\pi k_n) e^{2\pi k_{||}(\zeta+1/2)} & \zeta < -1/2 \\ \alpha\ sin(2\pi k_n \zeta) - \varepsilon_1 sin(\pi k_n) sh(2\pi k_{||}\zeta) & -1/2 < \zeta < 1/2 \\ \varepsilon_2 ch(\pi k_{||}) sin(\pi k_n) e^{-2\pi k_{||}(\zeta+1/2)} & \zeta > 1/2 \end{cases} \quad \text{(A.6)}$$

with

$$\rho^2[\frac{\alpha^2}{2}(k_n^2 + k_{||}^2) + \frac{\alpha^2}{2}(-k_{||}^2 + k_n^2)\frac{sin(2\pi k_n)}{2\pi k_n} + \beta^2 k_{||}^2 \frac{sh(2\pi k_{||})}{2\pi k_{||}} + c^2 \frac{k_{||}}{\pi}$$

$$-2\alpha\beta \frac{k_{||}}{\pi} ch(\pi k_{||}) sin(\pi k_n)] = 1 \quad \text{(A.7)}$$

$$\alpha = \varepsilon_2 ch(\pi k_{||}) + \varepsilon_1 sh(\pi k_{||}) \quad \text{(A.8)}$$

$$\beta = \frac{\omega_{L2}^2 - \omega_{T2}^2}{\omega^2 - \omega_{T2}^2} \varepsilon_1 sin(\pi k_n) \quad \text{(A.9)}$$

$$c = (\frac{\varepsilon_{\infty 1}}{\varepsilon_{\infty 2}} \frac{\omega_{L1}^2 - \omega_{T1}^2}{\omega_{L2}^2 - \omega_{T2}^2})^{1/2} \frac{\omega_{L2}^2 - \omega_{T2}^2}{\omega^2 - \omega_{T1}^2} \varepsilon_2 ch(\pi k_{||}) sin(\pi k_n) \quad \text{(A.10)}$$

In the above expressions, $k_{||}$ and k_n are in units of $2\pi/L$ with L being the width of the quantum well. The parameter ζ is defined as $\zeta = z/L$ and ch (sh) is used to denote the hyperbolic function $cosh$ ($sinh$).

The parameter values used in the calculations have been found in standard tables (Landolt-Börnstein) and are: $\omega_L^{GaAs} = 292.32 cm^{-1}$, $\omega_T^{GaAs} = 268.6 cm^{-1}$, $\varepsilon_\infty^{GaAs} = 10.9$, $\varepsilon_o^{GaAs} = 12.91$, $\omega_L^{AlAs} = 400.72 cm^{-1}$, $\omega_T^{AlAs} = 360.9 cm^{-1}$, $\varepsilon_\infty^{AlAs} = 8.16$, $\varepsilon_o^{AlAs} = 10.06$. The bulk dispersion parameter for GaAs is obtained by fitting the parabolic dispersion relation to measured bulk dispersion data [8] and direct calculation using analytical expressions derived from microscopic models [15]. The dimensionless value of b_L, appropriate for the dispersion relation with both the frequencies and the wave vectors in units of cm^{-1}, is $b_L = 1.5 \times 10^{-6}$.

Appendix B

Solution of the linearised Boltzmann equation.

We assume that the electron gas is located in the xy plane, in the presence of an in-plane electric field $\mathbf{E}$, an in-plane temperature gradient ∇T and a perpendicular magnetic field $\mathbf{B}$ in the z-direction. Then the linearized Boltzmann equation when only the ground subband is occupied can be written as:

$$-\frac{f^1}{\tau} - \frac{e}{\hbar}B(\nabla_{\mathbf{k}} f^1 \times \mathbf{v})_z = -\frac{\partial f^o}{\partial \varepsilon}\frac{\varepsilon - \varepsilon_f}{T}\mathbf{v}\nabla_{\mathbf{r}} \cdot T + e\frac{\partial f^o}{\partial \varepsilon}\mathbf{v} \cdot \mathbf{E} - U \qquad (B.1)$$

The following two equations have been used to bring the above equation into this form:

$$\nabla_{\mathbf{r}} f^o = -\frac{\partial f^o}{\partial \varepsilon}(\varepsilon - \varepsilon_f)\frac{\nabla_{\mathbf{r}} T}{T} \qquad (B.2)$$

and

$$\nabla_{\mathbf{k}} f^o = \hbar \mathbf{v}\frac{\partial f^o}{\partial \varepsilon}. \qquad (B.3)$$

Defining $\lambda = (\omega\tau)^{-1}$, where $\omega = |e|B/m^*$ is the cyclotron frequency, and expressing the electron wavevector as $\mathbf{k} = (kcos\theta, ksin\theta)$, equation (B.1) becomes:

$$\lambda f^1 + \frac{\partial f^1}{\partial \theta} = g_1(k)cos\theta + g_2(k)sin\theta + g_3(k,\theta) \qquad (B.4)$$

where

$$g_1(k) = \frac{\partial f^o}{\partial \varepsilon}[\frac{\varepsilon - \varepsilon_f}{\omega T} v \frac{\partial T}{\partial x} - \frac{\epsilon}{\omega} v E_x], \quad (B.5)$$

$$g_2(k) = \frac{\partial f^o}{\partial \varepsilon}[\frac{\varepsilon - \varepsilon_f}{\omega T} v \frac{\partial T}{\partial y} - \frac{\epsilon}{\omega} v E_y] \quad (B.6)$$

and

$$g_3(k, \theta) = \frac{U(k, \theta)}{\omega}. \quad (B.7)$$

The differential equation (B.4) is solved by using the Green's function which is defined by the differential equation:

$$\frac{\partial G}{\partial \theta} + \lambda G = \delta(\theta - \theta^*) \quad (B.8)$$

and the periodic boundary condition: $G(2\pi) = G(0)$. We find that

$$G(\theta, \theta^*) = \begin{cases} \dfrac{\epsilon^{-\lambda(\theta-\theta^*)}}{1 - \epsilon^{2\pi\lambda}} & \theta > \theta^* \\ \dfrac{\epsilon^{-\lambda[2\pi+(\theta-\theta^*)]}}{1 - \epsilon^{2\pi\lambda}} & \theta < \theta^* \end{cases} \quad (B.9)$$

and the solution of (B.4) is seen to be:

$$f^1(k, \theta) = \int_0^{2\pi} d\theta^* G(\theta, \theta^*)[g_1(k) cos\theta^* + g_2(k) sin\theta^* + g_3(k, \theta^*)] \quad (B.10)$$

Equation (B.10) gives:

$$f^1(k, \theta) = f^1_d + f^1_g \quad (B.11)$$

where

$$f^1_d = \frac{\omega\tau}{1 + \omega^2\tau^2}[g_1(k)(cos\theta + (\omega\tau) sin\theta) + g_2(k)(sin\theta - (\omega\tau) cos\theta)] \quad (B.12)$$

is the part of f^1 due to electron diffusion processes and

$$f^1_g = \int_0^{2\pi} d\theta^* G(\theta, \theta^*) g_3(k, \theta^*) \quad (B.13)$$

is the part of f^1 due to phonon drag.

We note that f^1_d can be written in the following form:

$$f_d^1(\mathbf{k}) = -\frac{df^o}{d\varepsilon}\frac{\mathbf{v}\cdot\mathbf{A} - \omega\tau(\mathbf{v}\times\mathbf{A})_z}{1+\omega^2\tau^2} \quad \text{(B.14)}$$

with

$$\mathbf{A} = \tau(\varepsilon)(e\mathbf{E} - (\varepsilon - \varepsilon_f)\frac{\nabla_{\mathbf{r}}T}{T}). \quad \text{(B.15)}$$

In the zero magnetic field limit, equations (B.14) and (B.13) become:

$$f_d^1 = -\frac{df^o}{d\varepsilon}\mathbf{v}\cdot\mathbf{A} \quad \text{(B.16)}$$

and

$$f_g^1 = \tau(\varepsilon)U(\mathbf{k}) \quad \text{(B.17)}$$

Appendix C

Derivation of transport coefficients for electron diffusion processes

When electron diffusion dominates, the 2D formalism for the transport coefficients can be derived by extending the standard 3D formalism [85]. Equations (3.9) and (B.14) give:

$$\mathbf{J}_{2D}^{d} = -\frac{e}{2\pi^2\hbar^2}\int \frac{\partial f^o}{\partial \varepsilon}(\mathbf{X}\cdot\nabla_{\mathbf{k}}\varepsilon)\nabla_{\mathbf{k}}\varepsilon d\tau_{\mathbf{k}} \tag{C.1}$$

where

$$\mathbf{X} = \frac{\mathbf{A} + (e\tau/m^*)(\mathbf{A}\times\mathbf{B})}{1+\omega^2\tau_f^2} \tag{C.2}$$

and $\mathbf{A}$ is defined in equation (B.15). To simplify the calculations the following vector is defined:

$$\mathbf{M} = -\frac{1}{2\pi^2}\int \varepsilon^{r-1}\tau^s \frac{\partial f^o}{\partial \varepsilon}\frac{(\mathbf{G}\cdot\mathbf{v})\mathbf{v}d\tau_{\mathbf{k}}}{1+\omega^2\tau^2} \tag{C.3}$$

where $\mathbf{G}$ will be chosen later on. It is convenient to define a second rank tensor K_{rs} with elements:

$$K_{rs}^{ij} = -\frac{1}{2\pi^2}\int \frac{\varepsilon^{r-1}\tau^s}{1+\omega^2\tau^2}\frac{\partial f^o}{\partial \varepsilon}v_i v_j d\tau_{\mathbf{k}} \tag{C.4}$$

Then equation (C.3) can be written as:

$$\mathbf{M} = K_{rs}\mathbf{G} \tag{C.5}$$

Equation (C.4) may be transformed into:

$$K_{rs}^{ij} = \delta_{ij} K_{rs} \tag{C.6}$$

where

$$K_{rs} = K_{rs}^{11} = K_{rs}^{22} = -\frac{1}{e^2}\int \varepsilon^{r-1}\tau^{s-1}\sigma_B(\varepsilon)\frac{\partial f^o}{\partial \varepsilon} d\varepsilon \tag{C.7}$$

and

$$\sigma_B(\varepsilon) = \frac{e^2 I(\varepsilon)\tau(\varepsilon)}{m^*(1+\omega^2\tau^2)}. \tag{C.8}$$

$\sigma_B(\varepsilon)$ may be interpreted as an energy-dependent conductivity. Hence, equation (C.5) becomes simply:

$$\mathbf{M} = \frac{1}{2}(K_{rs}^{11} + K_{rs}^{22})\mathbf{G} \tag{C.9}$$

which yields:

$$\mathbf{M} = -\frac{1}{e^2}\int \varepsilon^{r-1}\tau^{s-1}\sigma_B(\varepsilon)\frac{\partial f^o}{\partial \varepsilon}\mathbf{G} d\varepsilon \tag{C.10}$$

If we put

$$\mathbf{G} = \mathbf{A} + \frac{e\tau}{m^*}\mathbf{A}\times\mathbf{B} \tag{C.11}$$

in equation (C.3), **A** being given by equation (B.15), we get for $\mathbf{J}_{\mathbf{2D}}^{\mathbf{d}}$:

$$\mathbf{J}_{\mathbf{2D}}^{\mathbf{d}} = e^2 K_{11}\mathbf{E} + e\frac{K_{11}\varepsilon_f - K_{21}}{T}\nabla T + \frac{e^3}{m^*}K_{12}\mathbf{E}\times\mathbf{B} + \frac{e^2}{m^*}\frac{K_{12}\varepsilon_f - K_{22}}{T}\nabla T\times\mathbf{B} \tag{C.12}$$

By comparing equation (C.12) with equation (3.1) and working the energy integrals out, we obtain:

$$L_{xx} = \frac{\pi^2 k_B}{3|e|} k_B T \sigma_B'|_{\varepsilon_f} \tag{C.13}$$

and

$$L_{yx} = \frac{\pi^2 B}{3m^*} k_B^2 T (\tau\sigma_B)' \tag{C.14}$$

where the derivatives are with respect to energy.

Bibliography

[1] C Weisbuch and B Vinter, Quantum Semiconductor Structures (Academic Press, Inc. 1991)

[2] T Ando, A Fowler and F Stern, Rev. Mod. Phys. **54** 437 (1982)

[3] T Ando, J. Phys. Jap. **51** 3900 (1982)

[4] W E Howard and F F Fang, Phys. Rev. B **13** 2519 (1976)

[5] T Ando, J. Phys. Jap. **43** 1616 (1977)

[6] A K Sood, J Menendez, M Cardona and K Ploog, Phys. Rev. Lett. **54** 2111 (1985); Phys. Rev. Lett. **54** 2115 (1985)

[7] B Jusserand, D Paquet and A Regreny, Superlatt. Microstructures **1** 61 (1985)

[8] Z P Wang, H X Han and G H Li, Phys. Rev. B **42** 9693 (1990)

[9] M Cardona, Superlatt. Microstructures **5** 27 (1989)

[10] Bangfen Zhu, Phys. Rev. B **46** 13619 (1992)

[11] F Garcia-Moliner, J. Phys.: Condens. Matter **5** 5389 (1993)

[12] R Perez-Alvarez, F Garcia-Moliner, V R Velasco and C Trallero-Giner, Phys. Rev. B **48** 5672 (1993)

[13] X Zianni, P N Butcher and I Dharssi, J. Phys.: Condens. Matter **4** L77 (1992)

[14] K J Nash, Phys. Rev. B **46** 7723 (1992)

[15] Kun Huang and Bangfen Zhu, Phys. Rev B **38** 2183 (1988); **38** 13377 (1988); Bangfen Zhu, ibid. **38** 7694 (1988)

[16] T Tsuchiya, H Akera and T Ando, Phys. Rev. B **39** 6025 (1989); H Akera and T Ando, Phys. Rev. B **40** 2914 (1989)

[17] F Bechstedt and H Gerecke, Phys. Stat. Sol. (b) **156** 151 (1989); J. Phys.: Condensed Matter **2** 4363 (1990); Phys. Rev. B **43** 7053 (1991)

[18] E Molinari and A Fasolino, Superlatt. Microstructures **4** 449 (1988)

[19] R Enderlein, Phys. Rev. B **43** 14513 (1991)

[20] M Born and K Huang, Dynamical theory of Crystal Lattice 1962 (Oxford: Clarendon)

[21] R Fuchs and K L Kliewer, Phys. Rev. B **140** A2076 (1965)

[22] R E Camley and D Mills, Phys. Rev B **29** 1695 (1984)

[23] R Lassnig, Phys. Rev. B **30** 7132 (1984)

[24] K J Nash and D J Mowbray, J. Lumin. **44** 315 (1989)

[25] I. Dharssi, PhD thesis, Physics Dept., University of Warwick (1991)

[26] E Molinari, A Fasolino and K Kunc, Phys. Rev. Lett. **56** 1751 (1986)

[27] H Chu and Y Chang, Phys. Rev. B **38** 12369 (1988)

[28] M Babiker, J. Phys. C **19** 683 (1986)

[29] B K Ridley, Phys. Rev. B **39** 5282 (1989)

[30] B K Ridley and M Babiker, Phys. Rev. B **43** 9096 (1991)

[31] P N Butcher, The theory of electron transport in Crystalline Semiconductors in Crystalline Semiconducting Materials and devices, edited by P N Butcher, N H March and M P Tosi. (Plenum Press) 131 (1986)

[32] P N Butcher, An Introduction to the theory of Electron Transport in Low-Dimensional Structures, Trieste Lecture Notes (1990)

[33] D G Cantrell and P N Butcher, J. Phys. C: Solid State Phys. **20** 1985 (1987)

[34] D G Cantrell and P N Butcher, J. Phys. C: Solid State Phys. **20** 1992 (1987)

[35] M J Smith and P N Butcher, J. Phys.: Condens. Matter **1** 1261 (1989)

[36] M J Smith, PhD thesis, University of Warwick, Physics Dept. (1989)

[37] M N Ashroft and N D Mermin, Solid State Physics (Holt Saunders 1976)

[38] H Ehrenreich and M H Cohen, Phys. Rev. **115** 716 (1959)

[39] G D Mahan, Many Particle Physics (New York Plenum 1981)

[40] S Mori and T Ando, Phys. Rev. B **19** 6433 (1979)

[41] E D Siggia and P C Kwok, Phys. Rev. B **2** 1024 (1970)

[42] D S Tang, Phys. Rev. B **37** 8319 (1988)

[43] P F Maldague, Surf. Sci. **73** 296 (1978)

[44] F Stern and W E Howard, Phys. Rev. **163** 816 (1967)

[45] F Stern, Phys. Rev. Let. **44** 1469 (1980)

[46] T Kawamura and S Das Sarma, Phys. Rev. B **42** 3725 (1990)

[47] F J Blatt, Physics of Electronic Conduction in Solids (McGraw-Hill 1968)

[48] C Herring and E Vogt, Phys. Rev. **101** 944 (1956)

[49] B K Ridley, Quantum processes in Semiconductors (Oxford: Clarendon) (1982)

[50] I Gorczyca, T Suski, E Litwin-Staszewka, L Dmowski, J Krupski and B Etienne, Phys. Rev. B **46** 4328 (1992)

[51] K Hirakawa and H Sakaki, Appl. Phys. Lett **49** 889 (1986)

[52] P J Price, Annals of Physics **133** 217 (1981)

[53] S K Lyo, Phys. Rev. B **40** 6458 (1989)

[54] Y C Cheng and E A Sullivan, Surface Science **34** 717 (1973)

[55] S Kundu, C K Sarkar and P K Basu, J. Appl. Phys. **61** 5080 (1987)

[56] P K Basu, C K Sarkar and S Kundu, Surface Science **196** 700 (1988)

[57] G H Kruithof, T M Klapwijk and S Bakker, Phys. Rev. B **43** 6642 (1991)

[58] B L Gallagher, J P Oxley, T Galloway, M J Smith and P N Butcher, J. Phys.: Condens. Matter **2** 755 (1990)

[59] J P Oxley, PhD thesis, Physics Dept., Unversity of Nottingham (1991)

[60] C Ruf, M A Brummell, E Gmellin and K Ploog, Superlatt. and Microstr. **6** 175 (1989)

[61] V K Karavolas, T M Fromhold, P N Butcher, B G Mulimani, B L Gallagher and T P Oxley, J Phys. Condens. Matter **2** 10401 (1990)

[62] D J DiMaria, J. Appl. Phys. **48** 5149 (1977)

[63] V K Karavolas and P N Butcher, J. Phys.: Condens. Matter **3** 2597 (1991)

[64] Y Matsumoto and Y Uemura, Proc. 2nd International Conf. on Solid Surfaces 19974, Japan. J. Appl. Phys. Suppl. **2**, Pt. 2, 367 (1974)

[65] A Gold and V T Dolgopolov, Phys. Rev. B **33** 1076 (1986), and references therein.

[66] S M Goodnick, D K Ferry and C W Wilmsen, Phys. Rev. B **32** 8171 (1985)

[67] G Fishmann and D Calecki, Phys. Rev. B **43** 11581 (1991)

[68] F Stern, Solid State Communications **21** (1977)

[69] M J Smith and P N Butcher, J Phys. Condens. Matter **2** 2375 (1990)

[70] B L Gallagher and P N Butcher, Handbook on Semiconductors (2nd ed), 1 (ed. P T Landsberg), 721 (Elsevier 1992) and references therein.

[71] R Fletcher, M D'Iorio, A S Sachrajda, R Stoner, C T Foxon and J J Harris, Phys. Rev. B **37** 3137 (1988)

[72] B Kramer, G Bergmann and Y Bruynserade, 'Localization, interaction and transport phenomena' (Berlin: Springer-Verlag) (1985)

[73] Y Nagaoma and H Fukyama, Anderson localization (Berlin: Springer-Verlag) (1982)

[74] R Fletcher, M D'Iorio, W T Moore and R Stoner, J. phys. C: Solid State Phys. **21** 2681 (1988)

[75] R Fletcher, E Zaremba, M D'Iorio, C T Foxon and J J Harris, Phys. Rev. B **41** 10649 (1990)

[76] T Ando, J. Phys. Soc. Jap. **51** 3893 (1982)

[77] J P Harrang, R J Higgins, R K Goodall, P R Jay, M Laviron and P Delescluse, Phys. Rev. B **32** 8126 (1985)

[78] See, e.g., G Bergmann, Phys. Rep. **107** 1 (1983)

[79] M J Kearney, R T Syme and M Pepper, Phys. Rev. Lett, **66** 1622 (1991); R T Syme and M J Kearney, Phys. Rev. B **46** 7662 (1992)

[80] R Fletcher, J C Maan, K Ploog and G Weimann, Phys. Rev. B **33** 7122 (1986)

[81] S S Kubakaddi, P N Butcher and B G Mulimani, Phys. Rev. B **40** 1377 (1989)

[82] S Das Sarma and F Stern, Phys. Rev. B **32** 8442 (1985)

[83] I Dharssi and P N Butcher, J. Phys.: Condens. Matter **2** 119 (1990)

[84] H Ezawa, S Kawaji and K Nakamura, Jap. J. Appl. Phys. **13** 126 (1974)

[85] P Kireev, The Physics of Semiconductors, 2nd Edition (Mir-Moscow) (1975)

[86] H van Houten, L W Molenkamp,C W J Beenakker and C T Foxon, Semicond. Sc. Technol. **7** B215 (1992)